UHASSELT

Upscaling of two-phase porous-media flows with evolving fluid-fluid interfaces at the pore scale

Doctoral dissertation
submitted to obtain the degree of *Doctor of Science: Mathematics.*

Sohely Sharmin

Promoter:	Prof. Dr. Iuliu Sorin Pop	Hasselt University
Co-promoter:	Prof. Dr. Carina Bringedal	University of Stuttgart
Committee members:	Prof. Dr. Jochen Schütz	Hasselt University
	Prof. Dr. Fred Vermolen	Hasselt University
Jury members:	Prof. Dr. Kundan Kumar	University of Bergen
	Prof. Dr. Carmen Rodrigo Cardiel	University of Zaragoza

Sohely Sharmin, Upscaling of two-phase porous-media flows with evolving fluid-fluid interfaces at the pore scale, PhD thesis, Hasselt University, Belgium, 2022.

Belgian Royal Library depot number D/2022/2451/80.

This work was funded by the Research Foundation-Flanders (FWO) through the Odysseus program (project GOG1316N).

To my children, Mahdi Alam and Aisha Alam.
I am truly thankful for having them in my life.

Abstract

This thesis concerns the upscaling of two-phase/unsaturated flow and transport problems in porous media. Whereas the mathematical models at the pore scale are in general well understood, but due to their complexity, they are not suited for large-scale numerical simulations. Hence, in practice, Darcy-scale models are better suited. The aim of this thesis is to derive multiscale mathematical models that bridge the gap between pore- and Darcy-scale models. Asymptotic expansions together with transversal averaging and periodic homogenization are used to derive Darcy-scale models starting from pore-scale models. These resulting models are expressed in terms of effective Darcy-scale quantities like saturation, concentration, pressure and Darcy velocity. The derived Darcy-scale models are important since they describe the averaged behaviour of pore-scale models, but still reproduce the main flow features observed at the pore-scale.

First, we consider a pore-scale model for two-phase/unsaturated flow, defined in a two-dimensional thin strip. We use a sharp-interface approach to model the evolution of the free boundary. We consider three cases: two-phase flow with solute-dependent surface tension (the Marangoni effect), two-phase flow with constant surface tension, and unsaturated flow with constant surface tension. By assuming that the ratio between the width and length of the strip approaches 0, we use formal asymptotic expansion methods and derive the limit of transversally averaged models over the thin strip. Depending on the dimensionless parameters, different upscaled models in various pore-scale regimes are obtained. The resulting models involve Darcy-type laws for the flow, with a concentration-dependent surface tension effect (Marangoni effect) and a capillary pressure-saturation dependency involving a second-order derivative of the saturation. These formal results are validated by numerical experiments. We compare the solution of the upscaled models valid in the same capillary regime with the transversally averaged pore-scale quantities, and show that the Marangoni effect influences the overall flow.

Since the porous geometry largely influences the averaged/upscaled quantities and their behavior, we also consider a more general domain, namely a periodically perforated domain. We use a phase-field model for two-phase flow and surfactant transport at the pore scale. Using periodic homogenization theory, we derive a two-scale phase-field model describing the averaged behaviour of the system at the Darcy scale. The resulting two-scale model includes extended Darcy-type laws for the effective velocities, accounting for the concentration-dependent surface tension. The effective quantities are found through the corresponding local (cell) problems at the pore scale. For this two-scale phase-field model, we formulate a numerical scheme and present numerical results highlighting the influence of the solute-dependent surface tension.

Acknowledgements

First, I would like to thank Professor Sorin Pop for qualifying me to work with him and for being the main advisor of my doctoral study. I am very grateful for all his supervision, input into my work, and support. I am also thankful for his generosity and good humor. Due to his exceptional supervision and endless encouragement, the entire journey of my doctoral study was completed very smoothly, and I thoroughly enjoyed the path to completion. He is both an incredible person and an inspiring scientist. I also learned a lot by assisting him in partial differential equations lectures.

I would also like to thank Professor Carina Bringedal for her guidance and always being supportive. She has guided me to focus on the details and, at the same time to keep the big picture in mind. I certainly enjoyed all our fruitful discussions to make this work possible and pleasant for me.

I would also like to thank Professor Jochen Schutz for the helpful and patient discussions of the numerical results and writing of this work. I am thankful for his efforts to organize the CMAT talks, seminars, and summer schools; those activities were important for my doctoral studies. I further thank Professor Fred Vermolen for being part of my doctoral committee and providing all his valuable remarks on the thesis.

I would like to extend my gratitude and appreciation to Professor Carmen Rodrigo Cardiel and Professor Kundan Kumar for being part of the Ph.D. jury.

I would also like to thank my fellow doctoral students and the postdoctoral researchers here in Hasselt (past and present). In particular, I would like to mention the names of

Manuela, Stephan, Koondi, Alex, Markus, Maikel, Jeremy, Hoang-An, Eleni, Arjun, and Ayesha. It was delightful to have their company during my studies. I would like to pay special thanks to Manuela for always listening to me and sharing her knowledge, which is really helpful and warm. She became my best friend and always be my friend. Thanks to Stephan and Koondi for their input on my work; it was an honor to have such a clever and wonderful group of people always helping me.

I would like to thank the members of the Doctoral School of Sciences and Technology at Hasselt University and the Research Foundation-Flanders (FWO) through the Odysseus program (project GOG1316N) for its financial support.

Furthermore, I take this opportunity to thank all my friends and family in Europe and Bangladesh for encouraging me during tough moments. This achievement is also yours.

First, I would like to thank Professor Shafiqul Islam at Dhaka University for encouraging me to apply for the Erasmus Mundus Mobility with Asia program, and for supporting me in pursuing my higher studies at Heidelberg University.

My thanks are extended to my family and my in-law's family for their patience and constant support. I want to show my deep gratitude to my late father, Abdus Salim and my late mother, Asia Khatun. My father was the first person who motivated me to study, which was a privilege for a girl during that time. His last wish was to give me a chance to finish my studies. I also want to thank my sisters Kakoli bu and Shamoli (mejo apu), my brothers Sohel Ahmed and Sayid Ahmed, my mother-in-law Mamtaz Razzak, my father-in-law Abdur Razzaq, and my sister-in-law Razia Alam for supporting me all the time and giving me the strength to resume in my difficult times. They gave me the love and blessings which I used to get from my late parents.

Finally, I thank my husband, Mainul Alam, for supporting me in keeping my parent's end-of-life wishes. This Ph.D. is a product of his honesty, patience, sacrifice, innocence and good vibes. I never felt alone on this journey. It is because of his love and support. I am truly blessed to have him in my life.

Sohely Sharmin (সোহেলী শারমিন)

Hasselt, November 2022

Contents

Publications

This thesis is based on the following publications [17, 161, 162]:

- ”S. Sharmin, C. Bringedal, I.S. Pop, *On upscaling pore-scale models for two-phase flow with evolving interfaces*, Advances in Water Resources, 142 (2020), p.103646, `https://doi.org/10.1016/j.advwatres.2020.103646`.”
- ”S. Sharmin, M. Bastidas, C. Bringedal, I.S. Pop, *Upscaling a Navier-Stokes-Cahn-Hilliard model for two-phase porous-media flow with solute-dependent surface tension effects*, Applicable Analysis, 101 (2022), pp. 1-23, `https://doi.org/10.1080/00036811.2022.2052858`.”
- ”M. Bastidas, S. Sharmin, C. Bringedal, I.S. Pop, *A numerical scheme for two-scale phase-field models in porous media*, Book of Extended Abstracts of the 6th ECCOMAS Young Investigators Conference, Universitat Politècnica de València, Spain, `https://doi.org/10.4995/YIC2021.2021.12571`.”

Chapter 1

Introduction

Flow and transport models in porous media are encountered in several real-life situations of practical relevance. Prominent in this sense are energy (enhanced oil recovery [100], geothermal energy [129]), environmental or civil engineering (geological CO2 sequestration [48], concrete carbonation [112]), technological applications (fuel cells [11, 68], nano-materials [188]) and biological systems (blood vessels [183], biofilms [98]). Common for all these applications is that the flow and transport processes occur and interact at different scales for different applications [62,74,181,191]. This complexity makes the mathematical and numerical analysis of such processes very challenging. Since the past half-century, upscaling of such processes from a micro to a macro scale has been a common practice among researchers [56,187]. The goal is to find effective (upscaled) models which are not only less complex to describe but also very efficient to simulate.

In this thesis, we derive mathematical models for flow and transport problems in porous media involving different scales. More specifically, we start with mathematical models valid at the micro scale, here it is referred to as the pore scale. Later, we derive upscaled models valid at a much larger scale, namely the scale of the application. The larger scale of our interest is commonly referred to as the Darcy scale and can be viewed as a macro scale in contrast to the pore scale. In short, the goal is to derive upscaled models with a focus on two-phase or unsaturated flow coupled with the transport of a soluble surfactant.

In Section 1.1, we briefly discuss the physical processes regarding two-phase flow in porous media. Subsequently, we provide a short overview of the considered mathematical models at the scale of pores in Section 1.2.1, and further, we discuss commonly used models at the Darcy scale in Section 1.2.2. We present upscaling methods that bridge the gap between pore-scale and Darcy-scale models in Section 1.3. In Section 1.4, we introduce the numerical schemes used to solve the resulting Darcy-scale models. We formulate the main goals of the thesis in Section 1.5. Finally, we summarize the thesis in Section 1.6.

1.1 Physical processes in porous media

A porous medium is a material that contains pores (or voids) and a skeletal structure, the solid grains. The solid grain network may be very complex. Examples of porous media are rocks, soil, cement, wood, cork, nappies and face masks. We are interested in the case when one or more fluids (e.g., liquid and gas) occupy the pore space and species (solute/surfactant) maybe present in the fluids.

The porous medium is "fully saturated" if the entire pore space is filled with only one liquid phase. It is "unsaturated" if the pores are filled only partially with a liquid phase and otherwise by a gas that has no impact on the overall flow. If two liquids are present and influence each other, one deals with "two-phase" flow in a porous medium. For example, in groundwater hydrology, one deals with the flow of two fluids (water and air) in the subsurface, which is a porous medium. In oil recovery applications, two fluids (water and oil) flow through the reservoir rock. The first application is an example of unsaturated flow, while the latter is a two-phase flow system.

The two-phase or, more general, the multi-phase and multi-component flow and transport through a porous medium is inherently a process occurring at multiple scales [79]. Here we consider the pore scale as a micro scale, as opposed to the Darcy scale (the macro scale), where a volume containing both solid grains and pores is considered as representative elementary volume (REV) [20]). This volume is the smallest volume at which average properties do not vary with the change in REV size. In Figure 1.1, pore and Darcy scales are illustrated, where zooming in at the Darcy scale shows a detailed structure of the pore scale with two fluids and a surfactant. Darcy-scale processes occur in scales ranging from centimeters up to kilometers. On the other hand, those at the pore scale are within scales of millimeters or micrometers or even below. Hence there exists a clear scale separation between these scales.

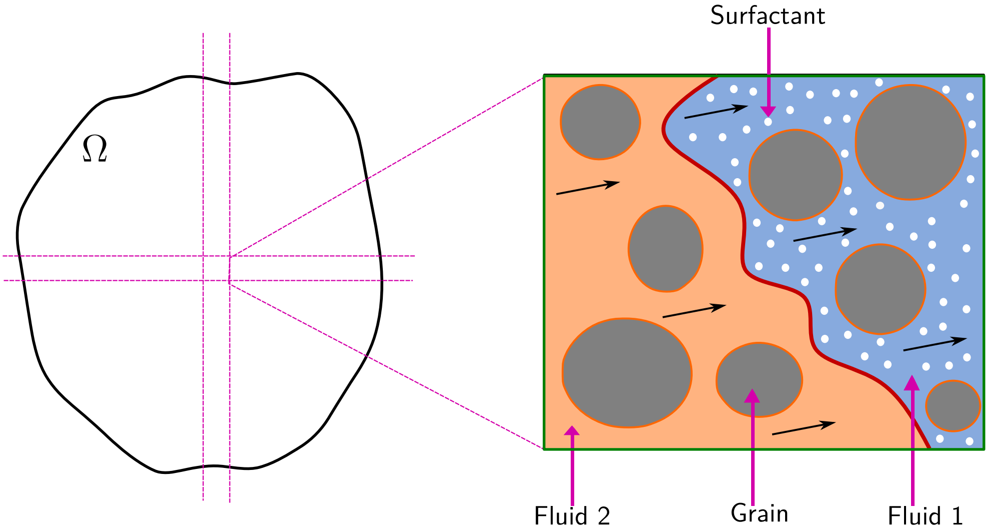

Figure 1.1: The left figure is a schematic representation of the porous medium Ω at the Darcy scale. The right figure is the representation of a two-phase flow and surfactant transport system with an evolving fluid-fluid interface (colored red) at the pore scale. It presents grains (colored gray) surrounded by void space (the pores) occupied by two immiscible fluids (blue and orange) and surfactant species (white dots). Black arrows indicate fluid velocity. The internal solid-fluid boundaries of the void space are colored orange and the outer one is colored green.

Since the total number of grains and voids of the porous medium is enormous, simulating flow is not feasible at the pore scale. The grain and void spaces, and the two (or more) fluid phases cannot be explicitly separated at the Darcy scale but can be modelled through average quantities such as porosity and saturation. For many applications, one is only interested in the average quantities at the Darcy scale. Therefore, a Darcy-scale model would be suitable. However, one would be interested in a Darcy-scale model that incorporates pore-scale influences. The derivation of Darcy-scale equations incorporating the pore-scale effects is one important research topic of flow in porous media. This derivation is a type of upscaling.

1.1.1 Flow in porous media

At the Darcy scale, the flow of each fluid phase is typically described with the help of Darcy-scale quantities like the absolute permeability and the fluid-specific relative permeability. The absolute permeability depends strictly on the composition and topology of the solid part of the medium. The relative permeability is considered to be a function of saturation.

Based on experiments, Henry Darcy [58] formulated one of the first mathematical models for the Darcy-scale flow in a porous medium. In these experiments, one fluid phase occupied the entire pore volume of the medium, and hence the porous medium was fully saturated. The empirical law observed by Darcy shows that permeability links the pressure gradient to the fluid flow velocity at the Darcy scale.

We mention [40,152,182] among the first attempts to model unsaturated flow through porous media. In these studies, Darcy's law for the saturated case is extended to unsaturated media, namely Richard's equation [152]. In the setting of two-phase flow, we mention the Buckley-Leverett equation [41]. It describes the average displacement behaviour of the mixtures of multi-phase (oil-water-gas) flow through the sand. The Buckley-Leverett equation is nothing but generalized Darcy's laws for multi-phase flow.

Traditionally, the Darcy-scale flow models involve the mass balance equations for each fluid phase, the Darcy laws for each fluid velocity with a saturation-dependent (relative) permeability, and the phase-pressure difference (the capillary pressure). In general, the permeability and capillary pressure depend nonlinearly and monotonically on the saturation of the (wetting) fluid. These nonlinear relations have been formulated based on experimental observations and lack a mathematical derivation from governing pore-scale models (see [20, 78]).

Although extensively used, traditional Darcy-scale models need improvements, as also motivated by experimental results. As shown in [121], the capillary pressure-saturation function also depends on the process (infiltration or drainage). Furthermore, the breakthrough curves determined in [26] between the phase-pressure difference and the saturation reveal that the dependency is not necessarily monotone. Next, there is indirect evidence of the limited validity of assuming a linear relationship between the capillary pressure and the saturation. In this respect, we mention that effects like saturation overshoot or finger formation, clearly evidenced in experiments reported, e.g., in [59, 138, 164, 190] and [70, 151], cannot be modeled by using traditional Darcy-scale models.

Multiple extensions of Darcy's law for unsaturated or two-phase flow in porous media have been proposed to overcome these drawbacks. In this sense, we start by mentioning [3, 21, 22, 135, 173], where different play-type hysteresis models are proposed (an overview is provided in [159]), and we refer to [21, 77] for models incorporating dynamic effects in the capillary pressure - saturation dependency. Inspired by the thin-film model proposed in [85], a phase-field model involving the second-order spatial derivative of the saturation in the capillary pressure is proposed in [9, 54, 55] for unsaturated flow in porous media. In [61], a model accounting for the differences between percolating and non-percolating parts of fluid is discussed, whereas the interfacial area concept is incorporated in the porous media flow models discussed in [76, 125, 137].

The effectiveness of such extensions in capturing phenomena like saturation overshoot and fingering is evidenced in [50, 55, 80, 97, 144, 155, 171, 174, 186, 190]. Two different major strategies can be observed in these papers. The first one is to present numerical simulations for the extended models, aiming at reproducing the experimental results quantitatively. The second strategy relies on mathematical analysis, particularly on the travelling waves. The focus is mainly on the qualitative behaviour of the solution and, in particular, the dependence on the parameters appearing in the extended models.

Alternatively to the extended models discussed above, one can consider mathematical models that are valid at the scale of pores, which lead to models posed in a complex domain consisting of the entire pore space of the porous medium. Such an approach allows for incorporating detailed pore-scale physics, which is generally better understood. A pore-scale model is useful for formulating physical processes on local pore structures in the porous medium. Pore-scale model equations are valid separately in the pore and grain spaces. This difference between pore and grain space allows a more precise mathematical formulation of the appropriate physical processes.

Pore-scale modeling is very useful for simulating fluid flow in the pore space. We refer to [72, 87, 168] for a review of numerical approaches for simulation of fluid flow at the pore scale. Closer to the studied case in Chapter 2 are [111] and [110], where direct numerical simulation tools are developed to understand the flow and the interface dynamics at the scale of pores, and these tools are then incorporated into a multi-scale simulator. Due to the computational cost, a numerical simulation for the entire domain of interest at such a detailed level remains infeasible for practical applications.

In this thesis, we use upscaling to derive averaged (upscaled) models at the Darcy scale from pore-scale models. These Darcy-scale models incorporate pore-scale effects through upscaled effective (average) quantities. Additionally, upscaled models are computationally less expensive to simulate compared to pore-scale models.

The upscaling of saturated flow in a porous media is well understood (see e.g., [84]) whereas the unsaturated flow or the two-phase, immiscible flow have many unsolved issues. The major challenges are due to the presence of evolving interfaces at the pore scale, which separate the two fluid phases [115] and the modelling of the fluid-fluid interface contact with grain boundaries [108]. In Chapters 2 and 3, we address the first issue due to evolving fluid-fluid interfaces at the pore scale and derive (non-standard) Darcy-scale models using upscaling.

1.1.1.1 Moving fluid-fluid interface

When referring to two fluid phases, a peculiar aspect of the pore-scale modelling is that, since the fluids are assumed immiscible, they are separated at the pore scale by an interface having a location that is not known a-priori. Its location depends on the surface tension between the fluids and on the fluid velocities (which may depend on the surfactant). In mathematical terms, this interface represents a free boundary in the model.

The fluid-fluid interface separates the regions occupied by the two fluids. At the Darcy scale, the interface determines the saturation of both fluids. However, simply knowing the saturation of the two fluids is not sufficient for describing the flow of both phases. It is crucial to quantitatively not only understand, but rather include the underlying processes that affect the interface between the two fluids. Further, the dynamics of the triple points in $\mathbb{R}^2$, or curves in $\mathbb{R}^3$ where the interface meets the solid grain need to be taken into account.

When dealing with free-boundary problems, one can consider several mathematical modelling strategies. The simplest situation is when the domain is either one-dimensional, or has a rectangular or cylindrical structure, and the free boundary is along the symmetry axis. In this case, one can identify the free boundary through the distance to the domain boundary along the symmetry axis. Such a strategy is adopted in [117] and in Chapter 2 of this thesis. In a similar context, but with a free boundary transversal to the symmetry axis, parametric curves or surfaces have been used to model two-phase flow in a rectangular or cylindrical structure [108, 115].

More realistic situations can be considered when assuming periodically distributed grains, which will be done in Chapter 3. In this case, the simplest approach is to assume a radial symmetry for the grain and the free boundary. Then, the free boundary can be identified through the radius of the curve/surface, as done, e.g., in [65, 167], where a model for water diffusion into absorbent particles is proposed. If radial symmetry cannot be assumed, level sets can be used to identify the free boundary, e.g., [34, 36, 67, 177].

In the sharp-interface approaches mentioned above, the main difficulty in the analysis and numerical simulation of such mathematical models is having discontinuities on each side of the interface and that the domains of the two fluids change with time. To avoid discontinuities and dealing with time-dependent domains, diffuse-interface approach, e.g., phase-field (see [2]), offers a good alternative. In this case, the sharp interface is approximated by a diffuse interface region and the model is defined in a fixed domain [46, 106]. The phase-field indicator is a smooth approximation of, say, the characteristic function of the domain occupied by one of the fluid phases. Then, a critical aspect is to guarantee that, when the diffuse interface width approaches 0, the model reduces to the original one, involving sharp interfaces. Phase-field models can capture topological changes such as merging and splitting and have thus been used successfully for direct numerical simulation of multi-phase flows [28, 90]. For different applications, we refer to [37, 180], where a (pore-scale) phase-field model is developed for a precipitation-dissolution model involving one fluid phase, to [150, 153] for two fluid phases, to [73] for two-phase flow including temperature-dependent surface tension, and to [103, 120] for fracture propagation in poroelastic media. Figure 1.2 shows a schematic representation of the sharp interface versus the phase-field approximation of the free boundary between the two fluids.

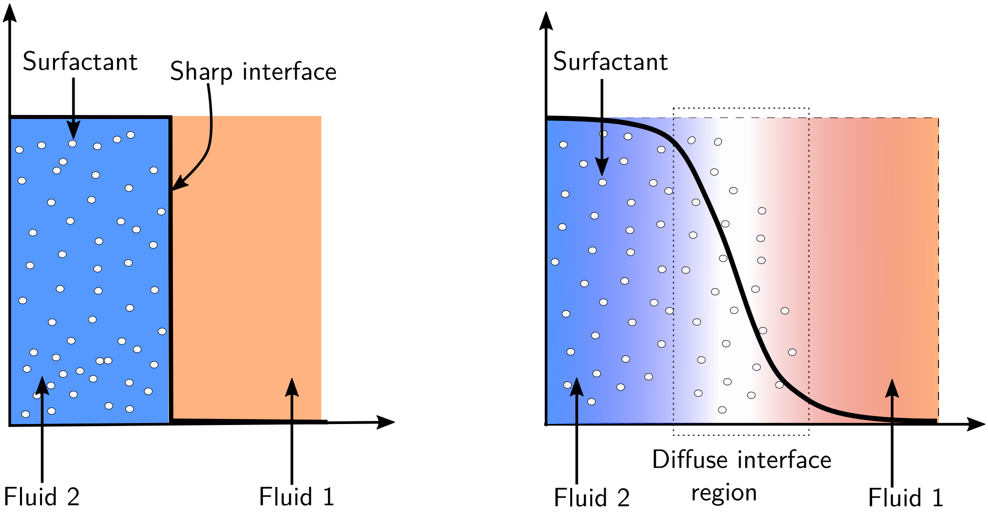

Figure 1.2: Schematic representation of the sharp interface versus diffuse interface to model a freely moving fluid-fluid interface.

1.1.2 Surfactant transport in a porous media

The surface tension between the two fluid phases can be influenced by the presence of a surfactant in one or both fluids in multiphase flow in porous media. Important examples in this sense are enhanced oil recovery [100, 185] or applications involving, e.g., microfluidics [94,123] or thin-film flows [53,75]. For more examples of models that account for surfactant transport in porous media, we also refer to [86, 91, 99, 124, 166].

The transport of surfactant in a fluid is determined by the fluid flow velocity and by the concentration gradient of the surfactant. A convection-diffusion equation is used at the pore scale to model the surfactant transport. Moreover, the surfactant can alter the surface tension at the fluid-fluid interface and create a surface tension gradient, which influences the capillary pressure and hence the overall flow. Such processes encountered at the pore scale have impact at the Darcy scale. The flow driven by variations in the surface tension is known as the Marangoni effect [160]. It is usually caused by surfactant or concentration gradients and helps the fluids to move from the region with higher concentration of surfactants to that with lower concentration. Hence, the transport of surfactant concentration can not be ignored. In many industrial applications such as microfluidics [63] and enhanced oil recovery (EOR) (see [83, 126, 163]), Marangoni effects play an important role.

In surfactant EOR, two fluids (water-oil) occupy the pores, and a surfactant is added to reduce the surface/interfacial tension (IFT) between trapped oil and injected water in the reservoir rock. The surface tension gradient drives the oil to move from the region with higher concentration of surfactant to that with the lower concentration. Consequently, the surfactant increases the mobilization of oil left inside the pores of the rock after primary or secondary recovery and therefore enhances the recovery of oil. See Figure 1.3 for the graphical illustration of the IFT reduction mechanism in the surfactant EOR process.

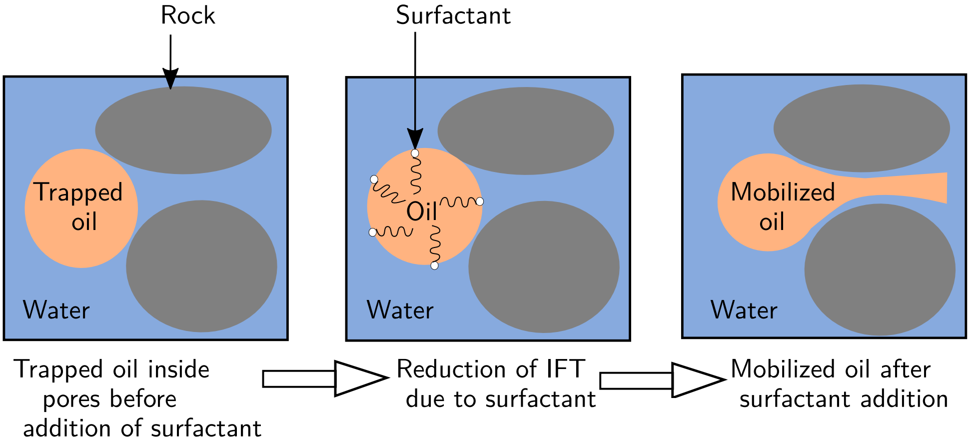

Figure 1.3: A schematic representation of the working principle of surfactant in EOR.

1.2 Overview of mathematical models in porous media

This section focuses on the single-phase and two-phase/unsaturated flow and surfactant transport models in porous media. First, the governing model equations for flow and transport are introduced at the pore scale, and later the commonly used model equations at the Darcy scale are presented.

1.2.1 Pore-scale models

We consider here pore-scale models for single-phase, two-phase or unsaturated flow through a porous medium. The pore-scale models also consider the possibility of one fluid transporting a (soluble) surfactant species.

The structure of the pore-scale models is described in Sections 1.2.1.1-1.2.1.4, which include two major components: the flow of the two separate phases and the diffusion and transport of the surfactant. Additionally, initial and boundary conditions are specified to complete the model equations. In Section 1.3 and Chapter 2, we use these pore-scale models to derive Darcy-scale models.

1.2.1.1 Single-phase flow

We start by presenting the model for single-phase flow, where the entire pore space is occupied by one fluid. The fluid is assumed incompressible, and its density and viscosity are assumed constant. Figure 1.4 sketches the geometry of a single-phase flow system in a general porous medium.

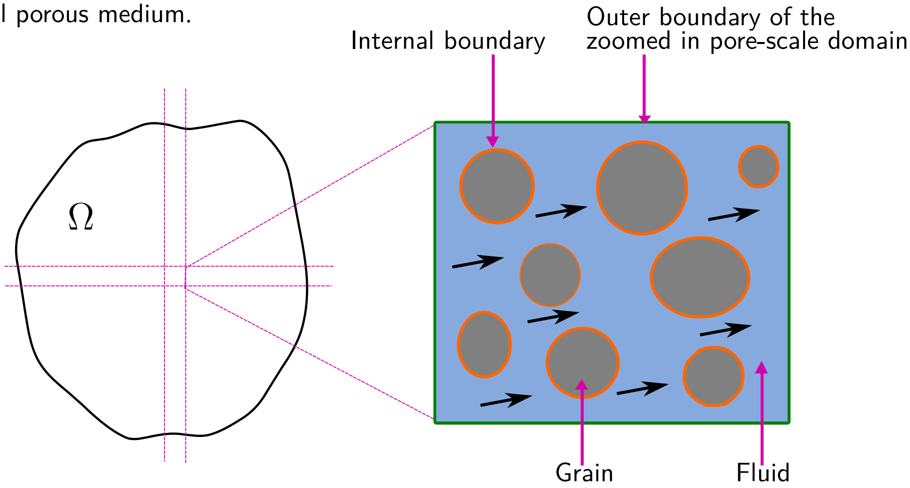

Figure 1.4: The left figure is a schematic representation of the porous medium Ω at the Darcy scale. The right figure is the representation of single-phase flow at the pore scale. It presents grains (colored gray) surrounded by void space (the pores) occupied by single fluid (blue). The internal solid-fluid boundaries of the void space is colored orange and the outer one is colored green. Black arrows indicate fluid velocity.

In what follows, we let Ω denote the entire domain (the porous medium), which consist of a solid grain space and a fluid-filled pore space $\Omega_{\mathcal{P}}$. We define $(0, \infty)$ the time interval in which the flow takes place and write $Q = \Omega_{\mathcal{P}} \times (0, \infty)$.

Let μ, ρ denote the viscosity and density of the fluid. Then, for any time $t > 0$, the flow of a single-phase fluid is modelled by the incompressible Navier-Stokes equations (see [24, 130]), which describe the conservation of momentum and mass,

$$\rho \partial_t \mathbf{v} + \rho \left(\mathbf{v} \cdot \nabla \right) \mathbf{v} + \nabla p - \mu \nabla^2 \mathbf{v} = 0, \qquad \text{in } Q, \tag{1.1}$$

$$\nabla \cdot \mathbf{v} = 0, \qquad \text{in } Q, \tag{1.2}$$

where $\mathbf{v}$ is the velocity and p is the pressure. For simplicity, the flow is assumed horizontal, so that gravity effects are neglected.

The boundary of $\Omega_{\mathcal{P}}$ consist of the inner part $\Gamma_{\mathcal{G}}$, which is the union of all grain boundaries of the outer part and the outert part, $\partial\Omega_{\mathcal{P}} \setminus \Gamma_{\mathcal{G}}$, where $\partial\Omega_{\mathcal{P}} = \overline{\Omega_{\mathcal{P}}} \setminus \Omega_{\mathcal{P}}$, which is the union of all pore boundaries. In Chapters 2 and 3, we assume that the grain boundary is impermeable to the fluids. Also, there is no-slip along $\Gamma_{\mathcal{G}}$,

$$\mathbf{v} = \mathbf{0}, \text{ on } \Gamma_{\mathcal{G}} \times (0, \infty). \tag{1.3}$$

Note that this condition is appropriate if the Knudsen number Kn> 10 (see [78]). The single-phase model (1.1)-(1.3) is completed by initial and boundary conditions. For example, one can use an initial velocity and periodic boundary conditions on $\partial\Omega_{\mathcal{P}}$ to close the system.

By neglecting the inertia effects and assuming a low Reynolds numbers, instead of (1.1), one can use the Stokes equations (see [81])

$$\mu \nabla^2 \mathbf{v} = \nabla p, \text{ in } Q. \tag{1.4}$$

In Section 1.3, we introduce upscaling methods used in this thesis and for simplicity, we use Stokes equation (1.4) and (1.2) to describe the flow. Whereas in Chapters 2 and 3, we use the Navier-Stokes equations (1.1)-(1.2) to fully describe the flow.

1.2.1.2 Two-phase flow

We extend the situation before by assuming that two incompressible and immiscible fluid phases occupy the pore space $\Omega_{\mathcal{P}}$. The model equations for two-phase flow at the pore scale are similar to those in the single-phase flow case. The main difference is that one needs to solve the conservation laws (momentum (1.1) and mass (1.2)) for each phase $\alpha = I, II$. Moreover, these are posed in time-dependent subdomains $Q_{(\alpha)} = \{\Omega_{(\alpha)}(t) \times t | t > 0\}$, which correspond to the parts of $\Omega_{\mathcal{P}}$ occupied by fluid α. The velocity vectors are denoted by $\mathbf{v}_{(\alpha)} = \left(v_{(\alpha,1)}, v_{(\alpha,2)}\right)$, where the index $\alpha = I, II$ distinguishes between the non-wetting (fluid-I) and the wetting fluid (fluid-II), respectively. Let $\mu_{(\alpha)}$ and $\rho_{(\alpha)}$ denote the (constant) viscosity and density of phase $\alpha = I, II$. Then the momentum and mass conservation laws are

$$\rho_{(\alpha)} \partial_t \mathbf{v}_{(\alpha)} + \rho_{(\alpha)} \left(\mathbf{v}_{(\alpha)} \cdot \nabla\right) \mathbf{v}_{(\alpha)} + \nabla p_{(\alpha)} - \mu_{(\alpha)} \nabla^2 \mathbf{v}_{(\alpha)} = 0, \qquad \text{in } Q_{(\alpha)}, \tag{1.5}$$

$$\nabla \cdot \mathbf{v}_{(\alpha)} = 0, \qquad \text{in } Q_{(\alpha)}, \tag{1.6}$$

where $p_{(\alpha)}$ denotes the pressure of phase α. As in the case of single-phase flow, gravity effects are neglected. Figure 1.5 sketches the geometry of a two-phase flow system in a general porous medium.

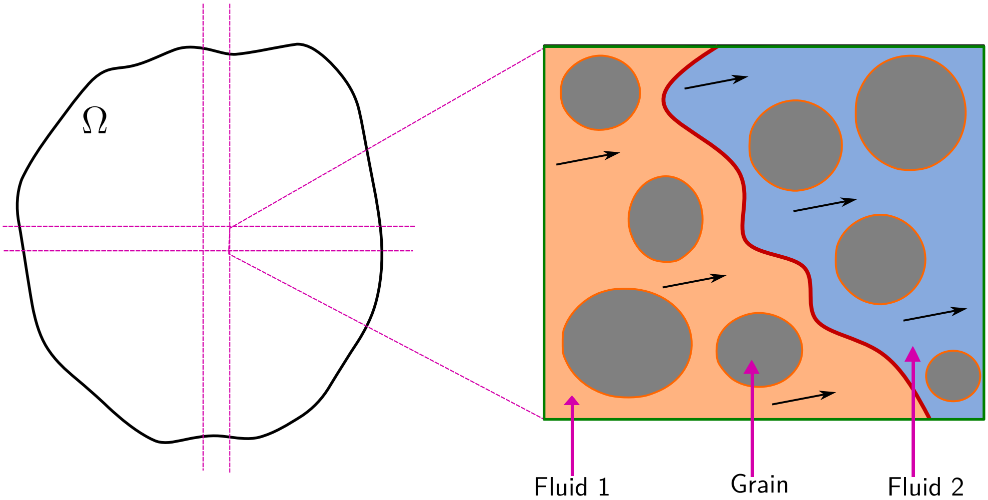

Figure 1.5: The left figure is a schematic representation of the porous medium Ω at the Darcy scale. The right figure is the representation of a two-phase flow system with evolving fluid-fluid interface (colored red) at the pore scale. It presents grains (colored gray) surrounded by void space (the pores) occupied by two immiscible fluids (blue and orange). Black arrows indicate fluid velocity. The internal solid-fluid boundaries of the void space is colored orange and the outer one is colored green.

To solve the two-phase flow model (1.5)-(1.6), we need to prescribe appropriate initial and boundary conditions. Furthermore, the models for phases I and II are coupled through boundary conditions at the fluid-fluid interface $\Gamma(t)$. We assume that the two fluids are separated by a sharp interface with zero thickness which changes with time. The movement is not known a-priori, hence is a moving boundary at $\Gamma(t)$. Figure 1.6 presents a schematic representation of fluid-fluid interface $\Gamma(t)$.

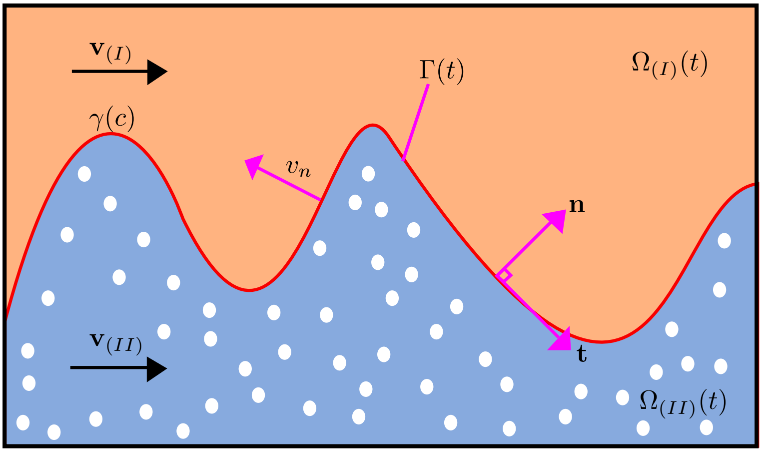

Figure 1.6: Schematic representation of two-phase flow and surfactant transport system with evolving fluid-fluid interface (colored red). It presents two immiscible fluids (blue and orange) and surfactant species (white dots). Black arrows indicate fluid velocity.

First, we assume that the fluids have no phase change. Hence there is no mass transfer across the interface $\Gamma(t)$ and therefore the velocities of the two fluids are equal at $\Gamma(t)$,

$$\mathbf{v}_{(I)} = \mathbf{v}_{(II)}, \text{ on } \{\Gamma(t) \times \{t\}, t > 0\}. \tag{1.7}$$

Second, we assume that the normal velocity v_n of $\Gamma(t)$, equals the normal velocities of the two fluids,

$$\mathbf{v}_{(\alpha)} \cdot \mathbf{n} = v_n, \text{ on } \{\Gamma(t) \times \{t\}, t > 0\}, \text{ for } \alpha = I, II, \tag{1.8}$$

where $\mathbf{n}$ denote the unit normal vector on $\Gamma(t)$ pointing into $\Omega_{(I)}(t)$ from $\Omega_{(II)}(t)$ and $\mathbf{t}$ the unit tangent vector.

The flow and the surface tension γ between the fluids give rise to a stress at the fluid-fluid interface $\Gamma(t)$. We use the stress tensors

$$\mathbf{T}_{(\alpha)} := -p_{(\alpha)}\mathbf{I} + \mu_{(\alpha)}\left(\left(\nabla \mathbf{v}_{(\alpha)}\right) + \left(\nabla \mathbf{v}_{(\alpha)}\right)^T\right) \ (\alpha = I, II).$$

If the surface tension γ is affected by the presence of a surfactant having concentration c in one of the fluids, one has γ as a function of c. For example, in [165] the following law is proposed

$$\gamma(c) = \gamma_{\text{ref}}\left(1 - b\ \ln\left(\frac{c}{a\ c_{\text{ref}}} + 1\right)\right), \tag{1.9}$$

where a, b are constants, γ_{ref} is a reference surface tension and c_{ref} is a reference concentration. The tangential stress gradient of the surface tension is

$$\nabla_s \gamma(c) := \nabla\ \gamma(c) - \mathbf{n}\left(\mathbf{n} \cdot \nabla\ \gamma(c)\right).$$

With this, the third boundary condition on the fluid-fluid interface reads (see [102])

$$\left(\mathbf{T}_{(I)} - \mathbf{T}_{(II)}\right) \cdot \mathbf{n} = \gamma(c)\ \ (\nabla \cdot \mathbf{n})\ \ \mathbf{n} - \nabla_s\ \gamma(c), \text{ on } \{\Gamma(t) \times \{t\}, t > 0\}.$$

This jump can be written in terms of the normal and the tangential components. At $\Gamma(t)$, the jump (see [105]) in the normal component of the normal stress is

$$\left(\left(\mathbf{T}_{(I)} - \mathbf{T}_{(II)}\right) \cdot \mathbf{n}\right) \cdot \mathbf{n} = \gamma(c)\ \ (\nabla \cdot \mathbf{n}), \text{ on } \{\Gamma(t) \times \{t\}, t > 0\}. \tag{1.10}$$

Due to the dependency of the surface tension γ on c the tangential component of the normal stress has a jump at $\Gamma(t)$ (the Marangoni effect),

$$\left(\left(\mathbf{T}_{(I)} - \mathbf{T}_{(II)}\right) \cdot \mathbf{n}\right) \cdot \mathbf{t} = -\mathbf{t} \cdot \nabla\ \gamma(c), \text{ on } \{\Gamma(t) \times \{t\}, t > 0\}, \tag{1.11}$$

which helps the flow of the fluids with lower surface tension going towards the region of larger surface tension.

For $\alpha = I, II$, on the solid-fluid interfaces $\Gamma_{\mathcal{G}}$, we assume no-slip for both fluids,

$$\mathbf{v}_{(\alpha)} = \mathbf{0}, \text{ on } \Gamma_{\mathcal{G}} \text{ and for } t > 0. \tag{1.12}$$

Finally, the initial velocity for each phase α must be specified to close the system.

Remark. *Whenever the surface tension is constant, as happening, e.g., in the absence of a surfactant or with a constant surface tension, the tangential components of the normal stresses are equal at* $\Gamma(t)$*. In this case,* $\gamma(c) = \gamma$*, and* (1.10)-(1.11) *reduce to*

$$\Big(\left(\mathbf{T}_{(I)} - \mathbf{T}_{(II)}\right) \cdot \mathbf{n}\Big) \cdot \mathbf{n} = \gamma \ (\nabla \cdot \mathbf{n}), \qquad \textit{on } \{\Gamma(t) \times \{t\}, t > 0\}, \tag{1.13}$$

$$\Big(\left(\mathbf{T}_{(I)} - \mathbf{T}_{(II)}\right) \cdot \mathbf{n}\Big) \cdot \mathbf{t} = 0, \qquad \textit{on } \{\Gamma(t) \times \{t\}, t > 0\}. \tag{1.14}$$

1.2.1.3 Unsaturated flow

Unsaturated flow is a special case of the two-phase flow model described in Section 1.2.1.2. For unsaturated flow, we assume that the pressure in fluid-I is constant and that its mobility is infinite. Essentially, this means that fluid-I plays no role for the flow of fluid-II. This situation appears, e.g., if fluid-I is air and is connected to the atmosphere. Then, the unknowns are reduced to those corresponding to fluid-II. The model equations in Section 1.2.1.2 are hence simplified by giving up the equations for $\alpha = I$, keeping only the Navier-Stokes equations in the region occupied by fluid-II,

$$\begin{aligned} &\rho_{(II)}\partial_t \mathbf{v}_{(II)} + \rho_{(II)} \left(\mathbf{v}_{(II)} \cdot \nabla\right) \mathbf{v}_{(II)} + \nabla p_{(II)} - \mu_{(II)} \nabla^2 \mathbf{v}_{(II)} = 0, && \text{in } Q_{(II)}, \\ &\nabla \cdot \mathbf{v}_{(II)} = 0, && \text{in } Q_{(II)}. \end{aligned}$$

Moreover, if we assume that the surface tension is constant, at the gas-fluid interface $\Gamma(t)$, the boundary conditions (1.8) and (1.10)-(1.11) reduce to

$$\begin{aligned} \mathbf{v}_{(II)} \cdot \mathbf{n} &= v_n, && \text{on } \{\Gamma(t) \times \{t\}, t > 0\}, \\ \Big(\mathbf{T}_{(II)} \cdot \mathbf{n}\Big) \cdot \mathbf{n} &= -\gamma(\nabla \cdot \mathbf{n}), && \text{on } \{\Gamma(t) \times \{t\}, t > 0\}, \\ \Big(\mathbf{T}_{(II)} \cdot \mathbf{n}\Big) \cdot \mathbf{t} &= 0, && \text{on } \{\Gamma(t) \times \{t\}, t > 0\}. \end{aligned}$$

We still assume a no-slip boundary condition (1.12) for phase $\alpha = II$ on the fluid-solid interface $\Gamma_{\mathcal{G}}$ and the initial velocity for phase $\alpha = II$ is needed to close the unsaturated flow model.

1.2.1.4 Surfactant transport

We consider one chemical species, a surfactant that is only soluble in one fluid, say in fluid-II. Its molar concentration is denoted by c. Additionally, there is no mass transfer of the surfactant from fluid-II to fluid-I. Hence, the molar concentration of the surfactant in fluid-I is zero. The surfactant transport is due to the fluid flow and the concentration gradient, resulting in

$$\partial_t c + \nabla \cdot \left(-D\nabla c + \mathbf{v}_{(II)} c\right) = 0, \text{ in } Q_{(II)}, \tag{1.15}$$

where D is a (constant) diffusion coefficient. Figure 1.1 sketches the geometry of a two-phase flow and surfactant transport system in a general porous medium.

At $\Gamma(t)$, one has the mass balance for the solute, while the normal flux into the solid matrix is zero at $\Gamma_{\mathcal{G}}$,

$$\begin{aligned} \left(-D\nabla c + \mathbf{v}_{(II)} c\right) \cdot \mathbf{n} &= c v_n, && \text{on } \{\Gamma(t) \times \{t\}, t > 0\}, \\ \left(-D\nabla c + \mathbf{v}_{(II)} c\right) \cdot \mathbf{n} &= 0, && \text{on } \Gamma_{\mathcal{G}} \text{ and for } t > 0. \end{aligned}$$

Finally, one needs an initial distribution for the surfactant concentration to complete the transport model.

1.2.2 Darcy-scale models

In this section, we discuss existing Darcy-scale models for flow and surfactant transport in a porous medium. In Darcy-scale models no distinction is made between the pore space and the skeleton of the porous medium. These models describe the averaged behavior of the system by considering so-called representative elementary volumes (REV) [20] where detailed information from the pore scale is not available. Note that gravity effects are neglected here as in the previous Section 1.2.1.

1.2.2.1 Single-phase flow

We begin with a single-phase flow in a $\mathtt{d}$-dimensional porous medium $\Omega \subset \mathbb{R}^{\mathtt{d}}(\mathtt{d} \in \{2,3\})$. Its outer boundary is $\partial\Omega$. Let $\mathcal{K} \in \mathbb{R}^{d\times d}$ be the absolute (or intrinsic) permeability of the porous medium. Typically, $\mathcal{K}$ is a symmetric positive definite tensor. In the case of an isotropic medium, the permeability tensor reduces to a scalar quantity. The Darcy-scale model equations for the incompressible single-phase flow in a porous medium are the Darcy law [58] and the conservation of mass,

$$\overline{\mathbf{v}} = -\frac{\mathcal{K}}{\mu}\nabla p, \text{ in } \Omega, \tag{1.16}$$

$$\nabla \cdot \overline{\mathbf{v}} = q, \text{ in } \Omega, \tag{1.17}$$

where $\overline{\mathbf{v}}$ is the Darcy (or volumetric) velocity, p is the fluid pressure and q stands for internal sources or sinks (depending on the sign of q). The model equations (1.16)-(1.17) are the simplest equations for modelling single-phase flow in a porous medium.

Boundary conditions have to be specified to complete the single-phase flow model. For simplicity, one can use the homogeneous Dirichlet boundary conditions on $\partial\Omega$ for the pressure.

1.2.2.2 Two-phase flow

If two fluids are present in the porous medium, we consider fluid-I as non-wetting and fluid-II as wetting. Let $S_{(\alpha)}$ be the saturation (the ratio of fluid α volume in an REV, and of the REV volume) of phase $\alpha, \alpha \in \{I, II\}$. Additionally, let Φ be the porosity of the porous medium (the volume of the pore space in an REV over the volume of the REV). At the Darcy scale, the model equations for two-phase flow are given by the mass conservation of the fluid phases $\alpha = I, II$ (see [20, 78])

$$\Phi\partial_t S_{(\alpha)} + \nabla \cdot \overline{\mathbf{v}}_{(\alpha)} = q_{(\alpha)}, \text{ in } \Omega \times (0, \infty), \tag{1.18}$$

where $\overline{\mathbf{v}}_{(\alpha)}$ is the volumetric flux, and $q_{(\alpha)}$ is the source/sink term of phase α. With $p_{(\alpha)}$ being the pressure, $\overline{\mathbf{v}}_{(\alpha)}$ satisfies the Darcy-Buckingham law (see [20])

$$\overline{\mathbf{v}}_{(\alpha)} = -\frac{\mathcal{K}\, k_{(r,\alpha)}}{\mu_{(\alpha)}} \nabla p_{(\alpha)}, \text{ in } \Omega \times (0, \infty). \tag{1.19}$$

Here $\mu_{(\alpha)}$ is the dynamic (constant) viscosity of phase α. Further $k_{(r,\alpha)}$ denotes the relative permeability and it models the relative transmigration rate of phase α through the medium. This function is usually obtained from experimental observations.

The model equations (1.18)-(1.19) are the typically used model equations for modelling two-phase flow in a porous medium. However, they do not form a closed system. To solve this system, one needs additional closure relationships. By the definition of saturation, one has $S_{(\alpha)} \in [0, 1]$. Since the voids are occupied by either phase, the first closure relation is

$$S_{(I)} + S_{(II)} = 1. \tag{1.20}$$

Secondly, the relative permeability is assumed to be a function of saturation

$$k_{(r,\alpha)} := k_{(r,\alpha)}(S_{(II)}),$$

which is typically a monotonic function. In standard flow models, the phase pressure difference, which is called the capillary pressure, is also assumed to be a function of the saturation,

$$p_{(I)} - p_{(II)} = p_c(S_{(II)}). \tag{1.21}$$

In practice, $p_c(S_{(II)})$ is assumed to be a monotonically decreasing function. Commonly used $p_c - S_{(II)}$-relationships are by Brooks-Corey and van Genuchten (see [38, 39, 175]). The van Genuchten and Brooks-Corey models are often combined with Mualem and Burdine relationships [44, 122] to obtain the $k_{(r,\alpha)} - S_{(II)}$-dependency.

To complete the two-phase flow models at the Darcy scale, one needs to consider appropriate initial and boundary conditions. For instance, one can prescribe Dirichlet boundary conditions on $\partial\Omega$ for phase pressure or saturation. Also the initial saturation must be prescribed.

These typical standard models (1.18)-(1.21) for two-phase flow have some limitations. The constitutive relationships are derived empirically under equilibrium (static or no flow) conditions which can not incorporate all the dynamics of pore-scale processes and their (non-equilibrium) effects (fluid-fluid interface, interfacial surface tension, immiscibility etc.) that alter the fluid distributions in the porous medium. The scaling functions for capillary pressure are not a monotonic function of saturation, but several curves are present for the same medium. More precisely, they are time-dependent and can not describe effects due to hysteresis (or memory effects) and dynamic capillarity [121]. Consequently, using traditional equilibrium models for two-phase flow, one can not address non-monotonic phenomena such as saturation overshoots and gravity driven fingering effects observed by experiments [60, 71]. Examples of non-standard two-phase flow models which incorporate non-monotonic effects and dynamics of the capillary pressure are [3, 21, 82, 93, 145, 173].

As an alternative to the mentioned extended models, in Chapters 2-3, we employ formal upscaling and use asymptotic expansion methods to derive non-standard Darcy-scale models for two-phase flow accounting for the behavior of the fluid-fluid interface at the pore scale.

1.2.2.3 Unsaturated flow

The Darcy-scale model equations for unsaturated flow in a porous medium is similar to the two-phase flow model in Section 1.2.2.2. One only needs the model equations for the (wetting) fluid-II, which is described by the following mass balance equation [20, 78],

$$\Phi\partial_t S_{(II)} + \nabla\cdot\overline{\mathbf{v}}_{(II)} = q_{(II)}, \text{ in } \Omega\times(0,\infty). \tag{1.22}$$

where $S_{(II)}$ is the saturation and $q_{(II)}$ is the source/sink term. Similar as in Section Section 1.2.2.2, one has

$$\overline{\mathbf{v}}_{(II)} = -\frac{\mathcal{K}\, k_{(r,II)}}{\mu_{II}}\nabla p_{(II)}, \text{ in } \Omega\times(0,\infty). \tag{1.23}$$

Combining the Buckingham flux law (1.23) with the mass balance (1.22), one gets

$$\Phi\partial_t S_{(II)} = -\nabla\cdot\left(\frac{\mathcal{K}\,k_{(r,II)}}{\mu_w}\nabla p_{(II)}\right) + q_{(II)},\ \text{in}\ \Omega\times(0,\infty), \tag{1.24}$$

which is the well-known Richards equation.

Note that (1.24) is not closed since it has three unknowns: saturation, pressure, and relative permeability of fluid-II. This is resolved by the closure relationships

$$p_{(II)} := p_c(S_{(II)}),\ \text{and}\ k_{(r,II)} := k_{(r,II)}(S_{(II)}). \tag{1.25}$$

Commonly used relationships for the $p_c - S_{(II)}$ and $k_{(r,II)} - S_{(II)}$-relationships can be found in [38, 39, 44, 122, 175].

To solve the unsaturated model equations, one needs to consider appropriate initial and boundary conditions. For example, one can prescribe the normal Darcy flux at the boundary, and an initial saturation.

1.2.2.4 Surfactant transport

At the Darcy scale, the mass transport of the surfactant concentration c is given by the convection-diffusion equation [78]

$$\Phi\partial_t(S_{(II)}\,c) + \nabla\cdot(\mathbf{J} + \overline{\mathbf{v}}_{(II)}c) = 0,\ \text{in}\ \Omega\times(0,\infty). \tag{1.26}$$

Here $\mathbf{J}$ is given by Fick's law, $\mathbf{J} = -\overline{D}\nabla c$ and $\overline{D}$ is an effective diffusion coefficient. Note that in Chapters chapter 2 and 3, we derive similar Darcy-scale effective equations for surfactant transport by applying upscaling methods from pore-scale equations (1.15). To close the system, an initial concentration profile and boundary conditions are needed.

1.3 Upscaling methods in porous media

In this section, we discuss upscaling methods for problems involving flow and transport in porous media. There are many contributions in the study of upscaling methods for porous media flows such as analytical methods, stochastic methods, numerical methods, see [18,49,56,62,64] for an overview. Here we briefly discuss analytic techniques which are relevant for this thesis. Since pore-scale models are unsuitable for large-scale simulations, the idea of analytic upscaling is to derive the Darcy-scale models by using averaging procedures over the pore scale. As mentioned in Sections 1.2.2.2 and 1.2.2.3, commonly used Darcy-scale models include parameters which need to be determined experimentally and additional effects such as dynamic effects due to evolving interfaces are included ad-hoc or are simply neglected. To overcome such issues, our goal here is to formally derive (averaged) Darcy-scale models based on model formulations from the pore scale, including the effects of the evolving interface. Then one can formulate the expressions for the effective parameters through upscaling.

Various analytic upscaling techniques can be considered to derive Darcy-scale models: transversal averaging, homogenization and volume averaging. Transversal averaging can be applied when a simple geometry (e,g, long, thin tube or strip) is considered (see [33, 108, 116, 117, 134, 162, 179]). Although simplified, upscaling using transversal averaging still provides Darcy-like model equations for effective quantities as in general porous media. In this way, the relevant model components and features can be included in the upscaling and the corresponding Darcy-scale models can be derived for different dominating effects. As in [118], we choose transversal averaging in Chapter 2 for upscaling a model in thin domain with two fluid phases which accounts for the evolution of the fluid-fluid interface due to flow and concentration-dependent surface tension. It is worth to mention that the novelty of our work lies in the fact that we consider different pore-scale regimes in the upscaling analysis and derive non-trivial averaged (upscaled) models at the Darcy scale including physical effects, e.g., Marangoni effects.

Homogenization is widely used for multi-phase flow and transport models in periodically perforated domains, with small-scale heterogeneities. Periodic homogenization provides a powerful framework to derive both the effective parameters and the Darcy-scale equations. It is based on two strong assumptions, scale separation and periodicity [5, 84, 131]. In particular, it uses a scale separation parameter ϵ, to separate the scales into a slow and a fast scale. By assuming $\epsilon \ll 1$, one can introduce two independent variables, a large-scale (slow) variable $\mathbf{x}$ and a small-scale (fast) variable $\mathbf{y} = \frac{\mathbf{x}}{\epsilon}$. The slow scale relates to the averaged behaviour to the system, and the fast scale represents the pore-scale characteristics. Additionally, one assume that all functions of $\mathbf{y}$ are periodic, i.e. the small scale features are periodic. The next stage is the formal analysis of the equations in the limit of $\epsilon \to 0$ by asymptotic expansions [4, 5]. In Chapter 3, we use homogenization trough asymptotic expansions to derive upscaled Darcy-scale models characterized by effective parameters. We refer to [19, 113, 154] which uses periodic homogenization as an upscaling approach for developing two-phase Darcy-scale models. Comparing to [113], we assume a minimal set of assumptions when deriving the upscaled model. There are also many results through rigorous homogenization for two-phase flow which can be obtained under suitable conditions. For example, we refer to [6, 27, 114], where the convergence of the upscaling process is proved by the concept of two-scale convergence. However, the influence of the evolving fluid-fluid interface has not been included in these proofs.

An alternative to homogenization is the method of volume averaging, which has been successfully applied to upscaling two-phase flow in porous media in [51,101,140,141,184]. Using volume averaging method, one needs to develop constitutive relationships in order to close the averaged (upscaled) models for the effective parameters. Whereas there is no need to derive such closure relationships when using homogenization [119,184]. However, one requires local periodicity assumption which is similar to a closure condition.

In this thesis, we use transversal averaging and homogenization together with the asymptotic expansion method. In this context, we mention that asymptotic homogenization methods either in a thin strip or in a periodic porous medium have been applied for many situations in which evolving interfaces are encountered at the pore scale. Examples in this sense are the evolving fluid-solid interface due to mineral precipitation and dissolution, see [33, 34, 35, 95, 157, 178, 179], or due to biofilm growth or other biological processes [98,132,148,149,156,158,176]. In these studies, the derived Darcy-scale models resemble many of the models (Taylor-dispersion model [169], Taylor-Jaffe model [170]) commonly accepted in literature and additional effects (e.g., variations in the temperature) are included by rational approaches. In contrast to these models, we account for two-phase flow with an evolving fluid-fluid interface at the pore scale and include concentration-dependent surface tension effects, on the upscaled, averaged behavior.

In the following, we present the two upscaling approaches: transversal averaging and homogenization. For simplicity, we consider a single-phase flow model and assume that the flow is governed by the Stokes system (1.4) and (1.2). Additionally, we consider a no-slip boundary condition (1.3) on the grain boundary. Namely,

$$\begin{aligned} \mu\Delta\mathbf{v} &= \nabla p, && \text{in } \Omega_{\mathcal{P}}, \\ \nabla\cdot\mathbf{v} &= 0, && \text{in } \Omega_{\mathcal{P}}, \\ \mathbf{v} &= \mathbf{0}, && \text{on } \Gamma_{\mathcal{G}}. \end{aligned} \tag{1.27}$$

Note that in Chapters 2 and 3, we consider a two-phase flow case but the main steps of the formal upscaling is still similar.

In Section 1.3.1, we bring (1.27) to a dimensionless form. Subsequently, in Section 1.3.2, transversal averaging is applied to a thin and long pore representing the local pore geometry (see Figure 1.7) to derive an upscaled model. Later, in Section 1.3.3, homogenization is used to derive the Darcy-scale model for the case of a complex medium, which consists of periodically distributed solid grains surrounded by a connected pore space (see Figure 1.9). To derive the Darcy-scale models using the formal upscaling and asymptotic expansion methods, we follow the procedures outlined in [84].

1.3.1 Dimensionless pore-scale equations

To identify the model components that have a larger or smaller impact than others, we first bring the model to a dimensionless form. The dimensionless model is formulated by relating the dimensional quantities to the reference ones. For the dimensionless pore-scale two-phase flow models, we refer to Chapter 2 and Chapter 3.

To make the equations dimensionless, we introduce a dimensionless scale separation parameter ϵ, which will be necessary for applying the upscaling methods in Sections 1.3.2 and 1.3.3. Typically, ϵ is the ratio of two length scales, the pore scale and the problem related scale, $\epsilon = \frac{l}{x_{\text{ref}}}$. Therefore, ϵ is a small dimensionless parameter.

Table 1.1: Reference variables and their primary dimensions

Reference variables	Description	Primary units
l	pore length	$[m]$
x_{ref}	characteristic length	$[m]$
p_{ref}	pressure	$[\mathrm{kg\ m^{-1}\ s^{-2}}]$
v_{ref}	velocity	$[\mathrm{m\ s^{-1}}]$
μ_{ref}	viscosity	$[\mathrm{kg\ m^{-1}\ s^{-1}}]$

Using the reference variables in Table 1.1, we define the dimensionless model parameters and variables, denoted with a hat

$$\hat{\mathbf{x}} = \frac{\mathbf{x}}{x_{\mathrm{ref}}}, \hat{\mu} = \frac{\mu}{\mu_{\mathrm{ref}}}, \hat{p}^{\epsilon} = \frac{p}{p_{\mathrm{ref}}}, \hat{\mathbf{v}}^{\epsilon} = \frac{\mathbf{v}}{v_{\mathrm{ref}}}, \hat{\nabla} = x_{\mathrm{ref}}\nabla, \tag{1.28}$$

We assume that the reference viscosity is $\mu_{\mathrm{ref}} = \frac{\epsilon^2 p_{\mathrm{ref}} x_{\mathrm{ref}}}{v_{\mathrm{ref}}}$. The fluid viscosity is chosen to scale with ϵ^2 so that viscous forces are balance with the pressure. We need this assumption to derive a non-trivial Darcy-scale model when $\epsilon \to 0$. If viscous forces dominate which corresponds to $\hat{\mu}\epsilon$ or $\hat{\mu}$, then after upscaling, this leads to a "frozen" profile when $\epsilon \to 0$.

Using the dimensionless variables from (1.28) in the Stokes equation (1.27) and applying the chain rule we obtain the dimensionless Stokes model

$$\epsilon^2 \hat{\mu} \hat{\Delta} \hat{\mathbf{v}}^{\epsilon} = \hat{\nabla} \hat{p}^{\epsilon}, \qquad \text{in } \hat{\Omega}_{\mathcal{P}}, \tag{1.29}$$

$$\hat{\nabla} \cdot \hat{\mathbf{v}}^{\epsilon} = 0, \qquad \text{in } \hat{\Omega}_{\mathcal{P}}, \tag{1.30}$$

$$\hat{\mathbf{v}}^{\epsilon} = \mathbf{0}, \qquad \text{on } \hat{\Gamma}_{\mathcal{G}}, \tag{1.31}$$

where $\hat{\Omega}_{\mathcal{P}} = \{\hat{x} | x_{\mathrm{ref}}\, \hat{x} \in \Omega_{\mathcal{P}}\}$.

1.3.2 Upscaling using transversal averaging

In this section, we present the framework of Chapter 2, where the upscaled models for two-phase or unsaturated flow are derived from a pore-scale model defined in a single pore in a porous medium, namely a thin strip. Additionally, here the pore-scale equations are simple Stokes equations whereas in Chapter 2, it is governed by Navier-Stokes equations.

By considering the simplicity of the geometry, as in Chapter 2, asymptotic expansions and transversal averaging are used here for upscaling. To introduce the method, we begin by defining the pore geometry.

1.3.2.1 Geometric settings

Here the geometry is simple and represented by a two-dimensional channel of length L and width l (see Figure 1.7).

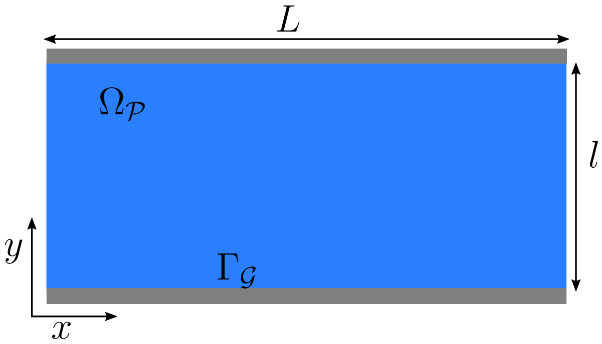

Figure 1.7: A schematic representation of the geometry of the single-phase flow model.

We assume that the width l of the strip is very small compared to the length L. Hence, a scale separation parameter can be identified as the dimensionless ratio, $\epsilon := \frac{l}{L}$. Since it is assumed as a small number, l and L can be treated as the characteristic scales of the pore and Darcy scale, respectively. We denote $\hat{x} = \frac{x}{L}$ and $\hat{y} = \frac{y}{l}$ as a dimensionless variables. The consequence is that $(\hat{x}, \hat{y}) \in (0,1)^2$.

In the dimensionless form, the pore space (domain occupied by the fluid) is the square

$$\hat{\Omega}_{\mathcal{P}} = \{(\hat{x}, \hat{y}) \in \mathbb{R}^2 | 0 \leq \hat{x} \leq 1, 0 \leq \hat{y} \leq 1\},$$

with boundary $\partial\Omega_{\mathcal{P}}$. The boundary between the pore walls and fluid is

$$\hat{\Gamma}_{\mathcal{G}} = \{(\hat{x}, \hat{y}) \in \mathbb{R}^2 | 0 < \hat{x} < 1, \hat{y} \in \{0,1\}\}.$$

The dimensionless model is the Stokes system (1.29)-(1.31). Here we do not specify the inflow and outflow boundary conditions since they are not influencing the upscaling procedure. This is because we assume that there are no boundary layers near the inflow and outflow boundaries. We refer to [131] for more explanations on boundary layers and homogenization.

1.3.2.2 The Darcy-scale model equations

To derive effective equations from the dimensionless single-phase Stokes-model (1.29)-(1.31), we assume scale separation represented by ϵ and use asymptotic expansion method with respect to ϵ. Since in this section only the non-dimensional variables are used, for the ease of presentation the hats are suppressed. We assume that all the variables are smooth and depend regularly on ϵ. Then we apply the homogenization ansatz for the model unknowns p^ϵ and $\mathbf{v}^\epsilon$,

$$\begin{aligned} p^\epsilon(x,y) &= p^0(x,y) + \epsilon p^1(x,y) + \mathcal{O}(\epsilon^2), \\ v_1^\epsilon(x,y) &= v_1^0(x,y) + \epsilon v_1^1(x,y) + \mathcal{O}(\epsilon^2), \\ v_2^\epsilon(x,y) &= v_2^0(x,y) + \epsilon v_2^1(x,y) + \mathcal{O}(\epsilon^2), \end{aligned} \tag{1.32}$$

where $p^{\mathrm{j}}(x,y,t), v_1^{\mathrm{j}}(x,y,t)$ and $v_2^{\mathrm{j}}(x,y,t)$ are functions describing the $\mathcal{O}(\epsilon^{\mathrm{j}})$ order approximation (for $\mathrm{j} = 0, 1, \cdots$) of pressure and velocity components in x- and y-directions, respectively.

Since the scaling of the spatial coordinates is different, the derivatives also need to be rescaled. Hence, the dimensionless gradient and the Laplacian operator are given by

$$\nabla = \left(\partial_x, \frac{1}{\epsilon}\partial_y, \right), \tag{1.33}$$

$$\Delta = \left(\partial_{xx} + \frac{1}{\epsilon^2}\partial_{yy}\right). \tag{1.34}$$

Applying the homogenization ansatz (1.32) and using the rescaled gradient operator (1.33) leads to

$$\begin{aligned} \nabla p^\epsilon &= \left(\partial_x, \frac{1}{\epsilon}\partial_y\right)\left(p^0 + \epsilon p^1 + \epsilon^2 p^2 + \mathcal{O}(\epsilon^3)\right), \\ &= \frac{1}{\epsilon}\left(0, \partial_y p^0\right) + \left(\partial_x p^0, \partial_y p^1\right) + \epsilon\left(\partial_x p^1, \partial_y p^2\right) + \mathcal{O}(\epsilon^2), \end{aligned} \tag{1.35}$$

and

$$\begin{aligned}
\nabla \cdot \mathbf{v}^\epsilon &= \left(\partial_x, \frac{1}{\epsilon}\partial_y\right) \cdot (v_1^\epsilon, v_2^\epsilon) = \partial_x v_1^\epsilon + \frac{1}{\epsilon}\partial_y v_2^\epsilon, \\
&= \left(\partial_x v_1^0 + \epsilon\partial_x v_1^1 + \mathcal{O}(\epsilon^2)\right) + \frac{1}{\epsilon}\left(\partial_y v_2^0 + \epsilon\partial_y v_2^1 + \mathcal{O}(\epsilon^2)\right), \\
&= \frac{1}{\epsilon}\partial_y v_2^0 + \left(\partial_x v_1^0 + \partial_y v_2^1\right) + \mathcal{O}(\epsilon).
\end{aligned} \tag{1.36}$$

Similarly, using the rescaled Laplacian operator (1.34) together with the homogenization ansatz (1.32) provides

$$\begin{aligned}
\Delta \mathbf{v}^\epsilon &= \left(\partial_{xx} + \frac{1}{\epsilon^2}\partial_{yy}\right)(v_1^\epsilon, v_2^\epsilon), \\
&= \left(\partial_{xx} + \frac{1}{\epsilon^2}\partial_{yy}\right)\left(\left(v_1^0 + \epsilon v_1^1 + \mathcal{O}(\epsilon^2)\right), \left(v_2^0 + \epsilon v_2^1 + \mathcal{O}(\epsilon^2)\right)\right), \\
&= \frac{1}{\epsilon^2}\left(\partial_{yy} v_1^0, \partial_{yy} v_2^0\right) + \frac{1}{\epsilon}\left(\partial_{yy} v_1^1, \partial_{yy} v_2^1\right) + \mathcal{O}(1).
\end{aligned} \tag{1.37}$$

Using the above three expansions in (1.29)-(1.31) and writing the x- and y-components of (1.29) separately gives

$$\begin{aligned}
\mu\partial_{yy} v_1^0 + \epsilon\mu\partial_{yy} v_1^1 &= \partial_x p^0 + \epsilon\partial_x p^1 + \mathcal{O}(\epsilon^2), && \text{in } \Omega_{\mathcal{P}}, \\
\mu\partial_{yy} v_2^0 &= \frac{1}{\epsilon}\partial_y p^0 + \partial_y p^1 + \mathcal{O}(\epsilon), && \text{in } \Omega_{\mathcal{P}}, \\
0 &= \frac{1}{\epsilon}\partial_y v_2^0 + \left(\partial_x v_1^0 + \partial_y v_2^1\right) + \mathcal{O}(\epsilon), && \text{in } \Omega_{\mathcal{P}}, \\
0 &= v_1^0 + v_1^1 + \mathcal{O}(\epsilon^2), && \text{on } \Gamma_{\mathcal{G}}^\epsilon, \\
0 &= v_2^0 + v_2^1 + \mathcal{O}(\epsilon^2), && \text{on } \Gamma_{\mathcal{G}}^\epsilon.
\end{aligned} \tag{1.38}$$

Note that v_2^0 does not play any role in the upscaled model since the ϵ^{-1} term of the third equation and ϵ^0 term of the y-component of the last equation of (1.38) give

$$\partial_y v_2^0 = 0, \text{ in } \Omega_{\mathcal{P}} \text{ and } v_2^0 = 0, \text{ on } \Gamma_{\mathcal{G}}^\epsilon,$$

which leads to

$$v_2^0 = 0, \text{in } \Omega_{\mathcal{P}}. \tag{1.39}$$

The ϵ^{-1} term of the second equation of (1.38) gives $\partial_y p^0 = 0$, implying that p^0 is y-independent, hence

$$p^0(x, y) = p^0(x). \tag{1.40}$$

To find the upscaled/averaged equation for the velocity, we first define the averaged quantity

$$\overline{v}(x) := \int_0^1 v_1^0(x, y)dy. \tag{1.41}$$

Subsequently we integrate the ϵ^0 term of the first equation of (1.38) three times with respect to y, which leads to

$$\overline{v}(x) = -\frac{1}{12}\frac{1}{\mu}\partial_x p^0, \text{ for } 0 \leq x \leq 1, \tag{1.42}$$

which is Darcy's law for single-phase flow. Note that there is usually a permeability factor proportional to the width of the fluid-layer cubed (see Chapter 2). Since the thin strip has unit width, this factor is here $\frac{1}{12}$.

Let δx be the width of a thin section of the pore space $\Omega_{\mathcal{P}}$ which is defined by $Y_{\mathcal{P}} = \{(x, y)|x_1 < x < x_1 + \delta x, 0 < y < 1\}$ with $0 < x_1 < 1$.

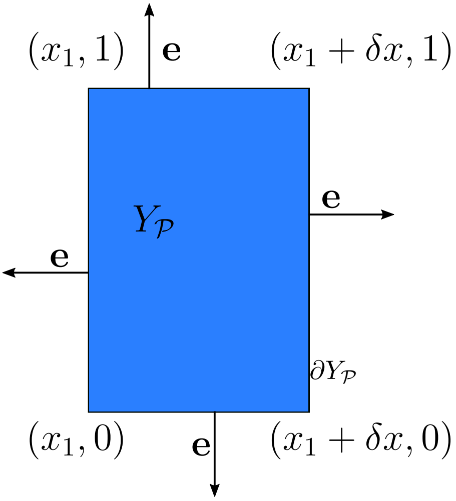

Figure 1.8: Thin section of the void space.

To show that the averaged velocity is divergence-free, we integrate the mass conservation (1.30) over $Y_{\mathcal{P}}$, which gives

$$\int_{Y_{\mathcal{P}}} \nabla \cdot \mathbf{v}^{\epsilon} dV = 0.$$

By applying Gauss's theorem to the integral above and divide it by δx, we obtain

$$\frac{1}{\delta x} \int_{\partial Y_{\mathcal{P}}} \mathbf{v}^{\epsilon} \cdot \mathbf{e} \, ds = 0,$$

where $\mathbf{e}$ is the outward unit normal vector. Since the boundary $\partial Y_{\mathcal{P}}$ consists of four parts; the right, left, up and down (see Figure 1.8), we can write

$$\begin{aligned}
0 =& \frac{1}{\delta x} \int_0^1 (v_1^{\epsilon}, v_2^{\epsilon}) \cdot (1,0) dy|_{x=x_1+\delta x} + \frac{1}{\delta x} \int_0^1 (v_1^{\epsilon}, v_2^{\epsilon}) \cdot (-1,0) dy|_{x=x_1} \\
&+ \frac{1}{\delta x} \int_{x_1}^{x_1+\delta x} (v_1^{\epsilon}, v_2^{\epsilon}) \cdot (0,1) dx|_{y=1} + \frac{1}{\delta x} \int_{x_1}^{x_1+\delta x} (v_1^{\epsilon}, v_2^{\epsilon}) \cdot (0,-1) \, dx|_{y=0}, \\
0 =& \frac{1}{\delta x} \int_0^1 v_1^{\epsilon} dy|_{x=x_1+\delta x} - \frac{1}{\delta x} \int_0^1 v_1^{\epsilon} dy|_{x=x_1} \\
&+ \frac{1}{\delta x} \int_{x_1}^{x_1+\delta x} v_2^{\epsilon} dx|_{y=1} - \frac{1}{\delta x} \int_{x_1}^{x_1+\delta x} v_2^{\epsilon} dx|_{y=0}.
\end{aligned}$$

Inserting the asymptotic expansion (1.32) in the above equation leads to

$$\begin{aligned}0 =& \frac{1}{\delta x}\int_0^1 \left(v_1^0 + \epsilon v_1^1 + \frac{1}{\delta x}\mathcal{O}(\epsilon^2)\right) dy|_{x=x_1+\delta x} - \frac{1}{\delta x}\int_0^1 \left(v_1^0 + \epsilon v_1^1 + \frac{1}{\delta x}\mathcal{O}(\epsilon^2)\right) dy|_{x=x_1}\\ &+ \frac{1}{\delta x}\int_{x_1}^{x_1+\delta x} \left(v_2^0 + \epsilon v_2^1 + \mathcal{O}(\epsilon^2)\right) dx|_{y=1} - \frac{1}{\delta x}\int_{x_1}^{x_1+\delta x} \left(v_2^0 + \epsilon v_2^1 + \mathcal{O}(\epsilon^2)\right) dx|_{y=0}.\end{aligned}$$

Collecting the lowest order terms and using (1.39), that is, $v_0^2 = 0$ at $y \in \{0, 1\}$, gives

$$0 = \frac{1}{\delta x}\int_0^1 v_1^0 dy|_{x=x_1+\delta x} - \frac{1}{\delta x}\int_0^1 v_1^0 dy|_{x=x_1}.$$

Using the definition of averaged velocity (1.41) in the above equation and letting $\delta x \to 0$, one obtains

$$\partial_x \overline{v}(x) = 0, \text{ for } 0 \leq x \leq 1, \tag{1.43}$$

which demonstrate that the Darcy-scale velocity is divergence-free.

Hence the Darcy-scale model equations for single-phase flow are given by (1.42) and (1.43).

1.3.3 Upscaling using homogenization

In this section, we upscale a single-phase flow model ((1.29)-(1.31)) but considering a complex, perforated domain. In doing so, we use the homogenization technique. We refer to [12, 52, 84] for an introduction to homogenization methods. This framework is further detailed in Chapter 3 for a two-phase flow model coupled with transport.

1.3.3.1 Geometric settings

Here the geometry is more complex than the thin strip. Let Ω be domain of the porous medium with outer boundary $\partial\Omega$. The domain Ω consists of a finite repetition of cells, $Y \in (0, l)^2$. Figure 1.9 shows the geometry of the periodic, perforated medium.

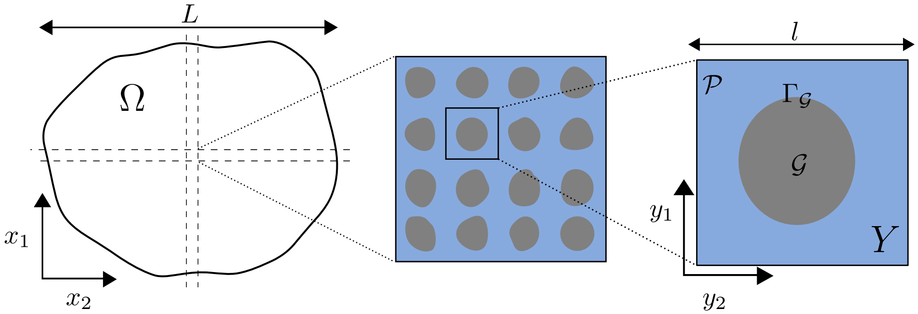

Figure 1.9: A schematic representation of perforated porous medium.

Let $\mathbf{x} = (x_1, x_2) \in (0, L)^2$ be the Darcy-scale variable for some positive number L, which contains only the large scale information. As in Section (1.3.2.1), we assume that $\epsilon = \frac{l}{L}$ is the scale separation parameter, where l is much smaller than L. Then the pore-scale variable $\mathbf{y} = (y_1, y_2) \in (0, l)^2$ is defined by $\mathbf{y} = \frac{\mathbf{x}}{\epsilon}$. Note that $\mathbf{x}$ and $\mathbf{y}$ play different roles in this model compared to the thin strip model. In the case of the thin-strip model, ϵ is defined by the ratio between the horizontal and vertical length scales, whereas for the periodical, perforated medium ϵ is defined by the ratio between the size of the local cell Y and the size of the Darcy-scale domain Ω.

We denote $\hat{\mathbf{x}} = \frac{\mathbf{x}}{L}$ and $\hat{\mathbf{y}} = \frac{\mathbf{y}}{l}$ as dimensionless variables. The consequence is that $\hat{\mathbf{x}} = (\hat{x}_1, \hat{x}_2) \in (0, 1)^2$ and $\hat{\mathbf{y}} = (\hat{y}_1, \hat{y}_2) \in (0, 1)^2$. By an abuse of notation, we suppress the hats from the non-dimensional variables from now on.

In the dimensionless settings, to define the pore-scale domain, we let each unit cell Y consist of a grain space $\mathcal{G}$, surrounded by the pore space $\mathcal{P}$ and the boundary between them $\Gamma_{\mathcal{G}}$, such that

$$Y = \mathcal{P} \cup \mathcal{G} \cup \Gamma_{\mathcal{G}}. \tag{1.44}$$

Then the Darcy-scale (porous medium) domain is mathematically described by

$$\Omega = \cup_{\mathbf{i} \in \mathcal{I}_\epsilon} \{\epsilon(\mathbf{i} + Y)\}, \tag{1.45}$$

where $\mathcal{I}_\epsilon$ is a set of multi indices. The pore space is defined by

$$\Omega_{\mathcal{P}}^{\epsilon} := \cup_{\mathbf{i} \in \mathcal{I}_\epsilon} \{\epsilon(\mathbf{i} + \mathcal{P})\}, \tag{1.46}$$

and the inner boundary between the grain and pore is

$$\Gamma^{\epsilon}_{\mathcal{G}} := \cup_{\mathbf{i}\in\mathcal{I}_{\epsilon}}\{\epsilon(\mathbf{i}+\Gamma_{\mathcal{G}})\}. \tag{1.47}$$

To derive the Darcy-scale model, we start with the dimensionless Stokes equations at the pore scale,

$$\epsilon^2\mu\Delta\mathbf{v}^{\epsilon} = \nabla p^{\epsilon}, \qquad \text{in } \Omega^{\epsilon}_{\mathcal{P}}, \tag{1.48}$$

$$\nabla\cdot\mathbf{v}^{\epsilon} = 0, \qquad \text{in } \Omega^{\epsilon}_{\mathcal{P}}, \tag{1.49}$$

$$\mathbf{v}^{\epsilon} = \mathbf{0}, \qquad \text{on } \Gamma^{\epsilon}_{\mathcal{G}}. \tag{1.50}$$

1.3.3.2 The Darcy-scale model equations

We start here by writing the two-scale expansion for p^{ϵ} and $\mathbf{v}^{\epsilon}$ as

$$\begin{aligned} p^{\epsilon}(\mathbf{x}) &= p^0(\mathbf{x},\frac{\mathbf{x}}{\epsilon}) + \epsilon p^1(\mathbf{x},\frac{\mathbf{x}}{\epsilon}) + \mathcal{O}(\epsilon^2),\\ \mathbf{v}^{\epsilon}(\mathbf{x}) &= \mathbf{v}^0(\mathbf{x},\frac{\mathbf{x}}{\epsilon}) + \epsilon\mathbf{v}^1(\mathbf{x},\frac{\mathbf{x}}{\epsilon}) + \mathcal{O}(\epsilon^2), \end{aligned} \tag{1.51}$$

where $p^{\mathtt{j}}, \mathbf{v}^{\mathtt{j}}$ are Y-periodic functions. In other words, for $\mathtt{j} = 0,1,2,\cdots$ and $\mathbf{e}^{\mathtt{i}}, \mathtt{i} = 1,2$ being the unit vectors in the $x_{\mathtt{i}}$-directions, one has $p^{\mathtt{j}}(\mathbf{x},\mathbf{y}) = p^{\mathtt{j}}(\mathbf{x},\mathbf{y}+\mathbf{e}^{\mathtt{i}}), \mathbf{v}^{\mathtt{j}}(\mathbf{x},\mathbf{y}) = \mathbf{v}^{\mathtt{j}}(\mathbf{x},\mathbf{y}+\mathbf{e}^{\mathtt{i}})$. Note that the variable $\mathbf{x}$ is doubled here. We consider the slow variable $\mathbf{x}$, accounting for changes at the Darcy scale, and $\mathbf{y} = \frac{\mathbf{x}}{\epsilon}$, reflecting rapid oscillations at the pore scale (the fast variable). The gradient and Laplacian operators need to be rewritten as

$$\nabla = \nabla_{\mathbf{x}} + \frac{1}{\epsilon}\nabla_{\mathbf{y}}, \quad \Delta = \Delta_{\mathbf{x}} + \frac{1}{\epsilon}\left(\nabla_{\mathbf{x}}\cdot\nabla_{\mathbf{y}} + \nabla_{\mathbf{y}}\cdot\nabla_{\mathbf{x}}\right) + \frac{1}{\epsilon^2}\Delta_{\mathbf{y}}. \tag{1.52}$$

Using these expansions in (1.48)-(1.50) implies

$$
\begin{aligned}
&\mu\Delta_{\mathbf{y}}\mathbf{v}^0 + \epsilon\mu\left[\left(\nabla_{\mathbf{x}}\cdot\nabla_{\mathbf{y}} + \nabla_{\mathbf{y}}\cdot\nabla_{\mathbf{x}}\right)\mathbf{v}^0 + \Delta_{\mathbf{y}}\mathbf{v}^1\right] \\
&\quad = \frac{1}{\epsilon}\nabla_{\mathbf{y}}p^0 + \left(\nabla_{\mathbf{x}}p^0 + \nabla_{\mathbf{y}}p^1\right) + \epsilon\left(\nabla_{\mathbf{x}}p^1 + \nabla_{\mathbf{y}}p^2\right) + \mathcal{O}(\epsilon^2), && \text{in } \Omega^\epsilon_{\mathcal{P}}, \\
&0 = \frac{1}{\epsilon}\nabla_{\mathbf{y}}\cdot\mathbf{v}^0 + \left(\nabla_{\mathbf{x}}\cdot\mathbf{v}^0 + \nabla_{\mathbf{y}}\cdot\mathbf{v}^1\right) + \epsilon\left(\nabla_{\mathbf{x}}\cdot\mathbf{v}^1 + \nabla_{\mathbf{y}}\cdot\mathbf{v}^2\right) + \mathcal{O}(\epsilon^2), && \text{in } \Omega^\epsilon_{\mathcal{P}}, \\
&\mathbf{0} = \mathbf{v}^0 + \epsilon\mathbf{v}^1 + \mathcal{O}(\epsilon^2), && \text{on } \Gamma^\epsilon_{\mathcal{G}}.
\end{aligned}
\tag{1.53}
$$

We equate the terms of the same order of magnitude. The ϵ^{-1} term in the first equation gives

$$\nabla_{\mathbf{y}}p^0 = 0, \text{ for } \mathbf{y}\in\mathcal{P}, \tag{1.54}$$

implying that p^0 is $\mathbf{y}$-independent, hence $p^0(\mathbf{x},\mathbf{y}) = p^0(\mathbf{x})$.

The ϵ^0 terms in the first and the last equation in (1.53) and the ϵ^{-1} term in the middle equation lead to

$$
\begin{cases}
\mu\Delta_{\mathbf{y}}\mathbf{v}^0 = \left(\nabla_{\mathbf{x}}p^0 + \nabla_{\mathbf{y}}p^1\right), & \text{in } \mathcal{P}, \\
\nabla_{\mathbf{y}}\cdot\mathbf{v}^0 = 0, & \text{in } \mathcal{P}, \\
\mathbf{v}^0 = \mathbf{0}, & \text{on } \Gamma_{\mathcal{G}}, \\
p^1 \text{ and } \mathbf{v}^0 \text{ are } Y\text{-periodic.}
\end{cases}
\tag{1.55}
$$

We have

$$\nabla_{\mathbf{x}}p^0(\mathbf{x}) = \sum_{\mathrm{j}=1}^{2}\mathbf{e}_{\mathrm{j}}\partial_{x_{\mathrm{j}}}p^0(\mathbf{x}). \tag{1.56}$$

By considering the linearity of the problem (1.55), we assume that p^1 and $\mathbf{v}^0$ can be written as a linear combination of some functions Π_{j} and χ_{j} with $\partial_{x_{\mathrm{j}}}p^0(\mathbf{x})$ as weights.

Namely,

$$\mathbf{v}^0(\mathbf{x},\mathbf{y}) = -\frac{1}{\mu}\sum_{\mathrm{j}=1}^{2}\chi_{\mathrm{j}}(\mathbf{x},\mathbf{y})\partial_{x_{\mathrm{j}}}p^0(\mathbf{x}), \tag{1.57}$$

$$p^1(\mathbf{x},\mathbf{y}) = \sum_{\mathrm{j}=1}^{2}\Pi_{\mathrm{j}}(\mathbf{x},\mathbf{y})\partial_{x_{\mathrm{j}}}p^0(\mathbf{x}). \tag{1.58}$$

Inserting these expressions into (1.55), we can construct the so-called cell problems ($\mathrm{j} = 1,2$)

$$\begin{cases} -\Delta_{\mathbf{y}}\chi_{\mathrm{j}}(\mathbf{y}) = \mathbf{e}_{\mathrm{j}} + \nabla_{\mathbf{y}}\Pi_{\mathrm{j}}(\mathbf{y}), & \text{in } \mathcal{P}, \\ \nabla_{\mathbf{y}}\cdot\chi_{\mathrm{j}}(\mathbf{y}) = 0, & \text{in } \mathcal{P}, \\ \chi_{\mathrm{j}}(\mathbf{y}) = \mathbf{0}, & \text{on } \Gamma_{\mathcal{G}}, \\ \Pi_{\mathrm{j}}, \chi_{\mathrm{j}} \text{ are } Y\text{-periodic }. \end{cases} \tag{1.59}$$

Since $|Y| = 1$, we define the average velocity as

$$\overline{\mathbf{v}}(\mathbf{x}) = \int_{\mathcal{P}}\mathbf{v}^0(\mathbf{x},\mathbf{y})dy, \text{ for all } \mathbf{x}\in\Omega. \tag{1.60}$$

The ϵ^0-order terms give

$$\nabla_{\mathbf{x}}\cdot\mathbf{v}_0(\mathbf{x},\mathbf{y}) + \nabla_{\mathbf{y}}\cdot\mathbf{v}_1(\mathbf{x},\mathbf{y}) = 0, \tag{1.61}$$

for all $\mathbf{y}\in\mathcal{P}$. Integrating the above with respect to $\mathbf{y}$, applying the Gauss theorem, and using the periodicity of $\mathbf{v}_1(\mathbf{x},\mathbf{y})$ and the boundary condition $\mathbf{v}_1(\mathbf{x},\mathbf{y}) = 0$ on $\Gamma_{\mathcal{G}}$, one gets

$$\nabla_{\mathbf{x}}\cdot\bar{\mathbf{v}}(\mathbf{x}) = 0, \tag{1.62}$$

for all $\mathbf{x}\in\Omega$.

Integrating (1.57) with respect to $\mathbf{y}$ over $\mathcal{P}$ and using the average velocity (1.60), for all $\mathbf{x}\in\Omega$, we obtain Darcy's law

$$\overline{\mathbf{v}} = -\frac{\mathcal{K}}{\mu}\nabla_{\mathbf{x}}p^0, \text{ in } \Omega, \tag{1.63}$$

where the permeability tensor $\mathcal{K}$ has the components

$$\mathcal{K}_{\mathtt{ij}} = \int_{\mathcal{P}} \chi_{\mathtt{j}}^{\mathtt{i}}(\mathbf{y})dy, \tag{1.64}$$

for $\mathtt{i}, \mathtt{j} = \{1, 2\}$. The elements of the effective matrix $\mathcal{K}(\mathbf{x})$ are obtained using the solutions of the cell problems (1.59). One can prove that $\mathcal{K}$ is symmetric and positive definite.

1.4 A brief description of the numerical schemes

We discuss briefly the numerical schemes used in this thesis to approximate the solution of the Darcy-scale models. We observe that these models are systems of coupled, non-linear partial differential equations and ordinary differential equations.

Since the upscaled models that will be derived in Chapter 2 are one-dimensional in space, we use finite differences for the spatial discretization [104]. The upscaled model that will be derived in Chapter 3 is a two-dimensional, two-scale, coupled non-linear system of partial differential equations, which we discretize in space by the mixed finite element method (MFEM) (see [10, 25, 32]). For the time discretization in Chapters 2 and 3, we consider both explicit and implicit schemes. To handle the non-linearities in the resulting coupled system of equations after discretization, we use linearization schemes, namely Newton's method (see [23, 43, 92, 139]) and the L-scheme (see [107, 136]) in Chapters 2 and 3.

1.4.1 Spatial discretization

In the following, we present the main concepts of the finite difference and mixed finite element methods. To introduce the finite difference method, we consider a simple partial differential equation

$$\frac{\partial^2 u(x)}{\partial x^2} = f, \text{ for } 0 \leq x \leq 1, \tag{1.65}$$

where f is given. We consider homogeneous Dirichlet boundary conditions, $u(0) = u(1) = 0$. For some given $N \in \mathbb{N}$, we choose $\Delta x = \frac{1}{N}$ as the fixed spatial-step size, and let

$x_j = j\Delta x$ be the mesh points and $j \in \{0, \dots, N\}$. The unknowns u_j approximate

$$u(x_j), j \in \{0, \dots, N\}. \tag{1.66}$$

Using a central finite difference approximation in (1.65) and letting $f_j = f(x_j)$, one obtains

$$\frac{u_{j-1} - 2\, u_j + u_{j+1}}{\Delta x^2} = f_j, \text{ for } j = 1, \dots, N-1, \tag{1.67}$$

which is an algebraic system of linear equations in the unknowns $u_j, j = 1, \dots, N-1$. Clearly $u_0 = u_N = 0$ due to the boundary conditions. With this one needs to solve the system

$$A\, U = F \tag{1.68}$$

where $F = (f_1, \dots, f_{N-1})^T \in \mathbb{R}^{(N-1)}$, and $A \in \mathbb{R}^{(N-1)\times(N-1)}$ is a matrix with entries $a_{jj} = -\frac{2}{\Delta x^2}, a_{j,j-1} = a_{j-1,j} = \frac{1}{\Delta x^2}$, and the unknown vector $U = (u_1, \dots, u_{N-1})^T \in \mathbb{R}^{(N-1)}$.

The mixed finite element method (MFEM) is a commonly used mass-conserving discretization technique (see [32]). Given a two-dimensional bounded domain $\Omega \subset \mathbb{R}^2$ with boundary $\partial\Omega$, we consider the elliptic problem

$$\begin{aligned} -\nabla \cdot (\mathcal{K}\nabla u) &= f, \text{ in } \Omega, \\ u &= 0, \text{ on } \partial\Omega, \end{aligned} \tag{1.69}$$

where u is the unknown function, f is a given function and $\mathcal{K}$ is a positive definite matrix. In many flow problems, the variable of interest is not only u but also the flux $-\mathcal{K}\nabla u$. Hence, we consider a second, vector-valued unknown,

$$\mathbf{v} = -\mathcal{K}\nabla u. \tag{1.70}$$

Then using (1.70), problem (1.69) is decomposed into the first-order system of equations

$$\begin{aligned} \mathbf{v} &= -\mathcal{K}\nabla u, && \text{in } \Omega, \\ \nabla\cdot\mathbf{v} &= f, && \text{in } \Omega, \\ u &= 0, && \text{on } \partial\Omega, \end{aligned} \tag{1.71}$$

which is the so-called mixed formulation of (1.69).

Before presenting the discretization, we introduce the functional spaces. Let $L^2(\Omega)$ be the Hilbert space of square-integrable real-valued functions with the usual norm. With this, we consider the space

$$H(\mathrm{div},\Omega) = \{\mathbf{q} \in [L^2(\Omega)]^2 : \nabla\cdot\mathbf{q} \in L^2(\Omega)\}. \tag{1.72}$$

Multiplying the first two equations of (1.71) by the test functions $\mathbf{q} \in H(\mathrm{div},\Omega)$ and $w \in L^2(\Omega)$ respectively, integrating over the domain Ω and using integration by parts, we obtain the weak mixed formulation of (1.71).

Problem WM: Find $u \in L^2(\Omega)$ and $\mathbf{v} \in H(\mathrm{div},\Omega)$ satisfying

$$\begin{aligned} \int_\Omega \mathcal{K}^{-1}(\mathbf{v}\cdot\mathbf{q})\,d\mathbf{x} - \int_\Omega u\nabla\cdot\mathbf{q}\,d\mathbf{x} &= 0, && \text{for all } \mathbf{q} \in H(\mathrm{div},\Omega), \\ \int_\Omega w\nabla\cdot\mathbf{v}\,d\mathbf{x} &= \int_\Omega fw\,d\mathbf{x}, && \text{for all } w \in L^2(\Omega). \end{aligned}$$

Let T_h be a triangular partition of Ω with elements T such that $\Omega = \bigcup_{T\in T_h} T$, where no vertex of any triangle lies in the interior of an edge of another triangle. It is an admissible triangulation (see [29, 30]).

We proceed now with the spatial discretization of Problem WM. We approximate the solutions $\mathbf{v}$ and u of (1.71) by functions in finite-dimensional subspaces. To this aim, we use the lowest-order Raviart-Thomas space $Q_h := \mathcal{RT}_0(T_h)$ for approximating the vectorial unknown $\mathbf{v}$ (see [146]) and for the scalar unknown we use the discrete subspace of piecewise constant functions $W_h := \mathbb{P}_0(T_h)$,

$$\begin{aligned} Q_h &= \{\mathbf{q}_h \in H(\mathrm{div},\Omega) : \mathbf{q}_h|_T = \mathbf{a} + b\mathbf{x} \text{ for all } T \in T_h, \mathbf{a} \in \mathbb{R}^2, b \in \mathbb{R}\}, \\ W_h &= \{w_h \in L^2(\Omega) : w_h \text{ is constant on each element } T \in T_h\}. \end{aligned} \tag{1.73}$$

Note that here we choose the most popular Raviart-Thomas space but one can also use Brezzi-Douglas-Marini or Brezzi-Douglas-Fortin-Marini spaces, we refer to [25, 32] for more details. Now we write the discrete weak mixed formulation of (1.71).

Problem DM: Find $u_h \in W_h$ and $\mathbf{v}_h \in Q_h$ satisfying

$$\begin{aligned} \int_{T_h} \mathcal{K}^{-1}(\mathbf{v}_h \cdot \mathbf{q}_h)\, d\mathbf{x} - \int_{T_h} u_h \nabla \cdot \mathbf{q}_h\, d\mathbf{x} &= 0, && \text{for all } \mathbf{q}_h \in Q_h, \\ \int_{T_h} w_h \nabla \cdot \mathbf{v}_h\, d\mathbf{x} &= \int_{T_h} f w_h\, d\mathbf{x}, && \text{for all } w_h \in W_h. \end{aligned}$$

We denote $\mathtt{nEdge}_h$ and $\mathtt{nElem}_h$ as the total number of edges and elements in the triangulation T_h. Let $\mathbf{q}_{h,1}, \ldots, \mathbf{q}_{h,\mathtt{nEdge}_h}$ and $w_{h,1}, \ldots, w_{h,\mathtt{nElem}_h}$ form the basis functions of the finite dimensional subspaces Q_h and W_h, respectively. Now, each unknown and test function of Problem DM can be written as linear combination of the basis functions such that

$$\mathbf{v}_h = \sum_{\mathtt{k}=1}^{\mathtt{nEdge}_h} [\mathbf{v}_h]_{\mathtt{k}} \mathbf{q}_{h,\mathtt{k}} \qquad \text{and} \qquad u_h = \sum_{\mathtt{k}=1}^{\mathtt{nElem}_h} [u_h]_{\mathtt{k}} w_{h,\mathtt{k}}.$$

The degrees of freedom $[\mathbf{v}_h]_{\mathtt{k}}$ are defined as fluxes across element edges and $[u_h]_{\mathtt{k}}$ are defined as element values. Denote A, B and C the matrices with elements

$$\begin{aligned} A_{\mathtt{k},\ell} &:= \int_{T_h} \mathcal{K}^{-1}(\mathbf{q}_{h,\mathtt{k}} \cdot \mathbf{q}_{h,\ell})\, d\mathbf{x}, \\ B_{\mathtt{k},\ell} &:= \int_{T_h} w_{h,\mathtt{k}} \nabla \cdot \mathbf{q}_{h,\ell}\, d\mathbf{x}, \\ C_\ell &:= \int_{T_h} f w_{h,\ell}\, d\mathbf{x}. \end{aligned} \tag{1.74}$$

The discretization of Problem DM then yields to a linear system of the form

$$\begin{bmatrix} A & -(B)^t \\ B & 0 \end{bmatrix} \begin{bmatrix} [\mathbf{v}_h] \\ [u_h] \end{bmatrix} = \begin{bmatrix} 0 \\ C \end{bmatrix}.$$

1.4.2 Time discretization

Time discretization is discussed for the differential equation

$$\frac{du}{dt} = f(u,t), \text{ for } t > 0, \tag{1.75}$$

where $f : \mathbb{R}^{d+1} \to \mathbb{R}^d$ is a Lipschitz continuous function and $u : \mathbb{R} \to \mathbb{R}^d$. In practice, f comes from spatial discretization of a partial differential equations and u is the space discrete solution vector. Let $u(0) = u_0$ be the initial condition. For some given $N_t \in \mathbb{N}$, we choose $\Delta t = \frac{T}{N_t}$ as the fixed time-step size. We denote $t^n = n\Delta t$ the mesh points in time. Then, replacing the first-order derivative using forward finite discretization in time, (1.75) becomes

$$\frac{u(t+\Delta t) - u(t)}{\Delta t} \approx f(u,t). \tag{1.76}$$

This suggest an explicit method to approximate $u(t)$. For $n \in \mathbb{N}$, let u^n be the approximation of the exact solution $u(t^n)$ and let $f^n = f(u^n, t^n)$. Then for all $n > 0$, one finds u^n as,

$$u^n = u^{n-1} + f^{n-1}\Delta t. \tag{1.77}$$

This approach, known as the forward Euler method, is fast, but it has only conditional stability [45]. More precisely, if the time-step size is not small enough, the solution will be oscillatory or diverge [7, 8]. However, the main advantage of the forward Euler method is the possibility to advance the system at each time step, without the need to solve a system of equations where all the degrees of freedom are involved. An alternative to the forward Euler method is the backward Euler method. Then we can approximate u^n as

$$u^n = u^{n-1} + f^n\Delta t, \text{ for } n > 0. \tag{1.78}$$

Compared to forward Euler method, this method allows stable time steps under less strict conditions on the time-step size Δt (see e.g., in [8]). However, since $f^n = f(u^n, t^n)$, at each time step, one needs to solve a nonlinear system of equations, which makes the method costly and difficult to parallelize. In general, no direct methods are available for this system, so one needs to consider iterative ones. For details on time discretization methods, we refer to [7, 8, 45].

1.4.3 Iterative solvers

As seen before, when using the backward Euler method, one needs to solve at each time step, a nonlinear algebraic system of equations. More precisely, for a fixed n and assuming u^{n-1} known, (1.78) becomes

$$G^n(u^n) = 0, \tag{1.79}$$

where $G^n : \mathbb{R}^d \to \mathbb{R}^d$ is defined as $G^n(u) = u - \Delta t f^n(t^n, u) - u^{n-1}$ for $u^n \in \mathbb{R}^d$. For $i \geq 0$ and given an initial guess u_0^n, the Newton method represents the following iterations

$$u_i^n = u_{i-1}^n - \nabla G^n(u_{i-1}^n)^{-1}\, G^n(u_{i-1}^n), \text{ for } i > 0, \tag{1.80}$$

where ∇G^n is the Jacobian of G^n. Newton's method converges quadratically but only if the initial guess u_0^n is close enough to the solution. With u_0^{n-1} as a natural initial guess, this induces severe restrictions on Δt. Moreover, one needs to compute ∇G at every iteration, which is very expensive. We have used Newton's method in Chapter 2, where the non-linear systems are smaller, since the models are one-dimensional.

An alternative to the Newton's method is the L-scheme. Given u_0^n, for $i > 0$, the iterations are

$$u_i^n = u_{i-1}^n - \mathcal{L}^{-1} G^n(u_{i-1}^n), \tag{1.81}$$

where $\mathcal{L}$ is a constant, diagonal matrix. The L-scheme is a simple, fixed-point iteration method. It only converges linearly for certain $\mathcal{L}$, and the convergence is then unconditional, for any initial guess but this scheme is robust with respect to the mesh size. Moreover, one does not have to compute the Jacobian, and therefore the computations are faster than for the Newton scheme. In Chapter 3, we use the L-scheme as the models are two-dimensional and the systems are larger. In the context of two-phase flow and transport problems, the robustness and convergence of the L-scheme are analyzed in [88, 142, 143].

1.5 Objectives

The aim of this thesis is to derive upscaled models for two-phase/unsaturated flow and surfactant transport in porous media taking into account the evolving fluid-fluid interface at the pore scale. The main objectives of this research are:

1. Upscaling of pore-scale models for a sharp-interface model problem for two-phase/unsaturated flow and surfactant transport in a simple domain with evolving fluid-fluid interfaces at the pore scale.

2. Upscaling of pore-scale models for a diffuse-interface model problem for two-phase flow and surfactant transport in a complex domain with evolving fluid-fluid interfaces at the pore scale.

To achieve this goal we start with the pore-scale modelling of two-phase/unsaturated flow and surfactant transport in porous media. We will use a thin strip and a periodically perforated domain (Chapters 2 and 3) to represent the pore-scale geometry of the porous medium. In particular, we account for the moving interfaces at the pore scale, and for the presence of variable surface tension effects due to soluble surfactant. This gives rise to a free-boundary problem at the pore-scale. To handle the free-boundary, we use a sharp-interface approach for the simple geometry of a thin-strip in Chapter 2. For a more general domain in Chapter 3 we use a diffuse-interface approach that allows us to work in fixed domains.

We apply formal upscaling methods to derive Darcy-scale models from the pore-scale ones. In particular, we apply transversal averaging and periodic homogenization as upscaling techniques. The resulting effective (upscaled) models are given by non-standard Darcy-type equations including physical effects due to evolving fluid-fluid interface. Whereas traditionally two-phase flow models at the Darcy scale needs additional constitutive relationships (e.g., $p_c - S$- and $k_r - S$-relationship) to close the system. In Chapter 2, we obtain models where the phase pressure difference depends on the Laplacian of the saturation. In Chapter 3, we derive a two-scale model where phase-field evolution appears through the pore-scale cell problems. The effective parameters appearing in the two-scale model are obtained by solving the derived pore-scale cell problems. Additionally, we show that the variations in the surface tension cannot be neglected since they have a significant impact on Darcy-scale properties like the effective flow velocity and phase pressures.

The upscaled models are validated numerically. Additionally, in Chapter 3, we propose a numerical scheme to solve the complete two-scale model.

1.6 Outline of the thesis

The thesis is structured in four main chapters. In the introductory chapter, we have given the mathematical and upscaling background of our work. The scientific part of the thesis is described in Chapter 2 and Chapter 3 and is summarized as follows:

Chapter 2. Thin strip homogenization of two-phase flow problems. We consider a problem which includes a pore-scale model for two-phase flow in a two-dimensional (2D) thin strip. The pore-scale model describes flow of two immiscible and incompressible fluid phases (e.g., wetting and non-wetting) in the thin strip. Additionally, a solute is transported in the wetting fluid. The wetting fluid is attached to the pore walls. At the pore scale, the flow is modelled by the Navies-Stokes equation, and a convection-diffusion equation describes the solute transport. The evolving fluid-fluid interface is modelled as a freely moving sharp interface. It depends on the flow of both fluids and on the surface tension. Moreover, the surface tension may depend on the concentration of the solute. We compute simple transversal averages over the thin strip and derive different upscaled models in various pore-scale regimes depending on the dimensionless parameters. The upscaled models at the Darcy scale describe the averaged behaviour of the system and include pore-scale information through effective parameters. Numerical solutions of the upscaled equations (1D) are computed using a finite difference scheme. We use the commercial software COMSOL (see [1]) to compute the direct numerical simulation of the pore-scale model and then we average transversally the 2D solutions to compare the results with the upscaled solutions. Numerical examples show that the upscaled models are a good approximation of the transversal average of the solution to the pore-scale models, as the ratio of the width and the length of the pore approaches zero.

Chapter 3. Periodic homogenization of two-phase flow problems. Here we start with a pore-scale model for two-phase flow accounting for variable surface tension effects. A periodically perforated medium is considered as a representation of the porous medium. A surfactant is dissolved in one of the fluid phases, and its concentration at the interface separating these two fluids gives rise to changes in the surface tension. At the scale of pores, we assume that the flow is governed by the Navier-Stokes equations, while for the phase separation, a Cahn-Hilliard phase-field model is adopted. Using formal homogenization, we derive a two-scale phase-field model describing the averaged behaviour of the system at the Darcy scale. The effective quantities are found through the corresponding local (cell) problems at the pore scale. For this two-scale phase-field model, we formulate a numerical scheme and present numerical results highlighting the influence of the solute-dependent surface tension.

In Chapter 4 we include a detailed discussion of the originality, impact and open questions related with this thesis.

Chapter 2

Thin strip homogenization of two-phase flow problems

This chapter is based on the following publication [162]:

> ”S. Sharmin, C. Bringedal, I.S. Pop, On upscaling pore-scale models for two-phase flow with evolving interfaces, Advances in Water Resources, 142 (2020), p.103646, https://doi.org/10.1016/j.advwatres.2020.103646.”

2.1 Introduction

Here the starting point is pore-scale models for two-phase and unsaturated flow through a thin strip. The fluids are assumed incompressible and immiscible. For each fluid phase, the flow is governed by the Navier-Stokes model, defined in the corresponding sub-domain, and with fluid-specific parameters. The models also take into account the possibility that one fluid is transporting a soluble surfactant or solute, which has an impact on the surface tension coefficient. The fluid-fluid interface moves depending on the (unknown) fluid velocities, and, if applicable, on the concentration of the solute at this interface. As discussed in Section 1.1.1.1, this gives rise to a free-boundary problem at the pore scale. Hence, the model equations are defined in time-dependent a-priori unknown pore-scale sub-domains corresponding to the space filled by each of the two fluids. One significant challenge can be identified in this context: the free boundary at the pore scale.

To deal with the free boundary, we consider a sharp-interface approach, in which jump conditions ensuring conservation of the involved quantities are used at the evolving fluid-fluid interface, as well as kinematic conditions to model its evolution. For simplicity, we considered here a thin strip (see Figure 2.1) as a representative of the local pore geometry. Although this is a very simple geometry, upscaling thin-strip models in other contexts (e.g. biofilm growth [176] and mineral precipitation [179]) has shown that the upscaled models have the same structure as commonly accepted Darcy-scale models in general porous media (see [178] and [158]). The advantage of using a single pore is that analytical expressions for the upscaled quantities are obtained. Inside the thin strip we assume that the two fluids have a layered structure. Hence, the location of the interface separating the two fluid phases can also uniquely describe the thickness of the wetting phase and hence the saturation. Such a fluid distribution is the same as the core-annular flow in [133] and the thin-film flow in [118]. In [133], upscaled models for core-annular flow and other fluid distributions are derived, but under steady-state conditions. Here we explicitly account for the evolving fluid-fluid interface by treating the width of the wetting phase as a variable. For more complicated situations, one can use e.g. a level-set approach [128] to track the location of the interface. Alternatively, a diffuse-interface approach can be considered, using e.g. the phase-field model in [2]. For more realistic situations, in Chapter 3 we assume periodically perforated domain and use a phase-field approach to avoid discontinuities and working in time-dependent domains.

In any of these approaches, the pore-scale models can be used for deriving the upscaled, Darcy-scale counterparts, which are more suited for numerical simulations. We recall that in practical applications, the main interest is in the system's behavior at the Darcy scale, not necessarily in the detailed, pore-scale behavior. Therefore, we use formal upscaling methods for deriving Darcy-scale models, approximating the averaged, Darcy-scale behavior of the system. For the simplified domain considered here, we apply asymptotic expansion techniques and transversal averaging to derive the upscaled models.

This chapter is build on [115, 118], where mathematically rigorous upscaling results are obtained for two-phase flow in a single pore. Compared to [115,118], here we consider different regimes with respect to the capillary number, and also include solute effects in the surface tension dependency. We also mention that, although not considering the flow in a porous medium, in [31] a similar approach is used for deriving the shallow-water equations.

This chapter is organized as follows. In Section 2.2 the mathematical models at the pore scale are introduced, based on Section 1.2.1. With ϵ being a small parameter representing the ratio of the pore width and length, in Section 2.3 the pore-scale models are non-dimensionalized and their dependence on ϵ is formulated. In Section 2.4 asymptotic expansion methods are applied to the pore-scale models and for various scaling regimes and the corresponding upscaled models are derived. In this sense, the cases in which the Marangoni effects do play a role at the Darcy scale are evidenced. Also, cases where the two upscaled fluid pressures are equal, or the capillary pressure depends on the saturation in a non-standard way are evidenced, resembling the models in [54, 55, 115, 118]. The results are summarized and discussed more closely in Section 2.5. Section 2.6 provides some numerical examples that confirm the validity of the approach. Specifically, the numerical solutions to the original pore-scale models are computed for different situations, and then their transversal averages are compared to the solutions of the upscaled models. These results support that, as ϵ approaches zero, the upscaled models are describing well the averaged behaviour of the considered pore-scale models. Finally, in Section 2.7 the different upscaled models are compared, highlighting the upscaled behaviour of the considered physical phenomena.

2.2 Mathematical model

A pore-scale model is considered for two-phase or unsaturated flow through a porous medium. For simplicity, we consider a single pore only. The pore is long and thin, specifically a thin strip. The pore is filled by two incompressible and immiscible fluids, having constant densities and viscosities. From the two fluids, one is wetting and the other non-wetting. The wetting phase is attached to the pore wall. The wetting layer has a thickness that changes with time and varies with the location of the wall. The two fluids are separated by a sharp interface with zero thickness which changes with time. The movement is not known a-priori, hence the fluid-fluid interface is a moving boundary.

Its movement is determined by the surface tension and by the flow of the two fluids. The pore-scale models also consider the possibility of one fluid transporting a (soluble) surfactant species. The surface tension is a function of the solute concentration, resulting in a tangential stress at the moving interface, the so called Marangoni stress.

2.2.1 Geometric settings

We start by describing the geometry of the two-phase thin-strip model. The width and length of the thin strip are respectively $2l$ and L with $L \gg l$. For simplicity, we assume a symmetric case with respect to (w.r.t.) the x-axis. The lower half of the strip is shown in 2.1.

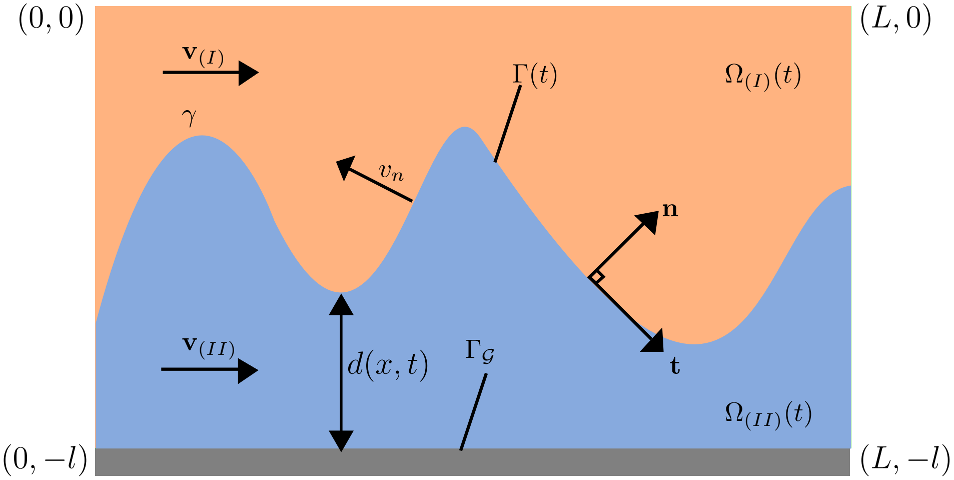

Figure 2.1: Schematic representation of the lower half of a single pore.

Let $t > 0$ be the time variable. The wetting fluid occupies a layer along the (lower) pore wall, having thickness d. Note that d depends on the x-coordinate and the time, $d = d(x,t)$, and that is not known a-priori. We assume that $0 \leq d(x,t) \leq l$. The pore space $\Omega_{\mathcal{P}}$ consists of two domains. The domains occupied by the non-wetting fluid (fluid-I) and the wetting (fluid-II) fluid are denoted by

$$\Omega_{(I)}(t) := \{(x,y) \in \mathbb{R}^2 | 0 < x < L, -l + d(x,t) < y < 0\},$$

$$\Omega_{(II)}(t) := \{(x,y) \in \mathbb{R}^2 | 0 < x < L, -l < y < -l + d(x,t)\}.$$

Observe that $\overline{\Omega}_{\mathcal{P}} = \overline{\Omega}_{(II)}(t) \cup \overline{\Omega}_{(I)}(t)$ is a fixed domain. The fluid-fluid interface and the fluid-solid interface, are respectively

$$\begin{aligned} \Gamma\left(t\right) &:= \{(x, y) \in \mathbb{R}^2 | 0 < x < L, y = -l + d\left(x, t\right)\}, \\ \Gamma_{\mathcal{G}} &:= \{(x, y) \in \mathbb{R}^2 | 0 < x < L, y = -l\}. \end{aligned}$$

Since $y = d(x, t)$ gives the location of the fluid-fluid interface $\Gamma(t)$, the unit normal vector at $\Gamma(t)$ pointing into fluid-I and the unit tangent vector are

$$\mathbf{n} := (-\partial_x d, 1)^T / \sqrt{1 + (\partial_x d)^2}, \text{ and } \mathbf{t} := (1, \partial_x d)^T / \sqrt{1 + (\partial_x d)^2}.$$

Given a point $(x, -l + d(x, t))$ on $\Gamma(t)$, its normal velocity is

$$v_n := \partial_t d / \sqrt{1 + (\partial_x d)^2}. \tag{2.1}$$

The curvature of $\Gamma(t)$ is given by

$$\nabla \cdot \mathbf{n} := -\partial_x \left(\frac{\partial_x d}{\sqrt{1 + (\partial_x d)^2}} \right).$$

Sections 2.2.2-2.2.4 is based on the discussions of Section 1.2.1. In the Sections 2.2.2-2.2.4, we start with formulating the relevant models at the pore scale and later we present the corresponding non-dimensional models in Sections 2.3.1-2.3.3.

2.2.2 Pore-scale model for the two-phase flow with solute-dependent surface tension

In this section, we consider pore-scale model for the two-phase flow with solute-dependent surface tension. Recall that the sub-domain occupied by fluid α is time dependent, $\Omega_{(\alpha)}(t)$, and that the freely moving fluid-fluid interface is denoted $\Gamma(t)$, and considering the discussion in Sections 1.2.1.2 and 1.2.1.4, one has

$$\rho_{(\alpha)}\partial_t \mathbf{v}_{(\alpha)} + \rho_{(\alpha)}\left(\mathbf{v}_{(\alpha)}\cdot\nabla\right)\mathbf{v}_{(\alpha)} = -\nabla p_{(\alpha)} + \mu_{(\alpha)}\nabla^2\mathbf{v}_{(\alpha)}, \quad \text{in}\,\Omega_{(\alpha)}(t)\ \ (\alpha = I, II)\,, \tag{2.2}$$

$$\nabla\cdot\mathbf{v}_{(\alpha)} = 0, \quad \text{in}\,\Omega_{(\alpha)}(t)\ \ (\alpha = I, II)\,, \tag{2.3}$$

$$\partial_t c + \nabla\cdot\left(-D\nabla c + \mathbf{v}_{(II)}c\right) = 0, \quad \text{in}\,\Omega_{(II)}(t), \tag{2.4}$$

$$\mathbf{v}_{(I)} = \mathbf{v}_{(II)}, \quad \text{at}\,\Gamma(t), \tag{2.5}$$

$$\mathbf{v}_{(\alpha)}\cdot\mathbf{n} = v_n, \quad \text{at}\,\Gamma(t)\ \ (\alpha = I, II)\,, \tag{2.6}$$

$$\Big(\left(\mathbf{T}_{(I)} - \mathbf{T}_{(II)}\right)\cdot\mathbf{n}\Big)\cdot\mathbf{n} = \gamma(c)\ \left(\nabla\cdot\mathbf{n}\right), \quad \text{at}\,\Gamma(t), \tag{2.7}$$

$$\Big(\left(\mathbf{T}_{(I)} - \mathbf{T}_{(II)}\right)\cdot\mathbf{n}\Big)\cdot\mathbf{t} = -\mathbf{t}\cdot\nabla\gamma(c), \quad \text{at}\,\Gamma(t), \tag{2.8}$$

$$\left(-D\nabla c + \mathbf{v}_{(II)}c\right)\cdot\mathbf{n} = v_n\ c, \quad \text{at}\,\Gamma\left(t\right), \tag{2.9}$$

$$\mathbf{v}_{(II)} = \mathbf{0}, \quad \text{at}\,\Gamma_{\mathcal{G}}, \tag{2.10}$$

$$\left(-D\nabla c + \mathbf{v}_{(II)}c\right)\cdot\mathbf{n} = 0, \quad \text{at}\,\Gamma_{\mathcal{G}}. \tag{2.11}$$

To complete the model above, appropriate initial conditions, inflow and outflow boundary conditions can be added. Here we do not account for boundary layers. In this case, the upscaling procedure is independent of the choice of initial and external boundary conditions, and therefore these will not be specified here. We refer to [154] for a detailed explanation of the role of boundary conditions depending on the different formulations which gives rise to boundary layers in the solid-fluid interface.

2.2.3 Pore-scale model for the two-phase flow with constant surface tension

In this case, the pore-scale model is simpler as in Section 2.2.2. However, the surface tension is considered constant. Hence (2.4), (2.9) and (2.11) become superfluous. Recalling the remark in 1.2.1.2, while $\gamma(c) = \gamma$ in (2.7) and (2.8), these reduce to

$$\begin{aligned} &\Big(\big(\mathbf{T}_{(I)} - \mathbf{T}_{(II)}\big) \cdot \mathbf{n}\Big) \cdot \mathbf{n} = \gamma \ (\nabla \cdot \mathbf{n})\,, && \text{at}\, \Gamma(t), \\ &\Big(\big(\mathbf{T}_{(I)} - \mathbf{T}_{(II)}\big) \cdot \mathbf{n}\Big) \cdot \mathbf{t} = 0, && \text{at}\, \Gamma(t). \end{aligned}$$

The remaining equations are the same as in Section 2.2.2.

2.2.4 Pore-scale model for the unsaturated flow with constant surface tension

A further simplification is to assume the case of pore-scale unsaturated flow model with constant surface tension introduced in Section 1.2.1.3. This pore-scale model can be interpreted as a thin-film flow with an open surface where a liquid is attached to the wall of the pore and the middle domain is occupied by air. We assume the solute is absent in fluid-II. In this case, (2.4), (2.9) and (2.11) are excessive. Moreover, the model equations in Section 2.2.2 are further simplified by giving up the equations for $\alpha = I$, and keeping only the Navier-Stokes equations in $\Omega_{(II)}(t)$. At $\Gamma(t)$, (2.6) is valid for $\alpha = II$, and (2.7) and (2.8) shorten to

$$\begin{aligned} &\big(\mathbf{T}_{(II)} \cdot \mathbf{n}\big) \cdot \mathbf{n} = -\gamma \ (\nabla \cdot \mathbf{n})\,, && \text{at}\, \Gamma(t), \\ &\big(\mathbf{T}_{(II)} \cdot \mathbf{n}\big) \cdot \mathbf{t} = 0, && \text{at}\, \Gamma(t). \end{aligned}$$

2.3 The non-dimensional model equations

Here we present the non-dimensional models for two-phase/unsaturated flow. To this aim, we use reference quantities and rescale the dimensional ones as specified in Table 2.1. In particular, $\mu_{(II)}$ and $\rho_{(II)}$ are taken as reference viscosity, respectively density. Table 2.1 introduces two length scales, L and l. In a general porous medium, L would reflect the length scale of the entire medium, where l is the one of a pore. As we let a single pore represent the porous medium, we use the length and the width of the pore as described in Section 2.2.1. In the same spirit, here we define the non-dimensional number $\epsilon := \frac{l}{L} > 0$, and assume that ϵ is small. Observe now that the x and y coordinates are scaled differently, so that they become both of order 1, $\mathcal{O}(1)$. Based on this, the derivatives change into $\frac{\partial}{\partial \hat{x}} = L \, \frac{\partial}{\partial x}$, $\frac{\partial}{\partial \hat{y}} = \epsilon \, L \, \frac{\partial}{\partial y}$. The non-dimensional gradient is $\hat{\nabla} := \left(\partial_{\hat{x}}, \frac{1}{\epsilon}\partial_{\hat{y}}\right)$ due to the different scaling in x and y-direction.

Table 2.1: Reference and non-dimensional quantities

Variables	Reference values	Non-dimensional variables
time	t_{ref}	$\hat{t} = t/t_{ref}$
space	$x_{ref} = L,$	$\hat{x} = x/L$
	$y_{ref} = l$	$\hat{y} = y/l = y/\left(\epsilon \, L\right)$
depth of the wetting fluid		$\hat{d}^{\epsilon} = d/l = d/\left(\epsilon \, L\right)$
velocities	$v_{ref} = L/t_{ref}$	$\hat{\mathbf{v}}^{\epsilon}_{(I)} = \mathbf{v}_{(I)}/v_{ref}$
		$\hat{\mathbf{v}}^{\epsilon}_{(II)} = \mathbf{v}_{(II)}/v_{ref}$
densities	$\rho_{ref} = \rho_{(II)}$	$\hat{\rho}_{(I)} = \rho_{(I)}/\rho_{(II)} = 1/N$
		$\hat{\rho}_{(II)} = 1$
pressures	$p_{ref} = \frac{L^4 \, \rho_{ref}}{t_{ref}^2 \, l^2}$	$\hat{p}^{\epsilon}_{(I)} = p_{(I)}/p_{ref}$
		$\hat{p}^{\epsilon}_{(II)} = p_{(II)}/p_{ref}$
kinematic viscosities	$\mu_{ref} = \frac{l^2 \, p_{ref}}{L \, v_{ref}} = \mu_{(II)}$	$\hat{\mu}_{(I)} = \mu_{(I)}/\mu_{(II)} = 1/M$
		$\hat{\mu}_{(II)} = 1$
surface tension	γ_{ref}	$\hat{\gamma}(\hat{c}^{\epsilon}) = \gamma(c)/\gamma_{ref},$
		$\hat{\gamma} = \gamma/\gamma_{ref} = 1,$ if γ is constant
diffusion coefficient	$D_{ref} = L^2/t_{ref}$	$\hat{D} = D/D_{ref}$
molar concentration	c_{ref}	$\hat{c}^{\epsilon} = c/c_{ref}$
capillary number		Ca $= \left(\mu_{ref} \, v_{ref}\right)/\gamma_{ref}$

Some assumptions are made in Table 2.1 by choosing the scaling for μ_{ref}, D_{ref} and p_{ref}. The capillary effects are accounted for by the capillary number, $\mathrm{Ca} = \left(\mu_{ref} \, v_{ref}\right)/\gamma_{ref}$, which is ratio of the capillary and viscous forces. The ratio of the time scales for the diffusion and the convective transport, referred to as the Péclet number, $Pe = \frac{v_{ref} \, x_{ref}}{D_{ref}}$ is chosen moderate w.r.t ϵ. For simplicity, the Péclet number is taken equal to 1. In [33, 34, 98, 132, 148, 149, 157, 158, 176, 178, 179] the case of moderate Péclet number (when diffusion dominates or is in balance with the transport) and in [35, 95, 109, 172] the case of high Péclet number (when the convective transport dominates the diffusion) are considered. Additionally, the scaling of the p_{ref} and μ_{ref} are chosen such that the Reynolds number, $Re = \frac{\rho_{ref} \, v_{ref} \, x_{ref}}{\mu_{ref}}$ is moderate, namely equal to

1, and the Euler number, $Eu = \frac{p_{ref}}{v_{ref}^2\, \rho_{ref}}$, is equal to ϵ^{-2}. These choices ensure laminar flow and that the pressure drop dominates the flow, which are needed to ensure validity of Darcy's law on the macro scale.

Note that the dimensionless parameters M, N appearing in Table 2.1,

$$M := \mu_{(II)}/\mu_{(I)},\ N := \rho_{(II)}/\rho_{(I)},$$

may also depend on ϵ. In this respect, here we restrict to the case $N = 1$, while M is assumed first $\mathcal{O}(1)$, and later the limit $M \to \infty$ is considered to show that the two-phase model reduces to the unsaturated, single-phase one.

In the non-dimensional setting, the pore space occupied by the two fluids is

$$\hat{\Omega}^{\epsilon}_{(I)}(\hat{t}) := \{(\hat{x}, \hat{y}) \in \mathbb{R}^2 | 0 < \hat{x} < 1, -1 + \hat{d}^{\epsilon}(\hat{x}, \hat{t}) < \hat{y} < 0\}, \tag{2.12}$$

$$\hat{\Omega}^{\epsilon}_{(II)}(\hat{t}) := \{(\hat{x}, \hat{y}) \in \mathbb{R}^2 | 0 < \hat{x} < 1, -1 < \hat{y} < -1 + \hat{d}^{\epsilon}(\hat{x}, \hat{t})\}. \tag{2.13}$$

The fluid-fluid and fluid-solid interfaces become

$$\begin{aligned} \hat{\Gamma}^{\epsilon}(\hat{t}) &:= \{(\hat{x}, \hat{y}) \in \mathbb{R}^2 | 0 < \hat{x} < 1, \hat{y} = -1 + \hat{d}^{\epsilon}(\hat{x}, \hat{t})\}, \\ \hat{\Gamma}_{\mathcal{G}} &:= \{(\hat{x}, \hat{y}) \in \mathbb{R}^2 | 0 < \hat{x} < 1, \hat{y} = -1\}. \end{aligned}$$

The normal and tangent unit vectors are, respectively

$$\hat{\mathbf{n}}^{\epsilon} := \frac{\left(-\epsilon\, \partial_{\hat{x}} \hat{d}^{\epsilon}, 1\right)}{\sqrt{1 + \left(\epsilon\, \partial_{\hat{x}} \hat{d}^{\epsilon}\right)^2}}, \text{ and } \hat{\mathbf{t}}^{\epsilon} := \frac{\left(1, \epsilon\, \partial_{\hat{x}} \hat{d}^{\epsilon}\right)}{\sqrt{1 + \left(\epsilon\, \partial_{\hat{x}} \hat{d}^{\epsilon}\right)^2}}.$$

The normal velocity becomes

$$\hat{v}^{\epsilon}_{n} := \frac{\epsilon\, \partial_{\hat{t}} \hat{d}^{\epsilon}}{\sqrt{1 + \left(\epsilon\, \partial_{\hat{x}} \hat{d}^{\epsilon}\right)^2}}.$$

The non-dimensional stress tensors are

$$\hat{\mathbf{T}}^\epsilon_{(I)} = -\hat{p}^\epsilon_{(I)}\,\mathbf{I} + \frac{\epsilon^2}{M}\left\{\left(\hat\nabla\hat{\mathbf{v}}^\epsilon_{(I)}\right) + \left(\hat\nabla\hat{\mathbf{v}}^\epsilon_{(I)}\right)^T\right\},$$

$$\hat{\mathbf{T}}^\epsilon_{(II)} = -\hat{p}^\epsilon_{(II)}\,\mathbf{I} + \epsilon^2\left\{\left(\hat\nabla\hat{\mathbf{v}}^\epsilon_{(II)}\right) + \left(\hat\nabla\hat{\mathbf{v}}^\epsilon_{(II)}\right)^T\right\}.$$

2.3.1 Non-dimensional model for the two-phase flow with solute-dependent surface tension

Substituting the non-dimensional variables into the pore-scale model in Section 2.2.2, for every $\hat{t} > 0$ the non-dimensional model equations for the two-phase flow model with solute-dependent surface tension become

$$\epsilon^2\left(\partial_{\hat t}\hat{\mathbf{v}}^\epsilon_{(I)} + \left(\hat{\mathbf{v}}^\epsilon_{(I)}\cdot\hat\nabla\right)\hat{\mathbf{v}}^\epsilon_{(I)}\right) + \hat\nabla\hat{p}^\epsilon_{(I)} - \frac{\epsilon^2}{M}\hat\nabla^2\hat{\mathbf{v}}^\epsilon_{(I)} = 0, \quad \text{in } \hat\Omega^\epsilon_{(I)}(\hat t), \tag{2.14}$$

$$\epsilon^2\left(\partial_{\hat t}\hat{\mathbf{v}}^\epsilon_{(II)} + \left(\hat{\mathbf{v}}^\epsilon_{(II)}\cdot\hat\nabla\right)\hat{\mathbf{v}}^\epsilon_{(II)}\right) + \hat\nabla\hat{p}^\epsilon_{(II)} - \epsilon^2\hat\nabla^2\hat{\mathbf{v}}^\epsilon_{(II)} = 0, \quad \text{in } \hat\Omega^\epsilon_{(II)}(\hat t), \tag{2.15}$$

$$\hat\nabla\cdot\hat{\mathbf{v}}^\epsilon_{(\alpha)} = 0, \quad \text{in } \hat\Omega^\epsilon_{(\alpha)}(\hat t)\ \left(\alpha = I, II\right), \tag{2.16}$$

$$\partial_{\hat t}\hat{c}^\epsilon - \hat\nabla\cdot\left(\hat{D}\hat\nabla\left(\hat{c}^\epsilon\right) - \hat{\mathbf{v}}^\epsilon_{(II)}\hat{c}^\epsilon\right) = 0, \quad \text{in } \hat\Omega^\epsilon_{(II)}(\hat t). \tag{2.17}$$

The boundary conditions at the fluid-fluid interface are

$$\hat{\mathbf{v}}^\epsilon_{(I)} = \hat{\mathbf{v}}^\epsilon_{(II)}, \qquad \text{at } \hat\Gamma^\epsilon(\hat t), \tag{2.18}$$

$$\hat{\mathbf{v}}^\epsilon_{(\alpha)}\cdot\hat{\mathbf{n}}^\epsilon = \hat{v}^\epsilon_n, \qquad \text{at } \hat\Gamma^\epsilon(\hat t)\ \left(\alpha = I, II\right), \tag{2.19}$$

$$\left(-\hat{D}\hat\nabla\hat{c}^\epsilon + \hat{\mathbf{v}}^\epsilon_{(II)}\hat{c}^\epsilon\right)\cdot\hat{\mathbf{n}}^\epsilon = \hat{c}^\epsilon\,\hat{v}^\epsilon_n, \qquad \text{at } \hat\Gamma^\epsilon\left(\hat t\right), \tag{2.20}$$

$$\left(\left(\hat{\mathbf{T}}^\epsilon_{(I)} - \hat{\mathbf{T}}^\epsilon_{(II)}\right)\cdot\hat{\mathbf{n}}^\epsilon\right)\cdot\hat{\mathbf{n}}^\epsilon = \frac{\epsilon^2}{\mathrm{Ca}}\,\hat\gamma\left(\hat{c}^\epsilon\right)\left(\hat\nabla\cdot\hat{\mathbf{n}}^\epsilon\right), \qquad \text{at } \hat\Gamma^\epsilon\left(\hat t\right), \tag{2.21}$$

$$\left(\left(\hat{\mathbf{T}}^\epsilon_{(I)} - \hat{\mathbf{T}}^\epsilon_{(II)}\right)\cdot\hat{\mathbf{n}}^\epsilon\right)\cdot\hat{\mathbf{t}}^\epsilon = -\frac{\epsilon^2}{\mathrm{Ca}}\left(\hat{\mathbf{t}}^\epsilon\cdot\hat\nabla\hat\gamma(\hat{c}^\epsilon)\right), \qquad \text{at } \hat\Gamma^\epsilon\left(\hat t\right). \tag{2.22}$$

At the fluid-solid interface, the boundary conditions are

$$\hat{\mathbf{v}}^\epsilon_{(II)} = \mathbf{0}, \qquad \text{at } \hat\Gamma_{\mathcal{G}}, \tag{2.23}$$

$$\left(-\hat{D}\hat\nabla\hat{c}^\epsilon + \hat{\mathbf{v}}^\epsilon_{(II)}\hat{c}^\epsilon\right)\cdot\hat{\mathbf{n}}^\epsilon = 0, \qquad \text{at } \hat\Gamma_{\mathcal{G}}. \tag{2.24}$$

At $\hat{y} = 0$ we apply symmetry conditions for all variables.

2.3.2 Non-dimensional model for the two-phase flow with constant surface tension

Similar to Section 2.2.3, we consider here the case without solute and with γ being constant. With $\gamma_{ref} = \gamma$, one gets $\hat{\gamma} = 1$ and (2.21), hence (2.22) become

$$\left(\left(\hat{\mathbf{T}}^{\epsilon}_{(\mathbf{I})} - \hat{\mathbf{T}}^{\epsilon}_{(\mathbf{II})}\right) \cdot \hat{\mathbf{n}}^{\epsilon}\right) \cdot \hat{\mathbf{n}}^{\epsilon} = \frac{\epsilon^2}{\mathrm{Ca}} \hat{\nabla} \cdot \hat{\mathbf{n}}^{\epsilon}, \qquad \text{at } \hat{\Gamma}^{\epsilon}\left(\hat{t}\right), \tag{2.25}$$

$$\left(\left(\hat{\mathbf{T}}^{\epsilon}_{(\mathbf{I})} - \hat{\mathbf{T}}^{\epsilon}_{(\mathbf{II})}\right) \cdot \hat{\mathbf{n}}^{\epsilon}\right) \cdot \hat{\mathbf{t}}^{\epsilon} = 0, \qquad \text{at } \hat{\Gamma}^{\epsilon}\left(\hat{t}\right). \tag{2.26}$$

Further, (2.17), (2.20) and (2.24) are not needed anymore and the remaining equations are the same as in the above section.

2.3.3 Non-dimensional model for unsaturated flow with constant surface tension

Continuing as in Section 2.2.4, assuming that fluid-I does not influence the flow of fluid-II and in the absence of solute, one ends up with (2.15), (2.16), (2.19) (for $\alpha = II$), (2.23) and

$$\left(\hat{\mathbf{T}}^{\epsilon}_{(II)} \cdot \hat{\mathbf{n}}^{\epsilon}\right) \cdot \hat{\mathbf{n}}^{\epsilon} = -\frac{\epsilon^2}{\mathrm{Ca}} \hat{\nabla} \cdot \hat{\mathbf{n}}^{\epsilon}, \qquad \text{at } \hat{\Gamma}^{\epsilon}\left(\hat{t}\right), \tag{2.27}$$

$$\left(\hat{\mathbf{T}}^{\epsilon}_{(II)} \cdot \hat{\mathbf{n}}^{\epsilon}\right) \cdot \hat{\mathbf{t}}^{\epsilon} = 0, \qquad \text{at } \hat{\Gamma}^{\epsilon}\left(\hat{t}\right). \tag{2.28}$$

2.4 Asymptotic expansion

We use an asymptotic expansion w.r.t. ϵ to derive transversally averaged upscaled (effective) models at the Darcy scale. Since in this section only the non-dimensional variables are used, for the ease of presentation the hats are suppressed. We assume that all the variables are smooth. Then we use the homogenization ansatz, namely that all variables can be expanded regularly w.r.t. ϵ,

$$\begin{aligned} p^{\epsilon}_{(\alpha)}(x,y,t) &= p^{0}_{(\alpha)}(x,y,t) + \epsilon p^{1}_{(\alpha)}(x,y,t) + \mathcal{O}(\epsilon^2)\ (\alpha = I, II), \\ v^{\epsilon}_{(\alpha,k)}(x,y,t) &= v^{0}_{(\alpha,k)}(x,y,t) + \epsilon v^{1}_{(\alpha,k)}(x,y,t) + \mathcal{O}(\epsilon^2)\ (\alpha = I, II, k = 1,2), \\ c^{\epsilon}(x,y,t) &= c^{0}(x,y,t) + \epsilon c^{1}(x,y,t) + \mathcal{O}(\epsilon^2), \\ d^{\epsilon}(x,t) &= d^{0}(x,t) + \epsilon d^{1}(x,t) + \mathcal{O}(\epsilon^2). \end{aligned} \tag{2.29}$$

where $p^{j}_{(\alpha)}(x,y,t), v^{j}_{(\alpha,k)}(x,y,t), c^{j}(x,y,t), d^{j}(x,t)$ are functions describing the $\mathcal{O}(\epsilon^j)$ order approximation (for $j = 0,1,2,\cdots$) of the corresponding variables. We will now insert these expansions in the model equations and equate terms of the same order in ϵ to find the transversally averaged equations. We do this for different regimes, and end up with different upscaled models.

2.4.1 Two-phase flow with solute-dependent surface tension

We start with the model for two-phase flow with solute-dependent surface tension (2.14)-(2.24). At this point we assume that M is $\mathcal{O}(1)$ w.r.t. ϵ.

2.4.1.1 Mass conservation

To derive an effective equation for the mass conservation, we follow the ideas in [33, 95, 179]. Substituting the asymptotic expansion (2.29) in the mass conservation equation (2.16) and restricting the writing up to the $\mathcal{O}(\epsilon^0)$ terms gives

$$\frac{1}{\epsilon}\,\partial_y v^{0}_{(\alpha,2)} + \left(\partial_x v^{0}_{(\alpha,1)} + \partial_y v^{1}_{(\alpha,2)}\right) + \mathcal{O}(\epsilon) = 0, \text{ in } \Omega^{\epsilon}_{(\alpha)}(t). \tag{2.30}$$

To show that $v^{0}_{(\alpha,2)} = 0$ in $\Omega^{\epsilon}_{(\alpha)}(t)$, we use (2.29) in the kinematic conditions (2.19) and obtain

$$v^{0}_{(\alpha,2)} + \epsilon\left(v^{1}_{(\alpha,2)} - v^{0}_{(\alpha,1)}\,\partial_x d^0 - \partial_t d^0\right) + \mathcal{O}(\epsilon^2) = 0, \text{ at } \Gamma^{\epsilon}(t). \tag{2.31}$$

The lowest order terms in (2.30) - (2.31) give

$$\partial_y v^0_{(\alpha,2)} = 0, \text{ in } \Omega^\epsilon_{(\alpha)}(t), \text{ and } v^0_{(\alpha,2)} = 0, \text{ at } \Gamma^\epsilon(t),$$

while (2.23) and the symmetry condition at $y = 0$ lead to

$$v^0_{(\alpha,2)} = 0, \text{ in } \Omega^\epsilon_{(\alpha)}(t). \tag{2.32}$$

To upscale the mass balance for the fluids, we consider a thin segment of the pore space, as sketched in Figure 2.2.

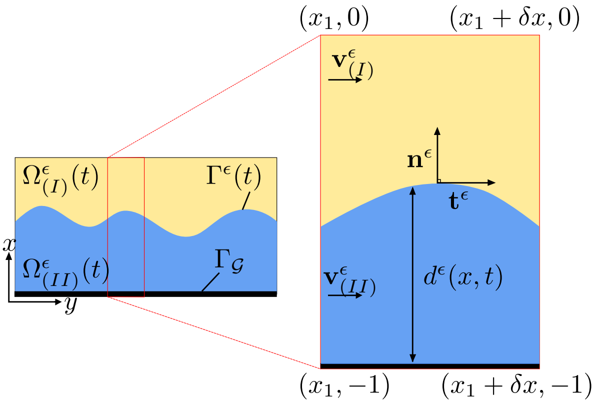

Figure 2.2: Thin section of the pore space

Let $Y_{(I)} := \{(x,y) | x_1 < x < x_1 + \delta x, -1 + d^\epsilon < y < 0\}$ be the region in this segment that is occupied by fluid-I. By integrating (2.16) over $Y_{(I)}$, one obtains

$$\int_{Y_{(I)}} \nabla \cdot \mathbf{v}^\epsilon_{(I)} \, dV_{(I)} = 0.$$

In the above equation, we apply the theorem of Gauss and divide all terms by δx, then using (2.19) and the asymptotic expansions (2.29) to get

$$\frac{1}{\delta x}\int_{-1+d^0}^{0} v^0_{(I,1)}\, dy|_{x=x_1+\delta x} - \frac{1}{\delta x}\int_{-1+d^0}^{0} v^0_{(I,1)}\, dy|_{x=x_1} + \frac{1}{\delta x}\int_{x_1}^{x_1+\delta x} v^1_{(I,2)}\, dx|_{y=0}$$
$$-\frac{1}{\delta x}\int_{x_1}^{x_1+\delta x} \partial_t d^0\, dx + \mathcal{O}(\epsilon) = 0.$$

Using the symmetry condition at $y = 0$ and equating the lowest order terms in the above gives

$$\frac{1}{\delta x}\int_{-1+d^0}^{0} \left(v^0_{(I,1)}|_{x=x_1+\delta x} - v^0_{(I,1)}|_{x=x_1}\right) dy - \frac{1}{\delta x}\int_{x_1}^{x_1+\delta x} \partial_t d^0\, dx = 0.$$

Defining the total flux of fluid-I as

$$\overline{v}^0_{(I,1)}(x,t) := \int_{-1+d^0}^{0} v^0_{(I,1)}(x,y,t)\, dy, \tag{2.33}$$

and letting $\delta x \to 0$, one obtains

$$\partial_x \overline{v}^0_{(I,1)} - \partial_t d^0 = 0, \text{ for all } 0 < x < 1 \text{ and } t > 0. \tag{2.34}$$

Similarly using the fluid-II region $Y_{(II)} := \{(x,y)|x_1 < x < x_1 + \delta x, -1 < y < -1 + d^\epsilon\}$, for

$$\overline{v}^0_{(II,1)}(x,t) := \int_{-1}^{-1+d^0} v^0_{(II,1)}(x,y,t)\, dy, \tag{2.35}$$

one obtains

$$\partial_x \overline{v}^0_{(II,1)} + \partial_t d^0 = 0, \text{ for all } 0 < x < 1 \text{ and } t > 0. \tag{2.36}$$

Remark. *Recalling that the fluids are incompressible, observe that, since d^0 is the thickness of the wetting phase layer in the half-pore, it can be regarded as the saturation of the wetting fluid. In this sense* (2.34) *and* (2.36) *are the effective mass balance equations for the two fluid phases.*

2.4.1.2 Solute transport

To upscale the solute transport, which is needed when considering the Marangoni effect, one uses the asymptotic expansion (2.29) in (2.17) to get

$$\begin{aligned}\partial_t c^0 - \left(\partial_x, \frac{1}{\epsilon}\partial_y\right) \cdot D \left(\partial_x, \frac{1}{\epsilon}\partial_y\right) \left(c^0 + \epsilon c^1 + \epsilon^2 c^2\right) \\ + \left(\partial_x, \frac{1}{\epsilon}\partial_y\right) \cdot \left(v^0_{(II,1)}, v^0_{(II,2)} + \epsilon v^1_{(II,2)}\right) \left(c^0 + \epsilon c^1\right) + \mathcal{O}(\epsilon) = 0, \text{ in } \Omega^\epsilon_{(II)}(t).\end{aligned} \tag{2.37}$$

First, we show that c^0 and c^1 do not depend on y. The ϵ^{-2} order term in (2.37) is leading to

$$\partial_{yy} c^0 = 0, \text{ in } \Omega^\epsilon_{(II)}(t).$$

From the ϵ^{-1} order term in the boundary conditions (2.20) and (2.24), one obtains

$$\partial_y c^0 = 0, \text{ at } \Gamma^\epsilon(t) \text{ and } \Gamma_{\mathcal{G}}.$$

This implies that c^0 does not depend on y,

$$c^0 = c^0(x,t), \text{ in } \Omega^\epsilon_{(II)}(t).$$

In a similar fashion, using this, (2.32), the ϵ^{-1} order term in (2.37) and ϵ^0 order term in (2.20), (2.24), one obtains

$$c^1 = c^1(x,t), \text{ in } \Omega^\epsilon_{(II)}(t).$$

The non-dimensional equation describing the solute concentration (2.17) can be written as

$$\frac{1}{\epsilon^2}\partial_y \left(D\, \partial_y c^\epsilon\right) - \frac{1}{\epsilon}\, \partial_y \left(v^\epsilon_{(II,2)}\, c^\epsilon\right) - \partial_t c^\epsilon + \partial_x \left(D\, \partial_x c^\epsilon - v^\epsilon_{(II,1)}\, c^\epsilon\right) = 0.$$

We integrate the above equation w.r.t. y from $y = -1$ to $y = -1 + d^\epsilon$. Applying the Leibniz rule in the last two terms and taking into account that d^ϵ depends on x and t, one gets

$$\left[\frac{1}{\epsilon^2}D\partial_y c^\epsilon - \frac{1}{\epsilon}v^\epsilon_{(II,2)}c^\epsilon\right]_{y=-1}^{y=-1+d^\epsilon} - \partial_t\left(\int_{-1}^{-1+d^\epsilon} c^\epsilon dy\right) + \partial_t d^\epsilon c^\epsilon|_{y=-1+d^\epsilon}$$
$$+\,\partial_x\left(\int_{-1}^{-1+d^\epsilon}\left(D\partial_x c^\epsilon - v^\epsilon_{(II,1)}c^\epsilon\right)dy\right) - \partial_x d^\epsilon\left(D\partial_x c^\epsilon - v^\epsilon_{(II,1)}c^\epsilon\right)|_{y=-1+d^\epsilon} = 0.$$

We insert the asymptotic expansion (2.29) in the above equation, recalling that c^0 and c^1 do not depend on y and that $\partial_y c^2 = 0$ and $v^1_{(II,2)} = 0$ at $y = -1$, since $v^0_{(II,2)} = 0$ in $\Omega^\epsilon_{(II)}(t)$, one obtains

$$\left(D\partial_y c^2 - v^1_{(II,2)}c^0\right)|_{y=-1+d^0} - \partial_t\left(c^0\int_{-1}^{-1+d^0} 1\,dy\right) + \partial_t d^0\, c^0|_{y=-1+d^0}$$
$$+\,\partial_x\left(D\,\partial_x c^0\left(\int_{-1}^{-1+d^0} 1\,dy\right) - c^0\left(\int_{-1}^{-1+d^0} v^0_{(II,1)}\,dy\right)\right)$$
$$-\,\partial_x d^0\left(D\partial_x c^0 - c^0\, v^0_{(II,1)}\right)|_{y=-1+d^0} + \mathcal{O}(\epsilon) = 0.$$

Using (2.35) and the ϵ order terms from the boundary condition (2.20) at $y = -1 + d^0$, one obtains the effective equation for the solute transport

$$\partial_t\left(c^0\, d^0\right) + \partial_x\left(c^0\,\overline{v}^0_{(II,1)}\right) - \partial_x(D\, d^0\,\partial_x c^0) = 0, \text{ for all } 0 < x < 1 \text{ and } t > 0. \quad (2.38)$$

2.4.1.3 Momentum conservation

We apply the asymptotic expansion (2.29) in the horizontal and vertical component of the momentum equation for fluid-II (2.15). Recalling that $v^0_{(II,2)} = 0$, in $\Omega^\epsilon_{(II)}(t)$, for all $t > 0$ one has

$$-\partial_{yy}v^0_{(II,1)} + \partial_x p^0_{(II)} - \epsilon\,\partial_{yy}v^1_{(II,1)} + \epsilon\,\partial_x p^1_{(II)} + \mathcal{O}(\epsilon^2) = 0, \quad (2.39)$$
$$\frac{1}{\epsilon}\,\partial_y p^0_{(II)} + \partial_y p^1_{(II)} + \epsilon\,\partial_y p^2_{(II)} - \epsilon\,\partial_{yy}v^1_{(II,2)} + \mathcal{O}(\epsilon^2) = 0. \quad (2.40)$$

Restricting to ϵ^{-1} order term in (2.40), for all $0 < x < 1$ and $t > 0$, one gets

$$p^0_{(II)} = p^0_{(II)}(x,t).$$

For all $t > 0$, the dominant terms in (2.39) give

$$\partial_{yy} v^0_{(II,1)} = \partial_x p^0_{(II)}, \text{ in } \Omega^\epsilon_{(II)}(t). \tag{2.41}$$

Integrating the above equation in y and taking into account that $p^0_{(II)}$ is independent of y, we obtain

$$\partial_y v^0_{(II,1)} = \partial_x p^0_{(II)}\, y + A_1(x,t), \text{ in } \Omega^\epsilon_{(II)}(t), \tag{2.42}$$

where $A_1(x,t)$ is an integrating constant that will be fixed using boundary condition for $v^0_{(II,1)}$. We now assume that the surface tension $\gamma = \gamma(c^\epsilon)$ depends smoothly on the solute concentration. Using (2.29) and expanding $\gamma(c^\epsilon)$ around c^0 gives

$$\gamma(c^\epsilon) = \gamma\left(c^0\right) + \epsilon\, c^1\, \gamma'\left(c^0\right) + \mathcal{O}(\epsilon^2).$$

We apply the asymptotic expansion (2.29) in the boundary condition (2.22). Using the above equation and recalling that $v^0_{(\alpha,2)} = 0$ at $\Gamma^\epsilon(t)$ and that c^0 is independent of y, we get

$$\begin{aligned}
&\frac{1}{\epsilon}\left(\frac{1}{M}\partial_y v^0_{(I,1)} - \partial_y v^0_{(II,1)}\right) + \left(\frac{1}{M}\partial_y v^1_{(I,1)} - \partial_y v^1_{(II,1)}\right) + \epsilon\left(\frac{1}{M}\partial_y v^2_{(II,1)} - \partial_y v^2_{(II,1)}\right)\\
&+ \epsilon\left(\frac{1}{M}\partial_x v^1_{(I,2)} - \partial_x v^1_{(II,2)}\right) + 2\epsilon\partial_x d^0\left(\frac{1}{M}\partial_y v^1_{(I,2)} - \partial_y v^1_{(II,2)}\right)\\
&- 2\epsilon\partial_x d^0\left(\frac{1}{M}\partial_x v^0_{(I,1)} - \partial_x v^0_{(II,1)}\right) - \epsilon\left(\partial_x d^0\right)^2\left(\frac{1}{M}\partial_y v^0_{(I,1)} - \partial_y v^0_{(II,1)}\right)\\
&+ \frac{1}{\mathrm{Ca}}\partial_x \gamma(c^0) + \frac{\epsilon}{\mathrm{Ca}}\partial_x\Big(c^1\gamma'(c^0)\Big) + \mathcal{O}(\epsilon^2) = 0, \text{ at } \Gamma^\epsilon(t).
\end{aligned} \tag{2.43}$$

At this point, the upscaling depends on the capillary number Ca. We will discuss the cases with $\mathrm{Ca} = \epsilon^\beta\, \overline{\mathrm{Ca}}$, for $0 \le \beta \le 3$, where $\overline{\mathrm{Ca}} = \mathcal{O}(1)$. We start by assuming $\mathrm{Ca} = \mathcal{O}(1)$ thus $\beta = 0$. From (2.43), one gets the tangential stress boundary condition

$$\partial_y v^0_{(II,1)} = \frac{1}{M}\, \partial_y v^0_{(I,1)}, \text{ at } \Gamma^\epsilon(t). \tag{2.44}$$

Using the above in (2.42) leads to

$$\frac{1}{M}\,\partial_y v^0_{(I,1)}|_{y=-1+d^0} = (-1+d^0)\,\partial_x p^0_{(II)} + A_1(x,t), \text{ in } \Omega^\epsilon_{(II)}(t). \tag{2.45}$$

Applying the asymptotic expansion (2.29) into (2.14) and using (2.32), for all $t>0$ one has

$$-\frac{1}{M}\,\partial_{yy} v^0_{(I,1)} + \partial_x p^0_{(I)} - \frac{\epsilon}{M}\,\partial_{yy} v^1_{(I,1)} + \epsilon\,\partial_x p^1_{(I)} + \mathcal{O}(\epsilon^2) = 0, \text{ in } \Omega^\epsilon_{(I)}(t), \tag{2.46}$$

$$\frac{1}{\epsilon}\,\partial_y p^0_{(I)} + \partial_y p^1_{(I)} + \epsilon\,\partial_y p^2_{(I)} - \frac{\epsilon}{M}\,\partial_{yy} v^1_{(I,2)} + \mathcal{O}(\epsilon^2) = 0, \text{ in } \Omega^\epsilon_{(I)}(t). \tag{2.47}$$

The lowest order term in (2.47) gives

$$p^0_{(I)} = p^0_{(I)}(x,t), \text{ for all } 0<x<1. \tag{2.48}$$

For all $t>0$, the dominating terms in (2.46) satisfy

$$\partial_{yy} v^0_{(I,1)} = M\,\partial_x p^0_{(I)}, \text{ in } \Omega^\epsilon_{(I)}(t). \tag{2.49}$$

We integrate the above equation w.r.t. y. We use (2.48) and the symmetry condition $\partial_y v^0_{(I,1)}(x,y,t) = 0$ at $y=0$, which leads to

$$\partial_y v^0_{(I,1)} = M\,\partial_x p^0_{(I)}\, y, \text{ in } \Omega^\epsilon_{(I)}(t). \tag{2.50}$$

We determine $A_1(x,t)$ from (2.45), by using (2.50) at $y=-1+d^0$, one gets for all $t>0$

$$\partial_y v^0_{(II,1)} = \partial_x p^0_{(II)}\, y + (-1+d^0)\left(\partial_x p^0_{(I)} - \partial_x p^0_{(II)}\right), \text{ in } \Omega^\epsilon_{(II)}(t). \tag{2.51}$$

The lowest order terms in (2.23) imply that $v^0_{(II,1)} = 0$ at $y=-1$. Hence, integrating the above equation in y, one obtains

$$v^0_{(II,1)} = \frac{\partial_x p^0_{(II)}(y^2-1)}{2} + (-1+d^0)\left(\partial_x p^0_{(I)} - \partial_x p^0_{(II)}\right)(y+1), \text{ in } \Omega^\epsilon_{(II)}(t). \tag{2.52}$$

Integrating the above in y from $y=-1+d^0$ to $y=-1$ and using (2.35), yields

$$\overline{v}^0_{(II,1)}(x,t) = -\frac{(d^0)^3}{3}\,\partial_x p^0_{(II)} - \frac{(1-d^0)\,(d^0)^2}{2}\,\partial_x p^0_{(I)},\text{ for all } 0<x<1 \text{ and } t>0.) \tag{2.53}$$

To derive an effective equation for the velocity of fluid-I, we integrate (2.50) twice w.r.t. y. To determine the integration constants we use the continuity of the velocity at the fluid-fluid interface. The lowest order terms in (2.18) imply $v^0_{(I,1)} = v^0_{(II,1)}$ and hence

$$\overline{v}^0_{(I,1)} = -\left[\frac{M\,(1-d^0)^3}{3} + d^0\,(1-d^0)^2\right]\partial_x p^0_{(I)} - \frac{(1-d^0)\,(d^0)^2}{2}\,\partial_x p^0_{(II)}, \tag{2.54}$$

for all $0<x<1$ and $t>0$.

2.4.1.4 Effect of Ca

We recall that the boundary conditions coming from the normal (2.21) and the tangential (2.22) components of the jump in the normal stress depends on the capillary number, Ca. To complete the upscaled model representing the effective behaviour for two-phase flow, we still have to find a relationship between the pressure difference of the fluids (capillary pressure) and the saturation in the porous medium. To this aim, we rewrite (2.21) as

$$\begin{aligned}
&-\frac{1}{\epsilon^2}\left(p^\epsilon_{(I)} - p^\epsilon_{(II)}\right) + \frac{2}{\epsilon}\,\left(\partial_y v^\epsilon_{(I,2)} - M\,\partial_y v^\epsilon_{(II,2)}\right) - (\partial_x d^\epsilon)^2\left(p^\epsilon_{(I)} - p^\epsilon_{(II)}\right)\\
&+2\,\partial_x d^\epsilon\left(\partial_y v^\epsilon_{(I,1)} - M\,\partial_y v^\epsilon_{(II,2)}\right) - 2\,\epsilon\,\partial_x d^\epsilon\left(\partial_x v^\epsilon_{(I,2)} - M\,\partial_x v^\epsilon_{(II,2)}\right)\\
&+\frac{\epsilon\,\gamma(c^\epsilon)\,\partial_{xx} d^\epsilon}{\mathrm{Ca}} + \mathcal{O}(\epsilon^2) = 0,\ \text{at } \Gamma^\epsilon(t).
\end{aligned} \tag{2.55}$$

Whenever $\mathrm{Ca} = \mathcal{O}(1)$ thus $\beta = 0$, applying the asymptotic expansion (2.29) in the above equation and recalling (2.32) gives

$$p^0_{(I)} - p^0_{(II)} = 0,\text{ for all } 0<x<1 \text{ and } t>0. \tag{2.56}$$

This means that in the upscaled model the pressures in both phases are equal. Since $p^0_{(I)} = p^0_{(II)}$ in the pressure relation (2.56), for simplicity, we set $p^0 = p^0_{(\alpha)}$ and the effective velocities (2.53) and (2.54) become, for all $0 < x < 1$ and $t > 0$

$$\overline{v}^0_{(II,1)} = -\frac{(d^0)^2\,(3-d^0)}{6}\,\partial_x p^0, \tag{2.57}$$

$$\overline{v}^0_{(I,1)} = -\left(\frac{M(1-d^0)^3}{3} + \frac{d^0\,(1-d^0)\,(2-d^0)}{2}\right)\partial_x p^0. \tag{2.58}$$

Thus, the upscaled model with $\mathrm{Ca} = \mathcal{O}(1)$ is represented by the mass conservation equations (2.34), (2.36), the effective velocities (2.57), (2.58) and the solute transport (2.38). This can be expressed in terms of three primary variables, the saturation of the wetting fluid d^0, the pressure p^0 (recall that the two fluid pressures are equal) and the concentration c^0. Specifically, for all $0 < x < 1$ and $t > 0$ one has

$$\begin{aligned} \partial_t d^0 + \partial_x\left[\left(\frac{M(1-d^0)^3}{3} + \frac{d^0\,(1-d^0)\,(2-d^0)}{2}\right)\partial_x p^0\right] &= 0, \\ \partial_t d^0 - \partial_x\left[\frac{(d^0)^2\,(3-d^0)}{6}\,\partial_x p^0\right] &= 0, \\ \partial_t\left(c^0\,d^0\right) + \partial_x\left[c^0\,\left(\frac{(d^0)^2\,(3-d^0)}{6}\right)\partial_x p^0\right] - \partial_x(D\,d^0\,\partial_x c^0) &= 0. \end{aligned} \tag{2.59}$$

This means that the surface tension γ plays no role in the effective equations, and therefore the Marangoni effect is lost.

For regimes where $\mathrm{Ca} = \mathcal{O}(\epsilon^\beta)\,\overline{\mathrm{Ca}}$ with $\beta > 0$, the Marangoni effect will play a role in the upscaled models. For example, if $\mathrm{Ca} = \epsilon\,\overline{\mathrm{Ca}}$ with $\overline{\mathrm{Ca}} = \mathcal{O}(1)$, from (2.43), one gets the Marangoni stress boundary condition,

$$\partial_y v^0_{(II,1)} = \frac{\partial_y v^0_{(I,1)}}{M} + \frac{\partial_x \gamma(c^0)}{\overline{\mathrm{Ca}}}, \text{ at } \Gamma^\epsilon(t). \tag{2.60}$$

Using this instead of (2.44) and repeating the same steps in Section 2.4.1.3, one gets for $0 < x < 1$ and $t > 0$,

$$\overline{v}^0_{(I,1)} = -\left(\frac{M(1-d^0)^3}{3} + \frac{d^0\,(1-d^0)\,(2-d^0)}{2}\right)\partial_x p^0 + \frac{(1-d^0)d^0}{\overline{\mathrm{Ca}}}\,\partial_x\gamma(c^0), \tag{2.61}$$

$$\overline{v}^0_{(II,1)} = -\frac{(d^0)^2\,(3-d^0)}{6}\,\partial_x p^0 + \frac{(d^0)^2}{2\,\overline{\mathrm{Ca}}}\,\partial_x\gamma(c^0). \tag{2.62}$$

The upscaled model consists of the mass conservation equations (2.34), (2.36), effective velocities (2.61), (2.62) and the solute transport (2.38). The model can be expressed in terms of three primary variables, the water saturation d^0, the pressure p^0 (recalling that the two fluid pressures are equal) and the concentration c^0. Specifically, for $0 < x < 1$ and $t > 0$ one has

$$\begin{aligned}\partial_t d^0 + \partial_x \left[\left(\frac{M(1-d^0)^3}{3} + \frac{d^0\ (1-d^0)\ (2-d^0)}{2} \right) \partial_x p^0 - \frac{(1-d^0)d^0}{\overline{\mathrm{Ca}}}\ \partial_x \gamma(c^0) \right] &= 0,\\ \partial_t d^0 - \partial_x \left[\left(\frac{(d^0)^2\ (3-d^0)}{6} \right) \partial_x p^0 - \frac{(d^0)^2}{2\ \overline{\mathrm{Ca}}}\ \partial_x \gamma(c^0) \right] &= 0,\\ \partial_t \left(c^0\ d^0 \right) + \partial_x \left[c^0\ \left(\frac{(d^0)^2\ (3-d^0)}{6} \right) \partial_x p^0 \right] - \partial_x (D\ d^0\ \partial_x c^0) &= 0.\end{aligned} \tag{2.63}$$

Assuming $\mathrm{Ca} = \epsilon^\beta\ \overline{\mathrm{Ca}},$ with $\beta = 2$ or 3, will lead to different Marangoni stress conditions than (2.60), involving the unknowns c^1, c^2 etc. In this case one needs to find an effective solute transport equation involving c^1, c^2 etc. This is beyond the scope of this work.

2.4.2 Two-phase flow with constant surface tension

Now, we consider the pore-scale model in Section 2.3.2. We begin with the assumption that $M = \mathcal{O}(1)$. We recall that for a constant surface tension, the dynamic boundary conditions are now (2.25), (2.26).

2.4.2.1 Mass conservation

The derivation of the mass conservation equation in this section is identical to the one in Section 2.4.1.1. The mass conservation equation for the two-phase flow model with constant surface tension are hence (2.34) and (2.36).

2.4.2.2 Momentum conservation

To derive the effective velocities for fluid-I and fluid-II we can follow the same steps discussed in Section 2.4.1.3. Since the surface tension γ is constant, we use the continuity in the tangential component of the normal stress (2.26). It is worth to mention that the capillary number Ca is absent in the tangential stress boundary condition. Applying asymptotic expansion (2.29) in the boundary condition (2.26), we get

$$\frac{1}{\epsilon}\left(\frac{1}{M}\partial_y v^0_{(I,1)} - \partial_y v^0_{(II,1)}\right) + \left(\frac{1}{M}\partial_y v^1_{(I,1)} - \partial_y v^1_{(II,1)}\right) + \mathcal{O}(\epsilon) = 0, \text{at}\, \Gamma^\epsilon(t).$$

The lowest order terms imply

$$\partial_y v^0_{(II,1)} = \frac{1}{M}\,\partial_y v^0_{(I,1)}, \text{ at } \Gamma^\epsilon(t),$$

which is same as (2.44). Further as in Section 2.4.1.3, one obtains the same effective velocities, (2.53) and (2.54).

2.4.2.3 Effect of Ca

Assuming $\mathrm{Ca} = \epsilon^\beta\ \overline{\mathrm{Ca}}$ with $\beta < 3$ and applying asymptotic expansion (2.29) in (2.55) (recalling that here $\gamma(c^\epsilon) = 1$), the lowest order term implies the same pressure relation as in (2.56). The upscaled model for two-phase flow with constant surface tension, large or moderate capillary number can be represented by the mass conservation equations (2.34), (2.36), by the effective velocities (2.58), (2.57) and the pressure relation (2.56). This can be expressed in terms of two primary variables, the water saturation d^0 and the pressure p^0 (recall that the two fluid pressures are equal). Specifically, for $0 < x < 1$ and $t > 0$ one has

$$\begin{aligned} \partial_t d^0 + \partial_x\left[\left(\frac{M(1-d^0)^3}{3} + \frac{d^0\,(1-d^0)\,(2-d^0)}{2}\right)\partial_x p^0\right] = 0,\\ \partial_t d^0 - \partial_x\left[\frac{(d^0)^2\,(3-d^0)}{6}\,\partial_x p^0\right] = 0 \end{aligned} \tag{2.64}$$

If the capillary number is $\mathrm{Ca} = \epsilon^3\ \overline{\mathrm{Ca}}$, applying (2.29) in (2.55), we obtain

$$p^0_{(I)} - p^0_{(II)} = \frac{\partial_{xx} d^0}{\overline{\mathrm{Ca}}}. \tag{2.65}$$

In this case, the upscaled model for the two-phase flow with constant surface tension is given by the mass conservation equations (2.34), (2.36), the effective velocities (2.54), (2.53) and the capillary pressure relationship (2.65).

2.4.2.4 Effect of large viscosity ratio between the fluids

By now we assumed $M = \mathcal{O}(1)$, here we consider $M = \epsilon^{-1}\,\overline{M}$, where $\overline{M} = \mathcal{O}(1)$, which means that the viscosity of fluid-I is much smaller than that of fluid-II. We upscale the equations in Section 2.4.2 and show that the first order terms will only include the fluid-II flow whereas the fluid-I flow component is vanishing when $M \to \infty$. Hence the two-phase flow model reduces to the unsaturated flow model in Section 2.4.3. In this respect we first show that the pressure becomes constant (and is set to 0) for fluid-I. Now, considering $M = \epsilon^{-1}\,\overline{M}$ with $\overline{M} = \mathcal{O}(1)$ in (2.46) and (2.47), for all $t > 0$ one has

$$\partial_x p^0_{(I)} + \epsilon\, \partial_x p^1_{(I)} - \frac{\epsilon}{\overline{M}}\, \partial_{yy} v^0_{(I,1)} + \mathcal{O}(\epsilon^2) = 0, \qquad \text{in } \Omega^\epsilon_{(I)}(t), \tag{2.66}$$

$$\frac{1}{\epsilon}\, \partial_y p^0_{(I)} + \partial_y p^1_{(I)} + \mathcal{O}(\epsilon) = 0, \qquad \text{in } \Omega^\epsilon_{(I)}(t). \tag{2.67}$$

The lowest order terms in (2.66) and (2.67) give

$$\partial_x p^0_{(I)} = 0, \text{ and } \partial_y p^0_{(I)} = 0, \text{ in } \Omega^\epsilon_{(I)}(t).$$

Hence $p^0_{(I)}$ is constant in space. We assume it constant in time as well and set this value to 0, implying

$$p^0_{(I)} = 0, \text{ in } \Omega^\epsilon_{(I)}(t).$$

Considering the surface tension constant in (2.43) and $M = \epsilon^{-1}\,\overline{M}$, where $\overline{M} = \mathcal{O}(1)$, give

$$-\frac{1}{\epsilon}\partial_y v^0_{(II,1)} - \partial_y v^1_{(II,1)} + \frac{1}{\overline{M}}\partial_y v^0_{(I,1)} + \mathcal{O}(\epsilon) = 0, \text{ at } \Gamma^\epsilon(t).$$

The ϵ^{-1} order term in the above equation gives

$$\partial_y v^0_{(II,1)} = 0, \text{ at } \Gamma^\epsilon(t). \tag{2.68}$$

To find the effective velocity for fluid-II we use (2.68) instead of (2.44) when integrating (2.41) in y. Recalling that γ is constant and $p^0_{(I)}$ is zero for fluid-I, we follow the same steps as in Section 2.4.1.3, which results in

$$v^0_{(II,1)} = \partial_x p^0_{(I)} \left(\frac{y^2}{2} + (1 - d^0)\, y + \left(\frac{1}{2} - d^0 \right) \right), \text{ in } \Omega^\epsilon_{(II)}(t). \tag{2.69}$$

Integrating (2.69) and using (2.35) gives the Darcy law

$$\overline{v}^0_{(II,1)} = -\frac{(d^0)^3}{3}\, \partial_x p^0_{(II)}, \text{ for all } 0 < x < 1 \text{ and } t > 0. \tag{2.70}$$

To find the pressure equation for fluid-II, we take $M = \epsilon^{-1}\, \overline{M}$ in Section 2.4.1.4 and we use the fact that the pressure for fluid-I is zero. Then the capillary pressure relation in (2.56) (for $\beta < 3$) changes into

$$p^0_{(II)} = 0, \text{ for all } 0 < x < 1 \text{ and } t > 0. \tag{2.71}$$

Remark. *Since $p^0_{(II)} = 0$ in (2.71), the same holds for $\overline{v}^0_{(II,1)}$ in (2.70) and therefore the saturation is constant in space and time. This is a trivial situation corresponding to steady state.*

Similarly, if $\beta = 3$, (2.65) becomes

$$p^0_{(II)} = -\frac{\partial_{xx} d^0}{\mathrm{Ca}}, \text{ for all } 0 < x < 1 \text{ and } t > 0. \tag{2.72}$$

Note that fluid-I plays no role in the upscaled equations, which now reduce to the equations for fluid-II. Specially, the upscaled model consists of the mass conservation equation (2.36), the effective velocity (2.70) and the pressure equation (2.71) (for $\beta < 3$), respectively by (2.72) (for $\beta = 3$). Hence, in the limit when $M \to \infty$, only the flow of one phase is accounted for the lowest order and the upscaled model for two-phase flow reduces to the upscaled model for the unsaturated flow, as derived in Section 2.4.3.

2.4.3 Unsaturated flow with constant surface tension

We here now turn our attention to the model in Section 2.3.3.

2.4.3.1 Mass conservation

The derivation of the mass conservation equation in this section is identical to the one in Section 2.4.1.1. The mass conservation equation for the unsaturated flow model with constant surface tension is the same as (2.36).

2.4.3.2 Momentum conservation

We apply the asymptotic expansion (2.29) in the boundary condition (2.28) and recall that $v^0_{(II,2)} = 0$ at $\Gamma^\epsilon(t)$, instead of (2.43), the boundary condition for unsaturated flow at $\Gamma^\epsilon(t)$ reduces to

$$-\frac{1}{\epsilon}\,\partial_y v^0_{(II,1)} - \partial_y v^1_{(II,1)} + \mathcal{O}(\epsilon) = 0. \tag{2.73}$$

The ϵ^{-1} order gives

$$\partial_y v^0_{(II,1)} = 0, \text{ at } \Gamma^\epsilon(t),$$

which is same as in (2.68). To find the effective velocity for fluid-II, we follow then the same steps as in Section 2.4.2.4, which results in (2.70), the same effective law for fluid-II as in Section 2.4.2.4.

2.4.3.3 Effects of Ca

In the unsaturated flow case, we disregard fluid-I in (2.55), which leads to

$$\begin{aligned}&-\frac{1}{\epsilon^2}p^\epsilon_{(II)} + \frac{2}{\epsilon}\,\partial_y v^\epsilon_{(II,2)} - (\partial_x d^\epsilon)^2\, p^\epsilon_{(II)} + 2\,\partial_x d^\epsilon\,\partial_y v^\epsilon_{(II,1)} - 2\,\epsilon\,\partial_x d^\epsilon\,\partial_x v^\epsilon_{(II,2)}\\ &-\frac{\epsilon\,\gamma(c^\epsilon)\,\partial_{xx} d^\epsilon}{\mathrm{Ca}} + \mathcal{O}(\epsilon^3) = 0, \text{ at } \Gamma^\epsilon(t).\end{aligned}$$

Applying (2.29) in the above equation and recalling $v^0_{(II,1)} = 0$ at $\Gamma^\epsilon(t)$, we find the same capillary pressure relations as in Section 2.4.2.4. In particular, for $\beta < 3$, we get (2.71) and in this case the upscaled model is trivial (see Section 2.4.2.4). The case Ca$= \epsilon^3\,\overline{\mathrm{Ca}}$ is more interesting as it gives the pressure relation (2.72). The upscaled model in this case is then represented by (2.34), (2.70) and (2.72).

2.5 Summary and discussion of upscaled models

We recall that in the upscaled models the width of the wetting fluid (fluid-II) d^0 can be seen as its saturation and therefore the saturation of the non-wetting fluid (fluid-I) is $(1 - d^0)$. The effective equations on the Darcy scale are now summarized and discussed in the sections below. These models are obtained in the limit situation when $\epsilon \to 0$. Practically, one has ϵ small but not zero. Therefore the upscaled models should be seen as an approximation of the pore-scale models, having a much simpler structure.

Table 2.2: Summary of the upscaled models obtained for different values of β in the capillary number Ca $= \epsilon^\beta$ $\overline{\text{Ca}}$.

β	Marangoni effect	$p^0_{(I)} - p^0_{(II)}$
0	not present	constant
1	present	constant
2	–	constant
3	–	curvature dependent

Assuming $\mathrm{Ca} = \epsilon^\beta \, \overline{\mathrm{Ca}}$, we have considered several regimes identified by the value of β, and derived different upscaled models. Table 2.2 is summarizing these results. Marangoni effects are not visible for $\beta = 0$ but for $\beta = 1$ the Marangoni effects are relevant. For $\beta = 2, 3$ the analysis need further investigated and we leave this as an open questions for the future research. For $\beta < 3$ the phase pressures are equal but for $\beta = 3$ the difference of the phase pressures depends on the second order derivative of the saturation.

2.5.1 Two-phase flow with solute-dependent surface tension

If $\mathrm{Ca} = \mathcal{O}(1)$, then for all $0 < x < 1$ and $t > 0$, the upscaled model for the pore-scale model (2.14)-(2.24) becomes

$$
\begin{aligned}
\partial_t d^0 &= \partial_x \overline{v}^0_{(I,1)}, \\
\partial_t d^0 &= -\,\partial_x \overline{v}^0_{(II,1)}, \\
\overline{v}^0_{(I,1)} &= -\left(\frac{M(1-d^0)^3}{3} + \frac{d^0\,(1-d^0)\,(2-d^0)}{2} \right) \partial_x p^0, \\
\overline{v}^0_{(II,1)} &= -\,\frac{(d^0)^2\,(3-d^0)}{6}\,\partial_x p^0, \\
\partial_t\left(c^0\,d^0\right) &= -\partial_x\left(c^0\,\overline{v}^0_{(II,1)}\right) + \partial_x (D\,d^0\,\partial_x c^0).
\end{aligned} \tag{2.74}
$$

If $\mathrm{Ca} = \epsilon\,\overline{\mathrm{Ca}}$, then for all $0 < x < 1$ and $t > 0$, the upscaled counterpart of the pore-scale model in Section 2.2.2 becomes

$$
\begin{aligned}
\partial_t d^0 &= \partial_x \overline{v}^0_{(I,1)}, \\
\partial_t d^0 &= -\partial_x \overline{v}^0_{(II,1)}, \\
\overline{v}^0_{(I,1)} &= -\left(\frac{M(1-d^0)^3}{3} + \frac{d^0\,(1-d^0)\,(2-d^0)}{2} \right) \partial_x p_0 + \frac{(1-d^0)\,d^0}{\overline{\mathrm{Ca}}}\,\partial_x \gamma(c^0), \\
\overline{v}^0_{(II,1)} &= -\frac{(d^0)^2\,(3-d^0)}{6}\,\partial_x p^0 + \frac{(d^0)^2}{2\,\overline{\mathrm{Ca}}}\,\partial_x \gamma(c^0), \\
\partial_t\left(c^0\,d^0\right) &= -\partial_x\left(c^0\,\overline{v}^0_{(II,1)}\right) + \partial_x (D\,d^0\,\partial_x c^0).
\end{aligned} \tag{2.75}
$$

The upscaled models in (2.74) and (2.75) have a common structure. They include the mass balance for both fluid phases and the Darcy laws for the two fluid velocities. Finally, the last equation gives the mass balance for the solute.

One can recognize the effective velocities in (2.74) and (2.75) as Darcy-type laws for the two fluid phases. Since d^0, respectively $(1 - d^0)$ are the saturation of the two fluids, the factors multiplying the pressure gradients in these equations can be viewed as relative permeabilities of the two fluids. Compared to the effective velocities in (2.74), the influence of the surface tension gradient, namely the Marangoni effect, is visible in the effective velocities in (2.75).

The upscaled models in (2.74) and (2.75) are valid for the regimes where the capillary number is either moderate or large, which corresponds to very small surface tension. Hence the two phase pressures are equal, or, equivalently the capillary pressure is zero, as commonly assumed in petroleum reservoir simulation models [13].

2.5.2 Two-phase flow with constant surface tension

If solute is not present in the fluid-II phase, the surface tension coefficient is constant. In this case the mass balance for solute is left out. Also, no Marangoni effect is encountered, which simplifies the models. Specifically, assuming $\mathrm{Ca} = \epsilon^{\beta}\ \overline{\mathrm{Ca}}$ for $\overline{\mathrm{Ca}} = \mathcal{O}(1)$ and $\beta < 3$, the upscaled counterpart of the pore-scale model in Section 2.2.3 is

$$\begin{aligned}
\partial_t d^0 &= \partial_x \overline{v}^0_{(I,1)}, \\
\partial_t d^0 &= -\partial_x \overline{v}^0_{(II,1)}, \\
\overline{v}^0_{(I,1)} &= -\left(\frac{M(1-d^0)^3}{3} + \frac{d^0\ (1-d^0)\ (2-d^0)}{2}\right) \partial_x p^0, \\
\overline{v}^0_{(II,1)} &= -\frac{(d^0)^2\ (3-d^0)}{6}\ \partial_x p^0,
\end{aligned} \tag{2.76}$$

for all $0 < x < 1$ and $t > 0$. Here the upscaled model is valid in the flow regimes where the capillary number is moderate or large, which again implies that the pressures for the two fluid phases are the same. Assuming, $\mathrm{Ca} = \epsilon^3\ \overline{\mathrm{Ca}}$ with $\overline{\mathrm{Ca}} = \mathcal{O}(1)$, the upscaled model becomes

$$\begin{aligned}
\partial_t d^0 &= \partial_x \overline{v}^0_{(I,1)}, \\
\partial_t d^0 &= -\ \partial_x \overline{v}^0_{(II,1)}, \\
\overline{v}^0_{(I,1)} &= -\left[\frac{M\ (1-d^0)^3}{3} + d^0\ (1-d^0)^2\right] \partial_x p^0_{(I)} - \frac{(1-d^0)\ (d^0)^2}{2}\ \partial_x p^0_{(II)}, \\
\overline{v}^0_{(II,1)} &= -\frac{(d^0)^3}{3}\ \partial_x p^0_{(II)} - \frac{(1-d^0)\ (d^0)^2}{2}\ \partial_x p^0_{(I)}, \\
p^0_{(I)} - p^0_{(II)} &= \frac{\partial_{xx} d^0}{\overline{\mathrm{Ca}}},
\end{aligned} \tag{2.77}$$

for all $0 < x < 1$ and $t > 0$. One can recognize the effective velocities in (2.76) and (2.77) as Darcy-type laws for the two fluid phases. Note that the effective velocities are depending on both pressure gradients from the two fluid phase. A similar case as considered here was also upscaled in [133]. As [133] considered steady-state flow, the phase pressure difference there is different from what we obtained here.

Observe that compared to traditional two-phase flow models, in which the capillary pressure is a function of the saturation, here this involves the second-order derivative of the saturation. Here we emphasize the differences between the regimes $\beta < 3$ and $\beta = 3$ in the capillary pressure relation in (2.76) and (2.77). In the former, the pressures for both fluids are equal, which is similar to saying that the capillary pressure is zero. In the later case, one gets a model in which the commonly used pressure-saturation relation is replaced by a differential equation. Such a model is also derived in [115] and [118] by homogenization techniques. Also, if the upscaled model derived here is reduced to a system of two equations, the capillary pressure relation in (2.77) would lead to a fourth order derivative term which is similar to the ones accounting for surface tension effects, as proposed in [85] for the case of a thin fluid film flowing down a plane, and in [54, 55] for unsaturated, one-phase flow. However, when compared to [54, 55], here a nonlinear, algebraic function of the saturation is absent in the equation for the capillary pressure. This is due to the simple setting adopted here. On the other hand, as in [115, 118] the models are derived by upscaling, whereas in [54, 55] they are formulated directly as upscaled models. One can explain the different results in the two (β-depending) regimes by observing that γ is the reciprocal of Ca. Hence, in the first regime γ is much smaller than in the second one. As in the Young-Laplace equation, the pressure difference is proportional to γ. Whenever this is small, in the upscaled limit one obtains that the two pressure are equal.

2.5.3 Unsaturated flow with constant surface tension

Continuing in the same spirit as before, for the unsaturated case with constant surface tension in Section 2.2.4, the upscaled models are simplified. More precisely, assuming $\mathrm{Ca} = \epsilon^{\beta}\ \overline{\mathrm{Ca}}$ with $\overline{\mathrm{Ca}} = \mathcal{O}(1)$, for $\beta < 3$ the upscaled fluid-II pressure becomes zero (as the one for fluid-I) and therefore the flow is vanishing as well. In this case, the saturation becomes constant in both space and time, which is actually steady state. In this case the upscaled model is trivial. For $\beta = 3$, the upscaled model becomes

$$\begin{aligned} &\partial_t d^0 + \partial_x \overline{v}^0_{(II,1)} = 0, \\ &\overline{v}^0_{(II,1)} + \frac{(d^0)^3}{3}\,\partial_x p^0_{(II)} = 0, \\ &p^0_{(II)} = -\frac{\partial_{xx} d^0}{\overline{\mathrm{Ca}}} \end{aligned} \tag{2.78}$$

for all $0 < x < 1$ and $t > 0$. This can be expressed in terms of one primary variable, the water saturation d^0. Specifically, for all $0 < x < 1$ and $t > 0$, one has

$$\partial_t d^0 + \partial_x \left(\frac{(d^0)^3}{3}\,\frac{\partial_{xxx} d^0}{\overline{\mathrm{Ca}}} \right) = 0, \tag{2.79}$$

This equation resembles the thin-film lubrication approximation [127].

Similar to (2.77), the upscaled model in (2.78) is a non-standard model in the sense that the capillary pressure relation is given by the second derivative of the effective saturation. Also, for a large viscosity ratio, the pore-scale model for the two-phase flow in Section 2.3.2 reduces to the upscaled models in (2.78).

Remark. *The Marangoni effect is only visible for the upscaled model* (2.75)*. For* (2.74)*, the Marangoni effect is lost and one immediately sees that* (2.75) *is equivalent to* (2.74) *for a constant surface tension. Additionally* (2.75) *is equivalent to* (2.76) *for a constant concentration and surface tension. Hence, for the numerical validation in Section 2.6, we will only consider the three upscaled models* (2.75)*,* (2.77) *and* (2.78)*, as these three models represent the different effective behaviours we have considered.*

2.6 Model validation

In this section the upscaled models are validated by numerical experiments. Specifically, the full solutions (e.g. $p^\epsilon_{(\alpha)}, \mathbf{v}^\epsilon_{(\alpha)}, c^\epsilon, d^\epsilon$) of the two-dimensional pore-scale models, computed for pores having different width/length ratios (e.g. $\epsilon = 0.5, 0.3, 0.1, 0.01$), and for different capillary numbers ($\mathrm{Ca} = \epsilon^\beta\ \overline{\mathrm{Ca}}$ with $\overline{\mathrm{Ca}} = \mathcal{O}(1)$, for $\beta = 1, 3$), are averaged in the transversal direction and compared to the approximate upscaled solutions (e.g. $p^0_{(\alpha)}, \mathbf{v}^0_{(\alpha)}, c^0, d^0$).

To compute the full solutions of the pore-scale models, we use COMSOL Multiphysics [1]. For the simulations of the upscaled models, we use a simple finite difference scheme on an equidistant mesh, implemented in MATLAB. First and second order central differences are used for the space discretization. For the time discretization, an explicit method with fixed time-step size is used to avoid the stability issues. In particular, due to the time-explicit approach in (2.75), we have restrictions on the total simulation time. While for (2.77) and (2.78), an implicit method with fixed time-step size is used to avoid the issues with stability when simulating for longer time. We use harmonic averages for the relative permeabilities in the effective flow equations. For the advective flux in (2.75) we use an upwind approximation. We employ Newton's method for solving the resulting non-linear system of equations.

We specify the pore geometry as in (2.12) and (2.13). For (2.12), we define the inflow and outflow boundaries as

$$\begin{aligned}\Gamma^{\epsilon}_{(I,in)}(t) &:= \{(x,y) \in \mathbb{R}^2 | x = 0, -1 + d^{\epsilon}(0,t) < y < 0\},\\ \Gamma^{\epsilon}_{(I,out)}(t) &:= \{(x,y) \in \mathbb{R}^2 | x = 1, -1 + d^{\epsilon}(1,t) < y < 0\}.\end{aligned}$$

For (2.13), the inflow and outflow boundaries are given by

$$\begin{aligned}\Gamma^{\epsilon}_{(II,in)}(t) &:= \{(x,y) \in \mathbb{R}^2 | x = 0, -1 < y < -1 + d^{\epsilon}(0,t)\},\\ \Gamma^{\epsilon}_{(II,out)}(t) &:= \{(x,y) \in \mathbb{R}^2 | x = 1, -1 < y < -1 + d^{\epsilon}(1,t))\}.\end{aligned}$$

In the following, all the presented numerical results are non-dimensional.

2.6.1 Two-phase flow with solute-dependent surface tension

Here we consider a numerical example of the pore-scale model in Section 2.3.1 where the regime is $\mathrm{Ca} = \epsilon\, \overline{\mathrm{Ca}}$ with $\overline{\mathrm{Ca}} = 1$. At the fluid-fluid interface, the surface tension coefficient is chosen as (1.9) with $a = 1$ and $b = 1$, to include the Marangoni effect. The diffusion coefficient is chosen as $D = 1$ and the viscosity ratio as $M = 1$. The initial conditions are

$$d^\epsilon(x,t=0)=0.5,\ \text{at}\ \Gamma^\epsilon(t=0),\ c^\epsilon(x,y,t=0)=0.25,\ \text{in}\ \Omega^\epsilon_{(II)}(t=0),$$
$$\mathbf{v}^\epsilon_{(\alpha)}(x,y,t=0)=\mathbf{0},\ \text{in}\ \Omega^\epsilon_{(\alpha)}(t=0),\quad p^\epsilon_{(\alpha)}(x,y,t=0)=0,\ \text{in}\ \Omega^\epsilon_{(\alpha)}(t=0).$$

The inflow and outflow boundary conditions are

$$p^\epsilon_{(\alpha)}=0.023\ \text{at}\ \Gamma^\epsilon_{(\alpha,in)}(t),\ \text{and}\ p^\epsilon_{(\alpha)}=0\ \text{at}\ \Gamma^\epsilon_{(\alpha,out)}(t),$$
$$c^\epsilon=1\ \text{at}\ \Gamma^\epsilon_{(II,in)}(t),\ \text{and}\ c^\epsilon=0.25\ \text{at}\ \Gamma^\epsilon_{II,out}(t).$$

Compatible initial and boundary conditions are chosen by recalling the capillary pressure relation (2.56). To solve the upscaled model (2.75), the same initial and boundary conditions are chosen. We use homogeneous Neumann boundary conditions for d^0 at $x=0$ and $x=1$. The models are solved for a total time of $t=0.1$.

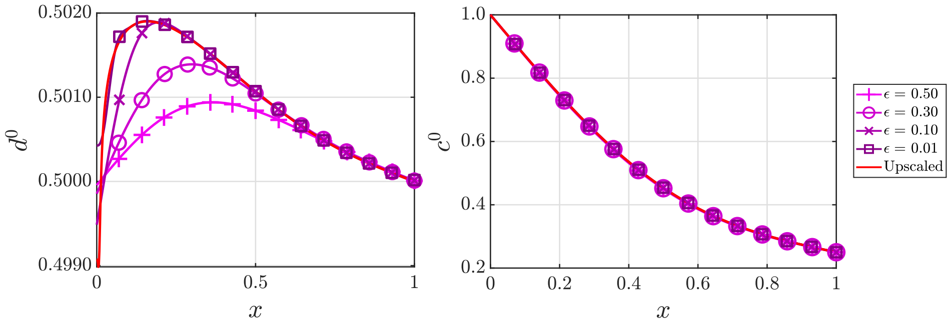

Figure 2.3: Comparison of the saturation (left) and the concentration (right) of the upscaled model with the transversally averaged solutions of the pore-scale model for different ϵ at $t=0.1$.

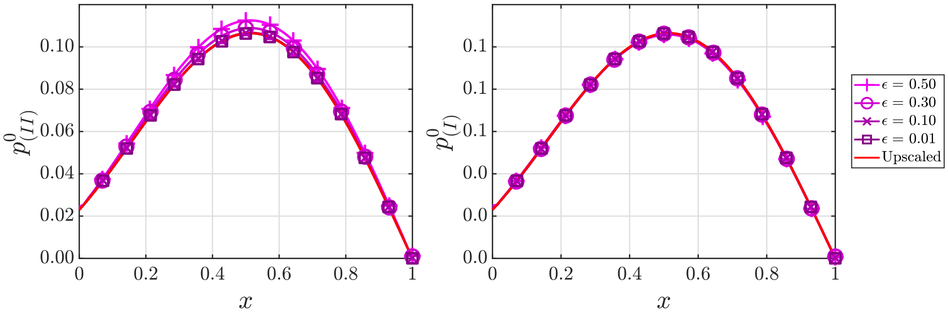

Figure 2.4: Comparison of the pressures of the wetting (left) and the non-wetting fluid (right) of the upscaled model with the transversally averaged solutions of the pore-scale model for different ϵ at $t = 0.1$.

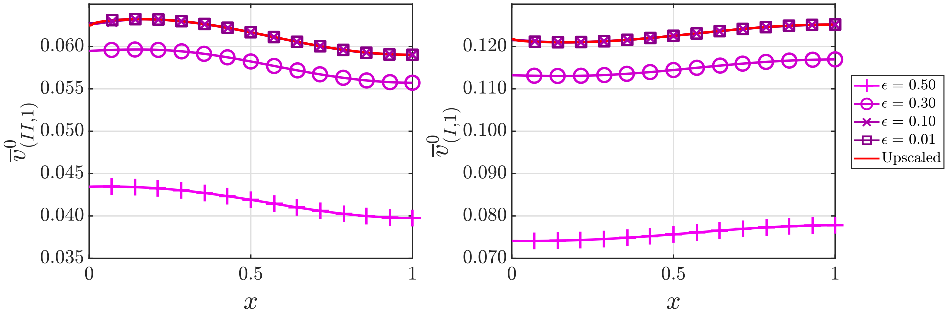

Figure 2.5: Comparison of the fluxes of the wetting (left) and the non-wetting fluid (right) of the upscaled model with transversally averaged solutions of the pore-scale model for different ϵ at $t = 0.1$.

In Figure 2.3-Figure 2.5, we have plotted the upscaled solutions of (2.75) together with the transversally averaged pore-scale solutions in Section 2.3.1 for four different ϵ. For decreasing ϵ, the averaged pore-scale solutions are closer to the upscaled ones, which we also observe in Figure 2.6. Note that we can not decide any convergence order for the L^2-errors in Figure 2.6. The numerical errors are influencing the results, especially for the COMSOL simulations, which are difficult to estimate. Moreover, we observe only weakly decreasing L^2-error from $\epsilon = 0.1$ to $\epsilon = 0.01$, likely due to numerical errors dominating. To analyze the order of convergence, one can use the concept of two-scale convergence (see [5]), which is beyond the scope of this thesis.

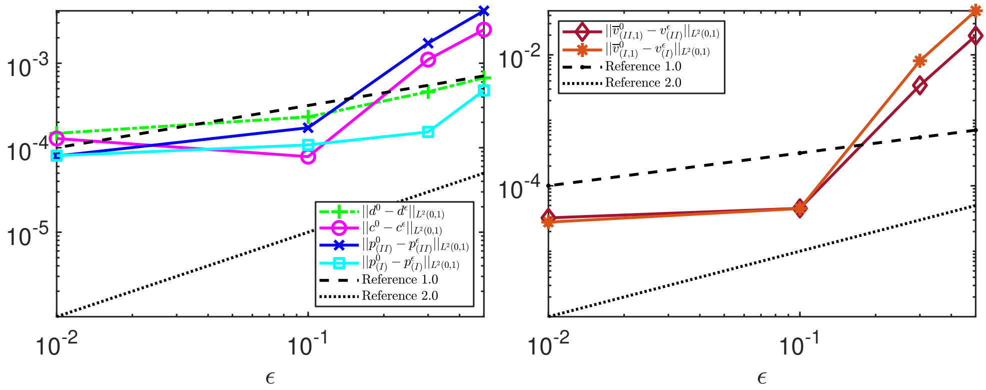

Figure 2.6: The L^2-norm of the difference between the upscaled quantities and the corresponding transversally averaged solutions of the pore-scale model for different ϵ at $t = 0.1$.

2.6.2 Two-phase flow with constant surface tension

Here we consider a numerical example of the pore-scale model in Section 2.3.2 where the regime is $\mathrm{Ca} = \epsilon^3\,\overline{\mathrm{Ca}}$ with $\overline{\mathrm{Ca}} = 1$. The viscosity ratio is chosen as $M = 1$. The initial conditions are

$$p^\epsilon_{(\alpha)}(x, y, t = 0) = 0, \text{ in } \Omega^\epsilon_{(\alpha)}(t = 0), \mathbf{v}^\epsilon_{(\alpha)}(x, y, t = 0) = \mathbf{0}, \text{ in } \Omega^\epsilon_{(\alpha)}(t = 0),$$
$$d^\epsilon(x, t = 0) = 0.5 - 1.2x + 1.2x^2, \text{ at } \Gamma^\epsilon(t = 0).$$

The inflow and outflow boundary conditions are

$$p^\epsilon_{(I)} = 0.023, \text{ at } \Gamma^\epsilon_{(I,in)}(t), \text{ and } p^\epsilon_{(I)} = 0 \text{ at } \Gamma^\epsilon_{(I,out)}(t),$$
$$p^\epsilon_{(II)} = -2.377, \text{ at } \Gamma^\epsilon_{(II,in)}(t), \text{ and } p^\epsilon_{(II)} = -2.4, \text{ at } \Gamma^\epsilon_{II,out}(t).$$

To avoid a non-smooth behaviour of the fluids, the values chosen above ensure that the initial and the boundary conditions are compatible. Moreover, the capillary pressure relation (2.65) is also satisfied for $t = 0$. To solve the upscaled model (2.77), the same initial and boundary conditions are chosen. We use homogeneous Neumann boundary conditions for d^0 at $x = 0$ and $x = 1$. The models are solved for a total time of $t = 1$.

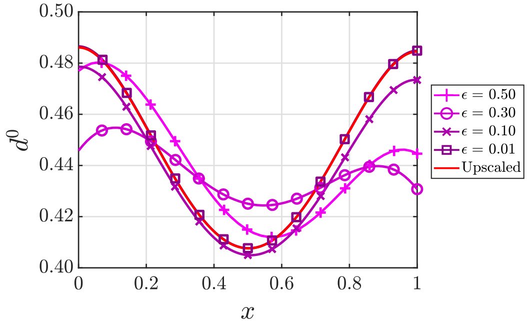

Figure 2.7: Comparison of the saturation of the wetting fluid of the upscaled model with transversally averaged solutions of the pore-scale model for different ϵ at $t = 1$.

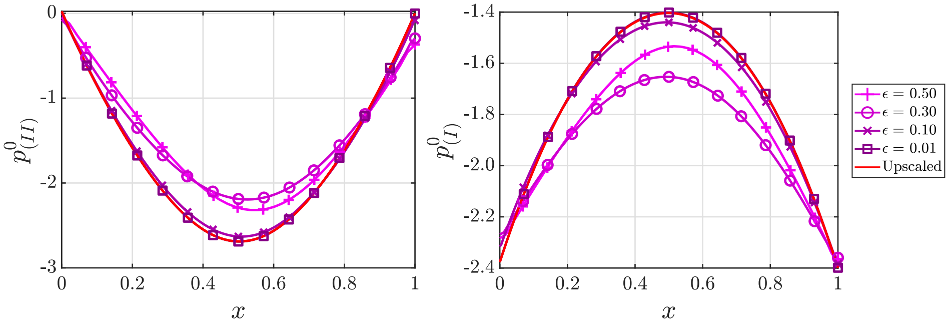

Figure 2.8: Comparison of the pressures of the wetting (left) and the non-wetting fluid (right) of the upscaled model with transversally averaged solutions of the pore-scale model for different ϵ at $t = 1$.

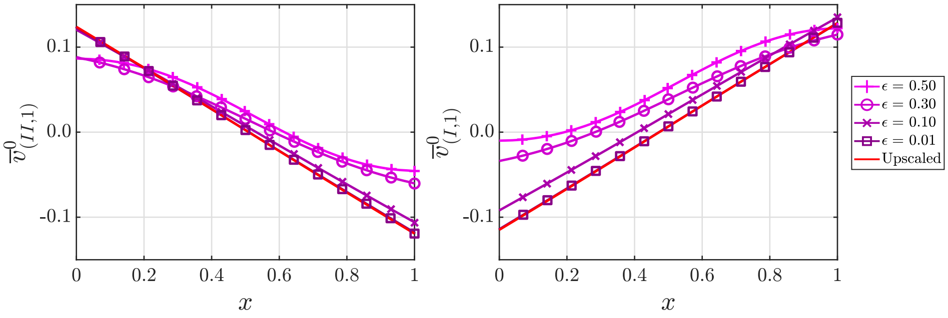

Figure 2.9: Comparison of the fluxes of the wetting (left) and the non-wetting fluid (right) of the upscaled model with transversally averaged solutions of the pore-scale model for different ϵ at $t = 1$.

In Figure 2.7 - Figure 2.9, we have plotted the upscaled solutions of (2.77) together with the averaged pore-scale solutions in Section 2.3.2 for various ϵ at $t = 1$. For decreasing ϵ, the averaged pore-scale solutions are closer to the upscaled solutions, which we also see in Figure 2.10. Here we can not also decide any convergence order for the L^2-errors in Figure 2.10, but the errors are generally decreasing for decreasing ϵ.

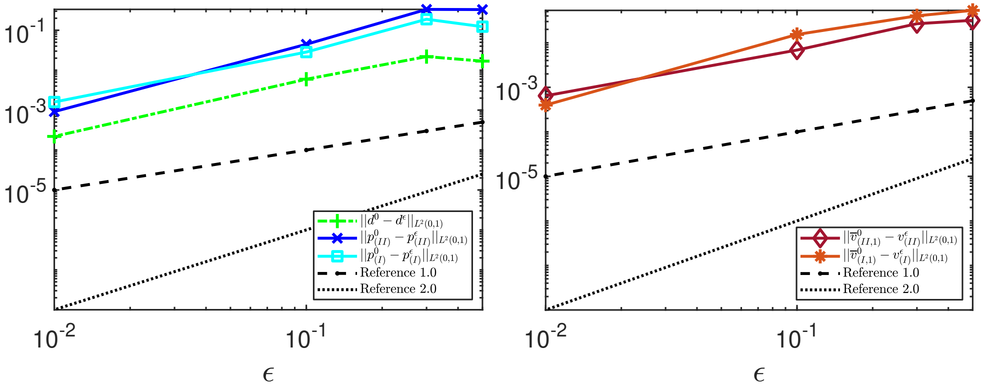

Figure 2.10: L^2-norm of the difference between the upscaled quantities and the corresponding transversally averaged solutions of the pore-scale model for different ϵ at $t = 1$.

2.6.3 Unsaturated flow with constant surface tension

The numerical computations of the pore-scale model in Section 2.3.3 are considered for the regime in $\mathrm{Ca} = \epsilon^3\, \overline{\mathrm{Ca}}$ with $\overline{\mathrm{Ca}} = \mathcal{O}(1)$. The initial conditions are

$$d^\epsilon(x, t=0) = 0.5 \text{ at } \Gamma^\epsilon(t=0),\ \mathbf{v}^\epsilon_{(II)}(x, y, t=0) = \mathbf{0}$$
$$\text{and } p^\epsilon_{(II)}(x, y, t=0) = 0 \text{ in } \Omega^\epsilon_{(II)}(t=0).$$

The inflow and outflow boundary conditions are

$$p^\epsilon_{(II)} = 0.023 \text{ at } \Gamma^\epsilon_{(II,in)}(t) \text{ and } p^\epsilon_{(II)} = 0 \text{ at } \Gamma^\epsilon_{II,out}(t).$$

The initial conditions and the boundary conditions are same as for the pore-scale model. We use homogeneous Neumann boundary conditions for d^0 at $x = 0$ and $x = 1$. The models are solved for a total time of $t = 1$.

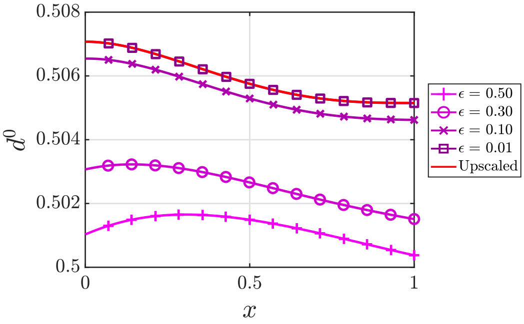

Figure 2.11: Comparison of the saturation of the wetting fluid of the upscaled model with the transversally averaged solutions of the pore-scale model for different ϵ at time $t = 1$.

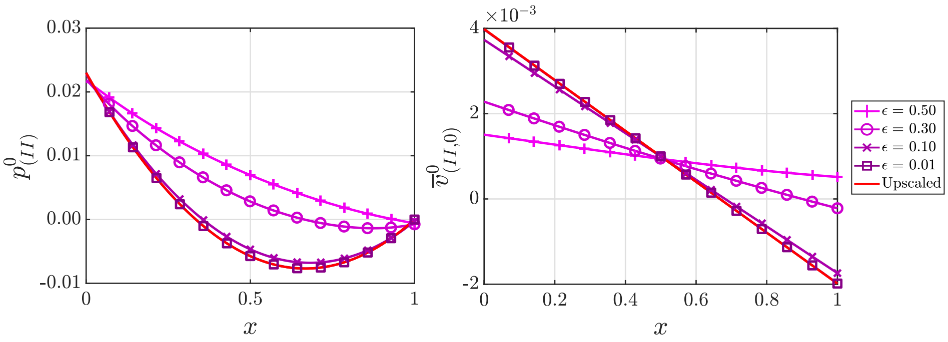

Figure 2.12: Comparison of the pressure (left) and the flux (right) of the wetting fluid of the upscaled model with the transversally averaged solutions of the pore-scale model for different ϵ at time $t = 1$.

In Figure 2.11 and Figure 2.12, we have plotted the upscaled solutions of (2.78) together with the averaged pore-scale solutions in Section 2.3.3 for various ϵ at $t = 1$. For decreasing ϵ, the averaged pore-scale solutions are closer to the upscaled solutions, which we also see in Figure 2.13. As before, we can not deduce an order of convergence.

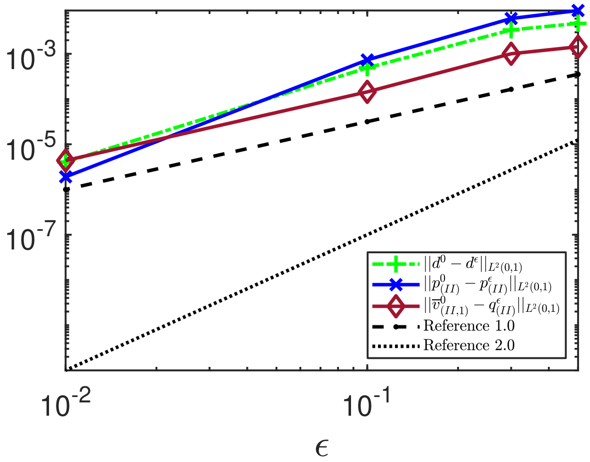

Figure 2.13: L^2-norm of the difference between the upscaled quantities and the corresponding transversally averaged solutions of the pore-scale model for different ϵ at $t = 1$.

2.7 Model comparison

In Section 2.5, we have summarized all the upscaled models derived for different capillary regimes. The goal of this section is to numerically compare the upscaled models valid in the same capillary regime. The upscaled model (2.75) includes the Marangoni effect which reduces to the upscaled model (2.76) of the two-phase flow model when the surface tension is constant or when the concentration of the solute is equally distributed. On the other hand when $M \to \infty$ the upscaled model (2.77) of the two-phase flow reduces to the unsaturated flow upscaled model (2.78). For this comparison we solve (2.77) for increasing values of M and then compare with (2.78).

2.7.1 Comparison of Marangoni flow and two-phase flow

Here we compare between the upscaled models in (2.75) and (2.76) where the regime is $\mathrm{Ca} = \epsilon\, \overline{\mathrm{Ca}}$ with $\overline{\mathrm{Ca}} = 1$. The initial conditions are, for $0 < x < 1$,

$$\begin{aligned} &d^0(x,0) = 0.5,\ c^0(x,0) = 0.50,\\ &\overline{q}^{(1)}_{\alpha,0}(x,0) = 0, \quad p_{\alpha,0}(x,0) = p^0(x,0) = 0. \end{aligned}$$

The inflow and outflow boundary conditions for the pressures are

$$p_{\alpha,0}(0,t) = 0.023,\ \text{and}\ p_{\alpha,0}(1,t) = 0.$$

Depending on the inflow boundary conditions for the concentration, we have tested three different cases to observe the Marangoni flow. Here the outflow boundary condition is set to the same value as the initial concentration. The three different cases are

$$\begin{aligned} &\text{case(i):} && c^0(0,t) = 0.25,\ \text{and}\ c^0(1,t) = 0.50,\\ &\text{case(ii):} && c^0(0,t) = 0.50,\ \text{and}\ c^0(1,t) = 0.50,\\ &\text{case(iii):} && c^0(0,t) = 1.00,\ \text{and}\ c^0(1,t) = 0.50. \end{aligned}$$

At the fluid-fluid interface, the surface tension coefficient is chosen as (1.9) with $a = 1$ and $b = 1$ to include the Marangoni effect. The diffusion coefficient is chosen as $D = 1$

and the viscosity ratio as $M = 1$. The models are solved for a total time of $t = 0.1$.

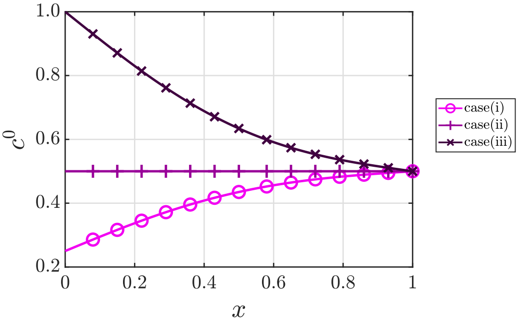

Figure 2.14: Comparison of the concentration of the upscaled model (2.75) for the Marangoni flow for different test cases at $t = 0.1$.

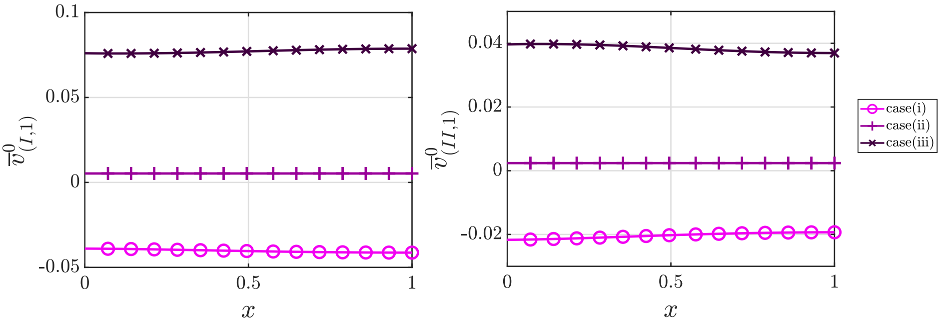

Figure 2.15: Comparison of the fluxes of the non-wetting (left) and the wetting fluid (right) of the upscaled model (2.75) for the Marangoni flow for different test cases at $t = 0.1$.

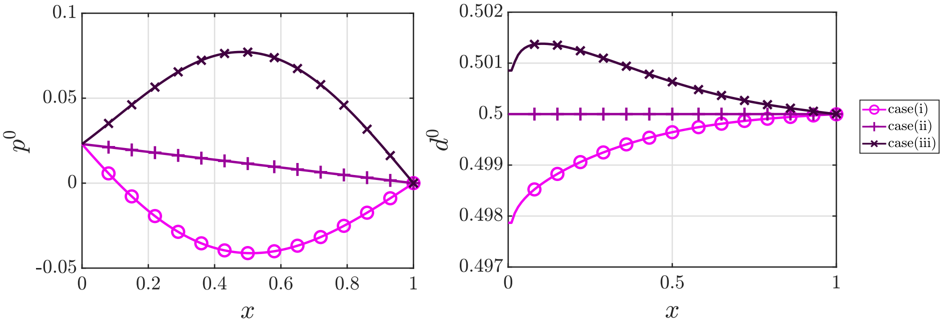

Figure 2.16: Comparison of the pressure (left) and the saturation (right) of the upscaled model (2.75) for the Marangoni flow for different test cases at $t = 0.1$.

We see in Figure 2.14 that case(ii) corresponds to a constant concentration and thus $\partial_x \gamma(c^0) = 0$. We want to emphasize that this is equivalent to the case of solving the upscaled model (2.76) for the two-phase flow with constant surface tension. This case will hence not include Marangoni effect. Due to the difference in inlet and outlet pressure, both fluid velocities are small but positive through the domain, accompanied by a linear pressure drop and a constant saturation as seen in Figure 2.15 and Figure 2.16.

For case(i) we see in Figure 2.14 that this corresponds to $\partial_x c^0 > 0$, which implies $\partial_x \gamma(c^0) < 0$. Oppositely, case(iii) corresponds to $\partial_x \gamma(c^0) > 0$. The effect on the fluid velocities, pressures and saturations in Figure 2.15 and Figure 2.16 is evident. For case(i) we see how the negative surface tension gradient along the strip results in overall negative velocities of both fluids through the strip. This is as expected from the Darcy-type laws in (2.75), and can be interpreted as the flow going towards the lower concentration of solute and hence towards the region of larger surface tension. In particular we see how the pressure distribution through the strip adjusts and hence is a convex function in case(i). Also, the saturation becomes slightly decreased near the inlet, which is due to the difference in response of the two fluid velocities. The opposite behaviour is seen for case(iii). Here the negative solute concentration gradient, corresponding to a positive surface tension gradient, gives an increased flow in the positive direction through the strip. The pressure becomes concave, while the saturation near the inlet is seen to increase slightly due to the difference in fluid velocity.

This simple test case shows how the Marangoni effect can alter the flow and mass transfer through a pore due to processes at the fluid-fluid interface. We see how the flow is adjusted to be towards the region of larger surface tension, as is expected for Marangoni flow.

2.7.2 Comparison of two-phase flow and unsaturated flow

Here we compare between the upscaled models in (2.77) and (2.78) where the regime is $\mathrm{Ca} = \epsilon^3\ \overline{\mathrm{Ca}}$ with $\overline{\mathrm{Ca}} = 1$. The viscosity ratio is chosen as $M = 1, M = 10, M = 100$ and $M = 1000$ in (2.77) and compared to (2.78) which corresponds to letting $M \to \infty$. The initial conditions are, for $0 < x < 1$

$$d^0(x,0) = 0.5 - 1.2\,x + 1.2\,x^2,\ \overline{q}^{(1)}_{\alpha,0}(x,0) = 0,\ p_{\alpha,0}(x,0) = 0.$$

The inflow and outflow boundary conditions are

$$\begin{aligned} &p^0_{(I)}(0,t) = 0.023,\ \text{and}\ p^0_{(I)}(1,t) = 0,\\ &p^0_{(II)}(0,t) = -2.377,\ \text{and}\ p^0_{(II)}(1,t) = -2.4. \end{aligned}$$

The models are solved for a total time of $t = 1$.

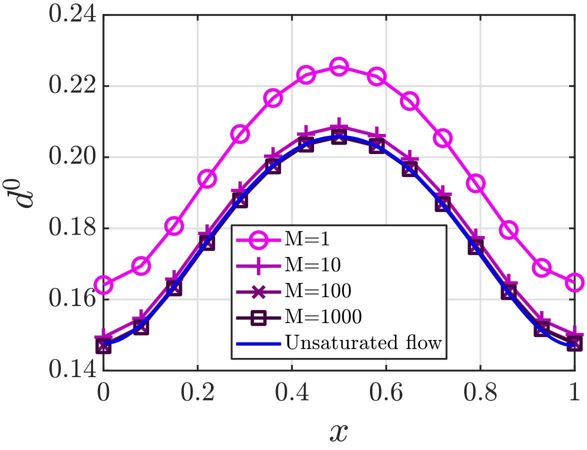

Figure 2.17: Comparison of the saturation of the wetting fluid of the upscaled models at $t = 1$.

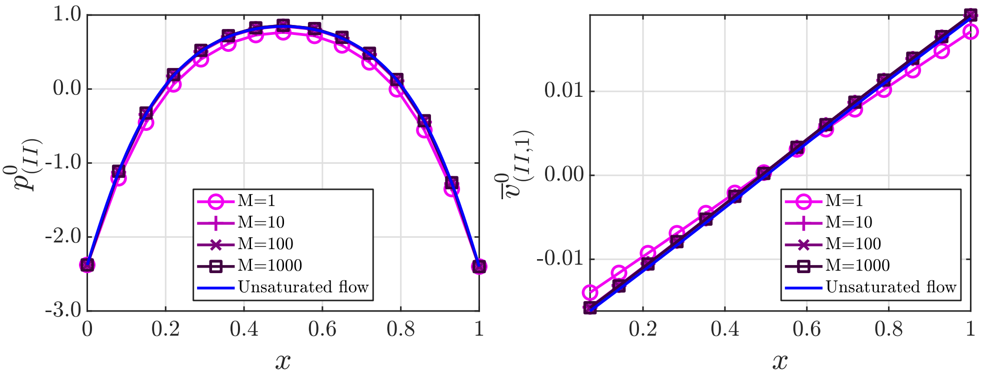

Figure 2.18: Comparison of the pressure (left) and the flux (right) of the wetting fluid of the upscaled models at $t = 1$.

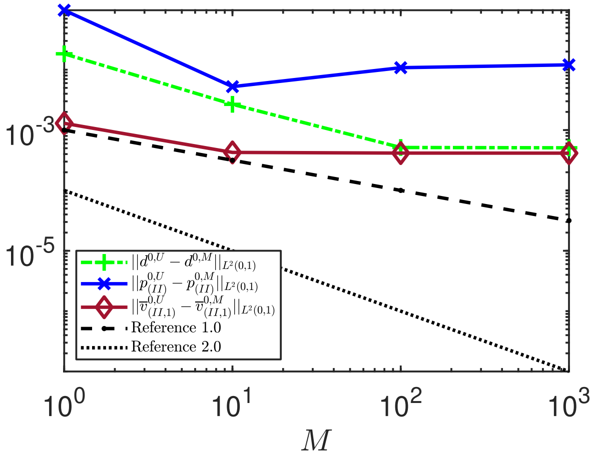

Figure 2.19: L^2-norm of the difference between the wetting phase quantities $(d^{0,U}, p^{0,U}_{(II)}, \overline{v}^{0,U}_{(II,1)})$ in the unsaturated flow model and the corresponding ones for the two-phase flow $(d^{0,M}, p^{0,M}_{(II)}, \overline{v}^{0,M}_{(II,1)})$, for different values of M at $t = 1$.

Figure 2.17 and Figure 2.18 show that the upscaled wetting phase quantities in the two-phase flow model are approaching the corresponding one in the unsaturated flow model as the viscosity ratio is increasing. In Figure 2.19, we present the L^2-norm of the difference between the wetting phase quantities in the unsaturated flow model and the corresponding ones for the two-phase flow, for different values of M at $t = 1$. Observe that the differences become smaller for larger viscosity ratios. We see that the behaviour of the wetting fluid is well approximated by the simpler unsaturated-flow model already for $M = 10$. But the differences are not decreasing from $M = 10$ to $M = 1000$, most likely caused by numerical errors starting to dominate. Hence, if the velocity and saturation of the wetting fluid is of main interest, one could use the unsaturated-flow model instead of the two-phase flow model already for relatively moderate viscosity ratios.

2.8 Conclusion

We consider the flow of two immiscible and incompressible phases, respectively the unsaturated flow in a thin strip representing a porous medium. We account for the possible dependence of the surface tension on the solute transported by the wetting fluid. For the two-phase flow the starting point is the model at the pore scale, where the two fluids are separated by an interface having an a-priori unknown location but depending on the fluid velocities. The flow is described by the Navier-Stokes equations and the solute transport by the advection-diffusion equation. At the interface separating the two fluids, relevant interface conditions are imposed. In particular, the difference in the normal stress tensors depend on the surface tension, which may change depending on the solute concentration. Considering a simplified situation, namely a thin strip representing a single pore, we have derived upscaled one-dimensional models describing the averaged behaviour of the system for different capillary regimes. We have validated our theoretical results with numerical experiments and we then compared the behaviour of the upscaled models. In doing so, different situations are considered, in which the capillary number and the viscosity ratio have a certain behaviour w.r.t. the ratio of the pore width and length. In particular, we see that the solute-dependent surface tension (the Marangoni effect) is relevant for the upscaled models only if the capillary number is small enough. In the case when the viscosity ratio becomes large, the two-phase flow model reduces to the unsaturated model. One main conclusion is that for small capillary numbers instead of capillary pressure - saturation curve, we obtain capillary pressure - saturation dependency involving the second order derivative of the saturation, as also proposed in [54, 55, 115, 118]. Based on the numerical results, we emphasize that the presence of solute-dependent surface tension can strongly influence the flow.

Although considering a simple geometry, combining asymptotic expansions with various scaling of the non-dimensional parameters show which processes are important at the larger scale and which can be neglected. The upscaling procedure also shows how the capillary pressure depends on the saturation when the capillary pressure should be accounted for. Allowing for other types of fluid displacement, such as a fluid-fluid-solid contact point, and more general geometries open for also other types of upscaled models.

Chapter 3

Periodic homogenization of two-phase flow problems

This chapter is based on the following two publications [17, 161]:

- "S. Sharmin, M. Bastidas, C. Bringedal, I.S. Pop, Upscaling a Navier-Stokes-Cahn-Hilliard model for two-phase porous-media flow with solute-dependent surface tension effects, Applicable Analysis, 101 (2022),pp. 1-23, https://doi.org/10.1080/00036811.2022.2052858."
- "M. Bastidas, S. Sharmin, C. Bringedal, I.S. Pop, A numerical scheme for two-scale phase-field models in porous media, Book of Extended Abstracts of the 6th ECCOMAS Young Investigators Conference, Universitat Politècnica de València, Spain, https://doi.org/10.4995/YIC2021.2021.12571."

3.1 Introduction

In this chapter, we consider the flow of two immiscible fluid phases in a porous medium, in which surfactant-dependent surface-tension effects are taken into account. More specifically, at the pore scale, the surface tension depends on the concentration of the surfactant, which is soluble in one of the fluid phases. At the pore scale, one encounters an interface separating the two fluids transported by the flow. The fluid-fluid interfaces appear as free boundaries at the pore scale.

In contrast to the sharp-interface approach used in Chapter 2, we consider here a diffuse-interface approach to handle the free-boundary problem. In the phase-field approach, one works with a mixture of both fluids. We briefly discussed the challenges and necessity of this approach for modeling more realistic situations in Section 1.1.1.1.

The starting point is a Cahn-Hiliard [47] approximation of the phase separation together with the Navier-Stokes equations for the flow of the two fluids. Such models have been considered in [2,51,69]. Alternatively, in [19,57,154] the pore-scale flow is described by the Stokes model. We prefer to use the Navier-Stokes equation for capturing fully the physics of the two-phase fluid flow at the pore scale. We highlight that a thermodynamically consistent phase-field model for two-phase flow was first derived in [2], and later, two-phase flow models with surfactants were considered in [69]. Our model builds upon the model B derived in [69], where two-phase flow with variable surface tension is considered and the phase-field approach within a free energy framework is used to model the phase separation. We consider the instantaneous adsorption regime in [69], and simplify the model by assuming that the surfactant is only present in one of the fluid phases. Concerning numerical methods for similar type of models as discussed here, we refer to [189], where energy-stable schemes are proposed for a Cahn-Hiliard model for two-phase flow and surfactant transport, and to [66, 147], where energy-stable methods based on discontinuous Galerkin discretization are analyzed.

To handle the complexity of the pore-scale domain, we consider a periodically perforated domain. We recall that in practical applications, the main interest is in the system behavior at the Darcy scale, not necessarily in the complex, pore-scale behavior. We employ here formal homogenization techniques for the derivation of the two-scale two-phase flow model, accounting for the surface-tension effects. More precisely, we use formal asymptotic expansion methods and assume local periodicity at the pore scale. In the resulting two-scale model, the effective (Darcy-scale) parameters required at the Darcy scale are determined by solving pore-scale cell problems, which, in their turn, depend on the Darcy-scale quantities. For similar results, we refer to [19, 42, 57, 113] where no surfactant is present in the model, and to [154], where a solute transport component is included in the model, but without affecting the surface tension.

This chapter is organized as follows. In Section 3.2, we present the Cahn-Hillard-Navier-Stokes two-phase flow model with solute-dependent surface tension and give the sharp-interface limit of the phase-field model. In Section 3.3, we derive the upscaled model from the non-dimensional pore-scale phase-field model using the asymptotic expansion method. In Section 3.4, we present the numerical scheme for solving the two-scale model and then solve this model for some test cases in Section 3.5. Finally, in Section 3.6, we draw our conclusions and give some remarks for future research.

3.2 The pore-scale model

Here we discuss the pore-scale model for the two-phase flow in a porous medium. The fluids are assumed incompressible and immiscible. For each fluid phase, the flow is governed by the Navier-Stokes model, defined in the corresponding sub-domain, and with fluid-specific parameters. As mentioned before, to overcome the difficulties related to the free boundaries, we use the phase-field approximation developed in [69]. The evolution of the phase field is given by the Cahn-Hilliard equation.

In what follows, we let $\Omega_{\mathcal{P}}$ be the domain which can be occupied by the two fluids and denote its boundary by $\partial\Omega_{\mathcal{P}}$.

3.2.1 The sharp-interface model

In the sharp-interface model, one has two different fluid phases, indexed by $\mathtt{i}(\mathtt{i} = 1, 2)$. We let $\rho^{(\mathtt{i})}, \mu^{(\mathtt{i})}, \mathbf{v}^{(\mathtt{i})}, p^{(\mathtt{i})}(\mathtt{i} = 1, 2)$ stand for the (constant) mass density, (constant) viscosity, velocity and pressure of fluid $\mathtt{i}$. Moreover, these quantities are defined in the time-dependent subdomains $\Omega_{\mathcal{P}}^{(\mathtt{i})}(t)$, which correspond to the parts of $\Omega_{\mathcal{P}}$ occupied by fluid $\mathtt{i}$. More precisely, the flow equations for fluid $\mathtt{i}$ read

$$\partial_t \left(\rho^{(\mathtt{i})}\mathbf{v}^{(\mathtt{i})}\right) + \nabla \cdot \left(\rho^{(\mathtt{i})}\mathbf{v}^{(\mathtt{i})} \otimes \mathbf{v}^{(\mathtt{i})}\right) - \nabla \cdot \left(-p^{(\mathtt{i})}\mathbf{I} + 2\mu^{(\mathtt{i})}\mathcal{E}(\mathbf{v}^{(\mathtt{i})})\right) = 0, \tag{3.1a}$$

$$\nabla \cdot \mathbf{v}^{(\mathtt{i})} = 0, \tag{3.1b}$$

for $t > 0$ and $\mathbf{x} \in \Omega_{\mathcal{P}}^{(\mathtt{i})}(t)$. Here $\mathcal{E}(\mathbf{v}^{(\mathtt{i})}) := \frac{1}{2}\left(\left(\nabla \mathbf{v}^{(\mathtt{i})}\right) + \left(\nabla \mathbf{v}^{(\mathtt{i})}\right)^T\right)$ is the symmetric stress tensor and $\mathbf{I}$ is the identity matrix.

For the surfactant concentration c, soluble only in fluid 1, we have

$$\partial_t c + \nabla \cdot \left(\mathbf{v}^{(1)} c\right) = \nabla \cdot (D \nabla c), \quad \text{in } \Omega_{\mathcal{P}}^{(1)}(t), \text{ for } t > 0, \tag{3.1c}$$

where $D > 0$ denotes the diffusion coefficient.

The fluid-fluid interface $\Gamma(t)$ is a free boundary, whose evolution is determined by the fluid velocities and the solute-dependent surface tension $\gamma(c)$. Several adsorption isotherms are proposed in [69], stating the relationship between surface tension and the surface concentration of the solute. To relate the volume and surface concentrations, we follow the ideas in [69] and define the isotherm in terms of the product βc, where β is a length and c a volume concentration. In this way, βc is to be understood as the surface concentration. We assume that $\gamma(c)$ is linearly decreasing, namely the Henry isotherm (see [69])

$$\gamma(c) = \gamma_0 - B\beta c. \tag{3.1d}$$

Here γ_0 is the surface tension of a clean interface and B is the sensitivity of the surface tension to the surfactant. For any $t > 0$, at $\Gamma(t)$, one has

$$\left[\mathbf{v}^{(\mathtt{i})}\right] = 0, \tag{3.1e}$$

$$\mathbf{v}^{(\mathtt{i})} \cdot \mathbf{n} = v_n, \tag{3.1f}$$

$$\left[-p^{(\mathtt{i})}\mathbf{I} + 2\mu^{(\mathtt{i})}\, \mathcal{E}(\mathbf{v}^{(\mathtt{i})})\right] \mathbf{n} = \gamma(c)\kappa \mathbf{n} - \nabla_{\mathbf{t}}\gamma(c), \tag{3.1g}$$

$$\left(-D\nabla c + \mathbf{v}^{(1)} c\right) \cdot \mathbf{n} = v_n\, c. \tag{3.1h}$$

Here $[.]$ stands for the jump of the quantities from $\Omega_{\mathcal{P}}^{(1)}(t)$ to $\Omega_{\mathcal{P}}^{(2)}(t)$, κ is the mean curvature of $\Gamma(t)$ and v_n its normal velocity. Moreover, $\nabla_{\mathbf{t}}\gamma(c) := \nabla\gamma(c) - \mathbf{n}\,(\mathbf{n} \cdot \nabla\gamma(c))$ is the tangential stress gradient, where $\mathbf{n}$ is the unit normal vector on $\Gamma(t)$ pointing into $\Omega_{\mathcal{P}}^{(1)}(t)$ from $\Omega_{\mathcal{P}}^{(2)}(t)$.

Note that the jump condition in (3.1g) has two components. In the direction normal to $\Gamma(t)$, the jump in the normal stress equals to $\gamma(c)\kappa$. In the tangential direction, the normal stress is given by the tangential component of $\nabla\gamma(c)$, multiplied by (-1). In case of a constant surface tension, the tangential component vanishes. Finally since no solute is present in fluid 2, (3.1h) expreses the conservation of solute across $\Gamma(t)$.

3.2.2 The phase-field model

In the phase-field model, the interface separating the two immiscible fluids is approximated by a diffuse interface. We consider the time interval $[0, \infty)$, and let $Q = (0, \infty) \times \Omega_{\mathcal{P}}$. A phase indicator $\phi : Q \to \mathbb{R}$ accounts for the presence of the two fluids, taking values either close to 1 in points occupied mainly by fluid 1 or close to -1 in points occupied mainly by fluid 2. Following [2, 69] the energy of the fluid-fluid interface is approximated by the Ginzburg-Landau energy functional

$$e_{\text{free}}(\phi, \nabla\phi) = \mathcal{C}\left(\frac{1}{\lambda}P(\phi) + \frac{\lambda}{2}|\nabla\phi|^2\right), \tag{3.2}$$

where $\lambda > 0$ is the thickness of the diffuse interfacial region, $\mathcal{C} = \frac{3}{2\sqrt{2}}$ is a calibration constant, while $P : \mathbb{R} \to \mathbb{R}$ is the double-well potential defined as

$$P(\phi) = \frac{1}{4}(1 - \phi^2)^2. \tag{3.3}$$

3.2.2.1 The Cahn-Hilliard equations

To describe the evolution of the phase field, we use the Cahn-Hilliard equation, written in mixed form as two coupled second order equations. First,

$$\partial_t\phi + \nabla \cdot (\mathbf{v}\phi) = m\ \lambda\ \Delta\psi, \text{ in } Q, \tag{3.4a}$$

where $\mathbf{v}$ is the velocity of the mixture and ψ is the potential. The Cahn-Hilliard mobility $m > 0$ is assumed here constant. Alternative choices for m are discussed in [2], leading to various sharp-interface models in the limit $\lambda \to 0$. Second, following Model B in [69], which corresponds to instantaneous adsorption, and using (3.1d), one obtains

$$\psi = -\nabla \cdot (\mathcal{C}\lambda\gamma(c)\nabla\phi) + \frac{\mathcal{C}}{\lambda}\gamma(c)P'(\phi) + \frac{1}{\beta}\gamma(c)I'(\phi), \text{ in } Q, \tag{3.4b}$$

where $I : \mathbb{R} \to \mathbb{R}$ is defined as

$$I(\phi) = \frac{1}{2}(1 + \phi). \tag{3.4c}$$

As shown in [69], when $\lambda \to 0$, the phase field ϕ approaches the sign graph and therefore $I(\phi)$ approaches the characteristic function of fluid 1. Note the last term in (3.4b), which is added to include the effect of the varying surface tension.

We assume homogeneous Neumann boundary conditions for the phase field ϕ, as well as for the chemical potential ψ

$$\nabla\phi \cdot \mathbf{n} = 0, \text{ and } \nabla\psi \cdot \mathbf{n} = 0, \text{ on } \partial\Omega_{\mathcal{P}}, \text{ for } t > 0, \tag{3.4d}$$

where $\mathbf{n}$ is the unit normal to $\partial\Omega_{\mathcal{P}}$ pointing out of $\Omega_{\mathcal{P}}$. The first boundary condition corresponds to a 90° contact angle, and the second is needed for conserving the mass of the phase field.

The Cahn-Hilliard equations (3.4a), (3.4b) are completed by the initial condition

$$\phi(0, \cdot) = \phi_{\text{init}}, \text{ in } \Omega_{\mathcal{P}}, \tag{3.4e}$$

where $\phi_{\text{init}} : \Omega_{\mathcal{P}} \to \mathbb{R}$ is a given function approximating the initial distribution of the two fluids in $\Omega_{\mathcal{P}}$.

3.2.2.2 The flow equations

Since the mixture velocity is volume averaged, and since we assume there is no excess volume after mixing, $\mathbf{v}$ is divergence free (see [2]),

$$\nabla \cdot \mathbf{v} = 0, \text{ in } Q. \tag{3.4f}$$

Here, the density and viscosity of the mixture are defined as $\rho(\phi) = \frac{\rho^{(1)}\cdot(1+\phi)}{2} + \frac{\rho^{(2)}\cdot(1-\phi)}{2}$, $\mu(\phi) = \frac{\mu^{(1)}\cdot(1+\phi)}{2} + \frac{\mu^{(2)}\cdot(1-\phi)}{2}$.

The momentum conservation law is a modified Navier-Stokes equation

$$\begin{aligned}&\partial_t\left(\rho(\phi)\mathbf{v}\right)+\nabla\cdot\left(\rho(\phi)\mathbf{v}\otimes\mathbf{v}\right)-\nabla\cdot\left(-p\mathbf{I}+2\mu(\phi)\mathcal{E}(\mathbf{v})+\mathbf{v}\otimes\rho'(\phi)\lambda\, m\,\nabla\psi\right)\\ &=\nabla\cdot\left(\gamma(c)\left(e_{\text{free}}(\phi,\nabla\phi)\mathbf{I}-\mathcal{C}\lambda\nabla\phi\otimes\nabla\phi\right)\right),\ \text{in}\ Q,\end{aligned}\tag{3.4g}$$

where p is a rescaled pressure. Here the flux term $(\mathbf{v}\otimes\rho'(\phi)\lambda\ m\ \nabla\psi)$ ensures thermodynamic consistency (see [2] and [69] for details) and the last two terms in (3.4g) account for the surface tension between the fluids. While such effects can be included in various ways (see [89]), here we adopt the approach in [69], based on the energy term $e_{\text{free}}(\phi,\nabla\phi)\mathbf{I}$ appearing in (3.4g). For convenience, from now on we use the following equivalent formulation of the momentum equation (3.4g)

$$\begin{aligned}&\partial_t\left(\rho(\phi)\mathbf{v}\right)+\nabla\cdot\left(\rho(\phi)\mathbf{v}\otimes\mathbf{v}\right)-\nabla\cdot\left(-p\mathbf{I}+2\mu(\phi)\mathcal{E}(\mathbf{v})+\mathbf{v}\otimes\rho'(\phi)\lambda\, m\,\nabla\psi\right)\\ &=\left(\frac{\mathcal{C}}{\lambda}\gamma(c)P'(\phi)-\nabla\cdot\left(\mathcal{C}\lambda\gamma(c)\nabla\phi\right)\right)\nabla\phi+\left(\frac{\mathcal{C}\lambda}{2}|\nabla\phi|^2+\frac{\mathcal{C}}{\lambda}P(\phi)\right)\nabla\gamma(c),\ \text{in}\ Q.\end{aligned}\tag{3.4h}$$

The solute transport model reads

$$\partial_t(I(\phi)c)+\nabla\cdot\left(I(\phi)\mathbf{v}c\right)=\nabla\cdot\left(D\,I(\phi)\nabla c\right),\ \text{in}\ Q.\tag{3.4i}$$

Note that as ϕ approaches -1, $I(\phi)$ vanishes, which is in line with the assumption that the solute is only present in fluid 1.

We assume that the velocity and solute flux are zero on the boundary

$$\mathbf{v}=\mathbf{0}\ \ \text{and}\ \ I(\phi)\nabla c\cdot\mathbf{n}=0\ \ \text{on}\ \ \partial\Omega_{\mathcal{P}},\ \ \text{for}\ \ t>0.\tag{3.4j}$$

Furthermore, the initial velocity and concentration are assumed to be known, $\mathbf{v}|_{t=0}=\mathbf{v}_{\text{init}}$ and $c|_{t=0}=c_{\text{init}}$ in $\Omega_{\mathcal{P}}$.

Remark. *Employing matched asymptotic expansions, in [69] it is shown that in the limit* $\lambda\to 0$, *the phase-field model discussed above reduces to the sharp-interface model in Section 3.2.1.*

3.3 Upscaling the pore-scale model to the Darcy scale

As stated in the introduction, we assume that, at the pore scale, the porous medium Ω consists of small but many periodically distributed impermeable grains, surrounded by a void space (the pore space). We are interested in the averaged behavior of the system, observed at the larger (Darcy) scale. At the same time, smaller (pore) scale information should not be disregarded. The pore scale and the Darcy scale are assumed well separated. With ℓ and L being the characteristic lengths of the pore scale and of the Darcy scale, we use $\epsilon = \frac{\ell}{L} \ll 1$ as the scale separation parameter.

To define the pore-scale domain, we write $Y = [0, \ell]^d, (d = 2, 3)$ as the union of the grain $\mathcal{G}$, its boundary $\partial\mathcal{G}$ and the surrounding pore space $\mathcal{P}$,

$$Y = \mathcal{P} \cup \mathcal{G} \cup \partial\mathcal{G}.$$

The entire porous medium occupies the domain

$$\Omega = \cup_{w \in W_\Omega} \{\ell w + Y\},$$

where $W_\Omega \subset \mathbb{Z}^d$ is a set of multi-indices. We assume that W_Ω is such that Ω is a connected set.

The phase-field model is defined in the entire pore space,

$$\Omega^\epsilon_{\mathcal{P}} = \cup_{w \in W_\Omega} \{\ell w + \mathcal{P}\},$$

which is also assumed to be connected.

The boundary of $\Omega^\epsilon_{\mathcal{P}}$ consists of the outer part, $\partial\Omega$, and the inner part, which is the union of the grain boundaries,

$$\Gamma^\epsilon_{\mathcal{G}} = \cup_{w \in W_\Omega} \{\ell w + \partial\mathcal{G}\}.$$

Note that the grains are not part of $\Omega^\epsilon_{\mathcal{P}}$. We refer to Figure 3.1 for a sketch of the domain.

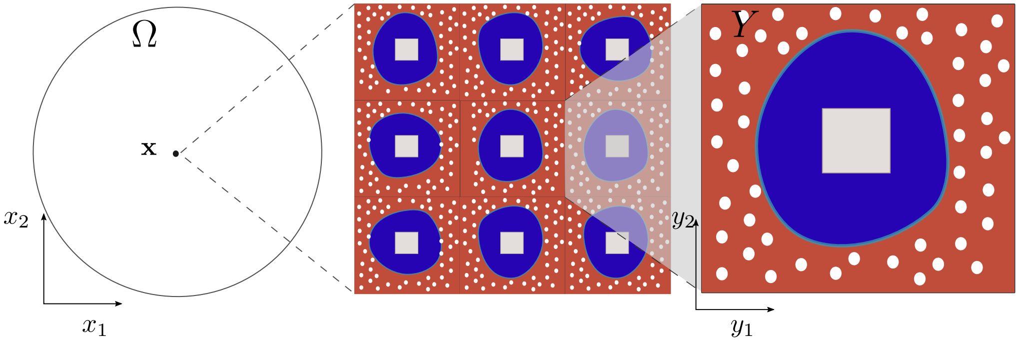

Figure 3.1: Schematic representation of the porous medium Ω. The figure in the middle presents periodically repeating grains (coloured gray) surrounded by void space (the pores) occupied by two immiscible fluids (blue and red). A surfactant soluble in fluid 1 is present (white particles). The right figure is a typical representation of a pore.

3.3.1 Non-dimensional model equations

For deriving the Darcy-scale model, we first bring the pore-scale model to a dimensionless form. To do so, we use the reference values and the non-dimensional quantities in Table 3.1, and the non-dimensional numbers

$$\begin{aligned} \mathrm{Eu} &= \frac{p_{\mathrm{ref}}}{\rho_{\mathrm{ref}} v_{\mathrm{ref}}^2}, \quad \mathrm{Re} = \frac{\rho_{\mathrm{ref}} v_{\mathrm{ref}} x_{\mathrm{ref}}}{\mu_{\mathrm{ref}}}, \quad \mathrm{Ca} = \frac{\mu_{\mathrm{ref}} v_{\mathrm{ref}}}{\gamma_{\mathrm{ref}}}, \\ \mathrm{Pe}_c &= \frac{v_{\mathrm{ref}} x_{\mathrm{ref}}}{D}, \quad \mathrm{A}_\phi = \frac{m\psi_{\mathrm{ref}}}{v_{\mathrm{ref}}}, \quad \mathrm{A}_\psi = \frac{\gamma_{\mathrm{ref}}}{x_{\mathrm{ref}} \psi_{\mathrm{ref}}}. \end{aligned} \tag{3.5}$$

Table 3.1: Reference values and non-dimensional quantities

Variables and parameters	Reference values	Units	Non-dimensional quantities
Time	t_{ref}	$[\mathrm{s}]$	$\hat{t} = t/t_{\text{ref}}$
Space (Darcy scale)	$x_{\text{ref}} = L$	$[\mathrm{m}]$	$\hat{\mathbf{x}} = \mathbf{x}/x_{\text{ref}}$
Space (pore scale)	$y_{\text{ref}} = \ell$	$[\mathrm{m}]$	$\hat{\mathbf{y}} = \mathbf{y}/y_{\text{ref}}$
Velocity	$v_{\text{ref}} = x_{\text{ref}}/t_{\text{ref}}$	$[\frac{\mathrm{m}}{\mathrm{s}}]$	$\hat{\mathbf{v}} = \mathbf{v}/v_{\text{ref}}$
Pressure	p_{ref}	$[\frac{\mathrm{kg}}{\mathrm{m\ s^2}}]$	$\hat{p} = p/p_{\text{ref}}$
Molar concentration	c_{ref}	$[\frac{\mathrm{mol}}{\mathrm{m^3}}]$	$\hat{c} = c/c_{\text{ref}}$
Density	ρ_{ref}	$[\frac{\mathrm{kg}}{\mathrm{m^3}}]$	$\hat{\rho} = \rho/\rho_{\text{ref}}$
Viscosity	μ_{ref}	$[\frac{\mathrm{kg}}{\mathrm{m\ s}}]$	$\hat{\mu} = \mu/\mu_{\text{ref}}$
Surface tension	γ_{ref}	$[\frac{\mathrm{kg}}{\mathrm{s^2}}]$	$\hat{\gamma}(\hat{c}) = \gamma(c_{\text{ref}}\,\hat{c})/\gamma_{\text{ref}}$
Diffuse interface thickness	$\lambda_{\text{ref}} = y_{\text{ref}} = \ell$	$[\mathrm{m}]$	$\hat{\lambda} = \lambda/y_{\text{ref}}$
	$\beta_{\text{ref}} = y_{\text{ref}} = \ell$	$[\mathrm{m}]$	$\hat{\beta} = \beta/y_{\text{ref}}$
Free energy	$e_{\text{free,ref}} = \frac{1}{x_{\text{ref}}}$	$[\frac{1}{\mathrm{m}}]$	$\hat{e}_{\text{free}} = e_{\text{free}}\, x_{\text{ref}}$
Cahn-Hilliard chemical potential	ψ_{ref}	$[\frac{\mathrm{kg}}{\mathrm{m\ s^2}}]$	$\hat{\psi} = \psi/\psi_{\text{ref}}$
Diffusion coefficient	D	$[\frac{\mathrm{m^2}}{\mathrm{s}}]$	
Cahn-Hilliard mobility	m	$[\frac{\mathrm{m^2\ s}}{\mathrm{kg}}]$	

Observe that the diffuse interface parameters λ and β are assumed to have the order of the pore-scale length ℓ. This corresponds to λ, β being of order $\mathcal{O}(\epsilon)$, as defined in Table 3.1. Here $\hat{\lambda}, \hat{\beta} \leq 1$, but these factors are independent of ϵ. Using the reference values and non-dimensional quantities from Table 3.1, and the non-dimensional numbers in (3.5), we obtain the dimensionless model (3.6). In the non-dimensional settings, we denote the pore space by $\hat{\mathbf{x}} \in \hat{\Omega}^{\epsilon}_{\mathcal{P}}$ and the inner boundary by $\hat{\Gamma}^{\epsilon}_{\mathcal{G}}$. Hence, one obtains

$$
\begin{aligned}
&\partial_{\hat t}\left(\hat\rho(\phi)\hat{\mathbf v}\right) + \hat\nabla\cdot\left(\hat\rho(\phi)\hat{\mathbf v}\otimes\hat{\mathbf v}\right) = \hat\nabla\cdot\left(-\mathrm{Eu}\,\hat p\mathbf I + \frac{1}{\mathrm{Re}}2\hat\mu(\phi)\mathcal E(\hat{\mathbf v})\right)\\
&\quad + \hat\nabla\cdot\left(\epsilon \mathrm{A}_\phi\hat\lambda\hat\rho'(\phi)\hat{\mathbf v}\otimes\hat\nabla\hat\psi\right) + \frac{1}{\mathrm{Re\ Ca}}\left(\frac{\mathcal C}{\epsilon\hat\lambda}\hat\gamma(\hat c)P'(\phi) - \hat\nabla\cdot\left(\epsilon\mathcal C\hat\lambda\hat\gamma(\hat c)\hat\nabla\phi\right)\right)\hat\nabla\phi\\
&\quad + \frac{1}{\mathrm{Re\ Ca}}\left(\frac{\epsilon\mathcal C\hat\lambda}{2}|\hat\nabla\phi|^2 + \frac{\mathcal C}{\epsilon\hat\lambda}P(\phi)\right)\hat\nabla\hat\gamma(\hat c), \qquad (3.6a)\\
&\hat\nabla\cdot\hat{\mathbf v} = 0, \qquad (3.6b)\\
&\partial_{\hat t}(I(\phi)\hat c) + \hat\nabla\cdot(I(\phi)\hat{\mathbf v}\hat c) = \frac{1}{\mathrm{Pe_c}}\hat\nabla\cdot\left(I(\phi)\hat\nabla\hat c\right), \qquad (3.6c)\\
&\partial_{\hat t}\phi + \hat\nabla\cdot(\hat{\mathbf v}\phi) = \epsilon\mathrm{A}_\phi\hat\lambda\hat\Delta\hat\psi, \qquad (3.6d)\\
&\hat\psi = \mathrm{A}_\psi\left(\frac{\mathcal C}{\epsilon\hat\lambda}\hat\gamma(\hat c)P'(\phi) + \frac{1}{\epsilon\hat\beta}\hat\gamma(\hat c)I'(\phi) - \hat\nabla\cdot\left(\epsilon\mathcal C\hat\lambda\hat\gamma(\hat c)\hat\nabla\phi\right)\right), \qquad (3.6e)
\end{aligned}
$$

for all $\hat{\mathbf x}\in\hat\Omega^\epsilon_{\mathcal P}$ and $\hat t > 0$. At the inner boundary $\hat\Gamma^\epsilon_{\mathcal G}$ and for $\hat t > 0$, one has

$$
\begin{aligned}
&\hat{\mathbf v} = 0, \qquad (3.6f)\\
&I(\phi)\hat\nabla\hat c\cdot\mathbf n = 0, \qquad (3.6g)\\
&\hat\nabla\phi\cdot\mathbf n = 0, \qquad (3.6h)\\
&\hat\nabla\hat\psi\cdot\mathbf n = 0. \qquad (3.6i)
\end{aligned}
$$

For the ease of presentation, since from now on only the non-dimensional quantities are considered, the hat is ommited in all notations.

3.3.2 Derivation of the two-scale model

We derive the upscaled counterpart of the phase-field model in Section 3.2.2. To do so, we employ formal asymptotic expansions w.r.t. ϵ. More precisely, we assume that all variables can be expanded regularly in terms of ϵ. For example, for ϕ one has

$$
\phi(t,\mathbf x) = \phi_0(t,\mathbf x,\frac{\mathbf x}{\epsilon}) + \epsilon\phi_1(t,\mathbf x,\frac{\mathbf x}{\epsilon}) + \mathcal O(\epsilon^2), \qquad (3.7)
$$

where the functions ϕ_i are Y-periodic w.r.t. the last argument. In other words, for $\mathrm{j} = 1, \ldots, \mathrm{d}$ and with $\mathbf{e}_\mathrm{j}$ being the unit vector in the j-th direction, one has $\phi_i(t, \mathbf{x}, \mathbf{y} + \mathbf{e}_\mathrm{j}) = \phi_i(t, \mathbf{x}, \mathbf{y})$. Similar expansions are used for $p, \mathbf{v}, c$. Note that the spatial variable $\mathbf{x}$ is doubled into the slow one, $\mathbf{x}$, accounting for the changes at the Darcy scale, and the fast variable $\mathbf{y} = \frac{\mathbf{x}}{\epsilon}$, where the rapid oscillations occur. With this the j-th spatial derivative ∂_{x_j} becomes $\partial_{x_\mathrm{j}} + \frac{1}{\epsilon}\partial_{y_\mathrm{j}}$ and

$$\nabla = \frac{1}{\epsilon}\nabla_{\mathbf{y}} + \nabla_{\mathbf{x}}. \tag{3.8}$$

Observe that, unlike [113], we do not consider an additional fast time scale, and do not disregard the $O(\epsilon)$ terms in the expansion of the phase field and of the velocity. At this point, we assume the following scaling of the dimensionless numbers (3.5),

$$\begin{aligned} &\mathrm{Eu} = \epsilon^{-2}\,\overline{\mathrm{Eu}}, \quad &&\mathrm{Re} = \overline{\mathrm{Re}}, \quad &&\mathrm{Ca} = \overline{\mathrm{Ca}}, \\ &\mathrm{Pe}_c = \overline{\mathrm{Pe}_c}, &&\mathrm{A}_\phi = \overline{\mathrm{A}_\phi}, &&\mathrm{A}_\psi = \epsilon\overline{\mathrm{A}_\psi}, \end{aligned} \tag{3.9}$$

where $\overline{\mathrm{Eu}}, \overline{\mathrm{Re}}, \overline{\mathrm{Ca}}, \overline{\mathrm{Pe}_c}, \overline{\mathrm{A}_\phi}$ and $\overline{\mathrm{A}_\psi}$ do not depend on ϵ. By choosing this scaling of the Euler number Eu and of the Reynolds number Re, we make sure that we are in the regime where Darcy's law is applicable, which corresponds to a laminar flow driven by the pressure gradient. The scaling of the capillary number Ca is chosen moderate w.r.t. ϵ. This choice results in equal pressures in both phases. Further, the Péclet number $\mathrm{Pe_c}$ is of order 1, which corresponds to the time scales of solute transport by advection and diffusion being of the same order. For simplicity, here $\overline{\mathrm{Ca}} = \overline{\mathrm{Pe_c}} = 1$. The scaling of A_ϕ and A_ψ is needed for the phase-field interface dynamics to be active at the pore scale.

For the ease of presentation, the dependency of $t, \mathbf{x}$ and $\mathbf{y}$ will in the following only be written whenever needed. Also, recall that all model variables are Y-periodic.

3.3.2.1 The flow equations

Inserting the asymptotic expansions in the reformulated momentum and mass conservation equations (3.6a) and (3.6b), and in the no-slip boundary condition (3.6f), and applying

(3.8), one obtains for all $t > 0$

$$
\begin{aligned}
&-\frac{1}{\epsilon^3}\overline{\mathrm{Eu}}\nabla_{\mathbf{y}} p_0 - \frac{1}{\epsilon^2}\overline{\mathrm{Eu}}\left(\nabla_{\mathbf{x}} p_0 + \nabla_{\mathbf{y}} p_1\right) + \frac{1}{\epsilon^2}\frac{1}{\overline{\mathrm{Re}}}\nabla_{\mathbf{y}} \cdot \left(2\mu(\phi_0)\mathcal{E}_{\mathbf{y}}(\mathbf{v}_0)\right) \\
&+ \frac{1}{\overline{\mathrm{Re}}\,\overline{\mathrm{Ca}}}\frac{1}{\epsilon^2}\left\{\left(\frac{\mathcal{C}}{\lambda}\gamma(c_0)P'(\phi_0) - \mathcal{C}\lambda\nabla_{\mathbf{y}} \cdot \left(\gamma(c_0)\nabla_{\mathbf{y}}\phi_0\right)\right)\nabla_{\mathbf{y}}\phi_0\right. \\
&\left.+\mathcal{C}\left(\frac{\lambda}{2}|\nabla_{\mathbf{y}}\phi_0|^2 + \frac{1}{\lambda}P(\phi_0)\right)\nabla_{\mathbf{y}}\gamma(c_0)\right\} + \mathcal{O}(\epsilon^{-1}) = 0, \qquad \text{in } \Omega \times \mathcal{P},
\end{aligned}
\tag{3.10a}
$$

$$
\frac{1}{\epsilon}\nabla_{\mathbf{y}} \cdot \mathbf{v}_0 + \nabla_{\mathbf{x}} \cdot \mathbf{v}_0 + \nabla_{\mathbf{y}} \cdot \mathbf{v}_1 + \mathcal{O}(\epsilon) = 0, \qquad \text{in } \Omega \times \mathcal{P},
\tag{3.10b}
$$

$$
\mathbf{v}_0 + \epsilon\mathbf{v}_1 + \mathcal{O}(\epsilon^2) = 0, \qquad \text{on } \Omega \times \partial\mathcal{G}.
\tag{3.10c}
$$

Here $\mathcal{E}_{\mathbf{y}}$ is the counterpart of $\mathcal{E}$, but involving derivatives in the fast variable $\mathbf{y}$. Since $|Y| = 1$, for all $t > 0$ and $\mathbf{x} \in \Omega$ we define the averaged velocity as

$$
\bar{\mathbf{v}}(t, \mathbf{x}) := \int_{\mathcal{P}} \mathbf{v}_0(t, \mathbf{x}, \mathbf{y})\, d\mathbf{y}.
\tag{3.11}
$$

The lowest order term in (3.10b) provides

$$
\nabla_{\mathbf{y}} \cdot \mathbf{v}_0 = 0,
\tag{3.12}
$$

for all $\mathbf{y} \in \mathcal{P}$. Next, the ϵ^0-order terms give

$$
\nabla_{\mathbf{x}} \cdot \mathbf{v}_0 + \nabla_{\mathbf{y}} \cdot \mathbf{v}_1 = 0,
\tag{3.13}
$$

for all $\mathbf{y} \in \mathcal{P}$. Integrating the above w.r.t $\mathbf{y}$, applying the Gauss theorem, and using the periodicity of $\mathbf{v}_1$ and the boundary condition $\mathbf{v}_1 = 0$ on $\partial\mathcal{G}$, one gets

$$
\nabla_{\mathbf{x}} \cdot \bar{\mathbf{v}} = 0,
\tag{3.14}
$$

for all $t > 0$ and $\mathbf{x} \in \Omega$. Equating the dominating $\mathcal{O}(\epsilon^{-3})$ term in (3.10a) gives

$$\nabla_{\mathbf{y}} p_0 = 0,$$

for all $\mathbf{y} \in \mathcal{P}$, so $p_0 = p_0(t, \mathbf{x})$. Further, in section 3.3.2.3 we also show that $c_0 = c_0(t, \mathbf{x})$ is independent of $\mathbf{y}$, and therefore, the last $\mathcal{O}(\epsilon^{-2})$ terms in (3.10a) are vanishing. Hence, the $\mathcal{O}(\epsilon^{-2})$ terms in (3.10a) yield

$$\begin{aligned}\overline{\overline{\mathrm{Eu}}}\nabla_{\mathbf{y}} p_1 - \frac{1}{\overline{\overline{\mathrm{Re}}}}\nabla_{\mathbf{y}} \cdot (2\mu(\phi_0)\mathcal{E}_{\mathbf{y}}(\mathbf{v}_0)) = -\overline{\overline{\mathrm{Eu}}}\nabla_{\mathbf{x}} p_0 \\ + \frac{1}{\overline{\overline{\mathrm{ReCa}}}}\gamma(c_0)\left(\frac{\mathcal{C}}{\lambda}P'(\phi_0) - \mathcal{C}\lambda\Delta_{\mathbf{y}}\phi_0\right)\nabla_{\mathbf{y}}\phi_0,\end{aligned} \tag{3.15}$$

for all $t > 0$, $\mathbf{x} \in \Omega$ and $\mathbf{y} \in \mathcal{P}$. Observe that (3.15) and (3.12) form a Stokes system in terms of the unknowns p_1 and $\mathbf{v}_0$, depending on p_0, ϕ_0 and c_0. This dependence can be made more precise through the cell problems, defined for all $\mathbf{x} \in \Omega$ and $t > 0$,

$$\begin{cases} \overline{\overline{\mathrm{Eu}}}\left(\mathbf{e}_{\mathrm{j}} + \nabla_{\mathbf{y}}\Pi_{\mathrm{j}}\right) = -\frac{1}{\overline{\overline{\mathrm{Re}}}}\nabla_{\mathbf{y}} \cdot \left(2\mu(\phi_0)\mathcal{E}_{\mathbf{y}}(\mathbf{w}_{\mathrm{j}})\right), & \text{in } \mathcal{P}, \\ \nabla_{\mathbf{y}} \cdot \mathbf{w}_{\mathrm{j}} = 0, & \text{in } \mathcal{P}, \\ \mathbf{w}_{\mathrm{j}} = \mathbf{0}, & \text{on } \partial\mathcal{G}, \\ \Pi_{\mathrm{j}}, \mathbf{w}_{\mathrm{j}} \text{ are } Y\text{-periodic and } \displaystyle\int_{\mathcal{P}} \Pi_{\mathrm{j}}\, d\mathbf{y} = 0, & \end{cases} \tag{3.16}$$

for $\mathrm{j} = 1, \ldots, \mathrm{d}$, and

$$\begin{cases} \overline{\overline{\mathrm{Eu}}}\nabla_{\mathbf{y}}\Pi_0 = -\frac{1}{\overline{\overline{\mathrm{Re}}}}\nabla_{\mathbf{y}} \cdot (2\mu(\phi_0)\mathcal{E}_{\mathbf{y}}(\mathbf{w}_0)) & \\ \qquad + \frac{1}{\overline{\overline{\mathrm{Re}}}\,\overline{\overline{\mathrm{Ca}}}}\left(\frac{\mathcal{C}}{\lambda}P'(\phi_0) - \mathcal{C}\lambda\Delta_{\mathbf{y}}\phi_0\right)\nabla_{\mathbf{y}}\phi_0, & \text{in } \mathcal{P}, \\ \nabla_{\mathbf{y}} \cdot \mathbf{w}_0 = 0, & \text{in } \mathcal{P}, \\ \mathbf{w}_0 = \mathbf{0}, & \text{on } \partial\mathcal{G}, \\ \Pi_0, \mathbf{w}_0 \text{ are } Y\text{-periodic and } \displaystyle\int_{\mathcal{P}} \Pi_0\, d\mathbf{y} = 0. & \end{cases} \tag{3.17}$$

By linearity, having solved the cell problems above, one immediately gets $\mathbf{v}_0$ and p_1 as functions of p_0, c_0 and, implicitly, of ϕ_0

$$\mathbf{v}_0(t,\mathbf{x},\mathbf{y}) = -\sum_{\mathtt{j}=1}^{d} \mathbf{w}_{\mathtt{j}}(t,\mathbf{x},\mathbf{y})\,\partial_{x_{\mathtt{j}}} p_0(t,\mathbf{x}) - \mathbf{w}_0(t,\mathbf{x},\mathbf{y})\,\gamma(c_0(t,\mathbf{x})), \tag{3.18}$$

$$p_1(t,\mathbf{x},\mathbf{y}) = \tilde{p}_1(t,\mathbf{x}) + \sum_{\mathtt{j}=1}^{d} \Pi_{\mathtt{j}}(t,\mathbf{x},\mathbf{y})\,\partial_{x_{\mathtt{j}}} p_0(t,\mathbf{x}) + \Pi_0(t,\mathbf{x},\mathbf{y})\gamma(c_0(t,\mathbf{x})). \tag{3.19}$$

Here $\tilde{p}_1 = \tilde{p}_1(t,\mathbf{x})$ is an arbitrary function not depending on $\mathbf{y}$. Integrating (3.18) w.r.t. $\mathbf{y}$ over $\mathcal{P}$ and using (3.11) yields

$$\bar{\mathbf{v}} = -\mathcal{K}\nabla_{\mathbf{x}} p_0 - \mathbf{M}\gamma(c_0), \tag{3.20}$$

for all $\mathbf{x} \in \Omega$ and $t > 0$. The elements of the effective matrix $\mathcal{K}(t,\mathbf{x})$ and the components of the effective vector $\mathbf{M}(t,\mathbf{x})$ are obtained using the solutions of the cell problems (3.16) and (3.17),

$$\mathcal{K}_{\mathtt{i},\mathtt{j}} = \int_{\mathcal{P}} \mathbf{w}_{\mathtt{i},\mathtt{j}}\, d\mathbf{y} \quad \text{and} \quad \mathbf{M}_{\mathtt{i}} = \int_{\mathcal{P}} \mathbf{w}_{\mathtt{i},0}\, d\mathbf{y}, \text{ with } \mathtt{i},\mathtt{j} = 1,\ldots,\mathtt{d}, \tag{3.21}$$

where $\mathbf{w}_{\mathtt{i},\alpha}$ is the $\mathtt{i}$-th component of $\mathbf{w}_\alpha$ ($\alpha \in \{0,\ldots,\mathtt{d}\}$).

3.3.2.2 The Cahn-Hilliard equations

By Taylor expansions about ϕ_0 and c_0, we can write

$$P(\phi) = P(\phi_0) + \epsilon\phi_1 P'(\phi_0) + \mathcal{O}(\epsilon^2),\ \gamma(c) = \gamma(c_0) + \epsilon c_1 \gamma'(c_0) + \mathcal{O}(\epsilon^2). \tag{3.22}$$

Using this and the homogenization ansatz (3.7) in equation (3.6d), (3.6e), (3.6h) and (3.6i), one gets for all $t > 0$

$$\begin{aligned}
\mathcal{O}(\epsilon) =& \frac{1}{\epsilon}\nabla_{\mathbf{y}} \cdot (\mathbf{v}_0\phi_0) - \frac{1}{\epsilon}\overline{\mathrm{A}_\phi}\lambda\Delta_{\mathbf{y}}\psi_0 + \partial_t\phi_0 + \nabla_{\mathbf{x}} \cdot (\mathbf{v}_0\phi_0) \\
&- \overline{\mathrm{A}_\phi}\lambda\left(\nabla_{\mathbf{x}} \cdot (\nabla_{\mathbf{y}}\psi_0) + \nabla_{\mathbf{y}} \cdot (\nabla_{\mathbf{x}}\psi_0) + \Delta_{\mathbf{y}}\psi_1\right), && \text{in } \Omega \times \mathcal{P}, && (3.23a)\\
\mathcal{O}(\epsilon) =& \psi_0 - \gamma(c_0)\overline{\mathrm{A}_\psi}\left(\frac{\mathcal{C}P'(\phi_0)}{\lambda} + \frac{I'(\phi_0)}{\beta} - \mathcal{C}\lambda\Delta_{\mathbf{y}}\phi_0\right), && \text{in } \Omega \times \mathcal{P}, && (3.23b)\\
\mathcal{O}(\epsilon) =& \frac{1}{\epsilon}\nabla_{\mathbf{y}}\phi_0 \cdot \mathbf{n} + \nabla_{\mathbf{x}}\phi_0 \cdot \mathbf{n} + \nabla_{\mathbf{y}}\phi_1 \cdot \mathbf{n}, && \text{on } \Omega \times \partial\mathcal{G}, && (3.23c)\\
\mathcal{O}(\epsilon) =& \frac{1}{\epsilon}\nabla_{\mathbf{y}}\psi_0 \cdot \mathbf{n} + \nabla_{\mathbf{x}}\psi_0 \cdot \mathbf{n} + \nabla_{\mathbf{y}}\psi_1 \cdot \mathbf{n}, && \text{on } \Omega \times \partial\mathcal{G}. && (3.23d)
\end{aligned}$$

Since $|Y| = 1$, the porosity of the medium is defined as

$$\Phi := |\mathcal{P}|. \tag{3.24}$$

We also define

$$\bar{\phi}(t, \mathbf{x}) := \frac{1}{\Phi}\int_{\mathcal{P}} \phi_0(t, \mathbf{x}, \mathbf{y})\, d\mathbf{y}. \tag{3.25}$$

Since ϕ_0 approaches 1 inside fluid 1, we use (3.4c) to define the fluid 1 saturation as

$$S := \frac{1}{\Phi}\int_{\mathcal{P}} I(\phi_0) d\mathbf{y} = \frac{1}{2}\left(1 + \bar{\phi}\right), \tag{3.26}$$

for all $t > 0$ and $\mathbf{x} \in \Omega$. Equating the lowest order terms in (3.23a)-(3.23d), and using (3.26), one gets the local cell problem for the phase field and the potential,

$$\begin{cases}
\nabla_{\mathbf{y}} \cdot (\mathbf{v}_0\phi_0) = \overline{\mathrm{A}_\phi}\lambda\Delta_{\mathbf{y}}\psi_0, & \text{in } \mathcal{P},\\
\psi_0 = \gamma(c_0)\overline{\mathrm{A}_\psi}\left(\frac{\mathcal{C}P'(\phi_0)}{\lambda} + \frac{I'(\phi_0)}{\beta} - \mathcal{C}\lambda\Delta_{\mathbf{y}}\phi_0\right), & \text{in } \mathcal{P},\\
\nabla_{\mathbf{y}}\phi_0 \cdot \mathbf{n} = 0, & \text{on } \partial\mathcal{G},\\
\nabla_{\mathbf{y}}\psi_0 \cdot \mathbf{n} = 0, & \text{on } \partial\mathcal{G},\\
\phi_0, \psi_0 \text{ are } Y\text{-periodic, and } \frac{1}{\Phi}\int_{\mathcal{P}} \phi_0\, d\mathbf{y} = 2\, S - 1,
\end{cases} \tag{3.27}$$

for all $t > 0$ and $\mathbf{x} \in \Omega$, where $\mathbf{v}_0$ is defined in (3.18). Observe that in the above equations only spatial derivatives w.r.t. $\mathbf{y}$ are present. The constraint $\frac{1}{\Phi} \int_{\mathcal{P}} \phi_0 \, d\mathbf{y} = 2\,S - 1$ follows from (3.26) and ensures the uniqueness of a solution.

The ϵ^0-order terms in (3.23a) equate to

$$\partial_t \phi_0 + \nabla_{\mathbf{x}} \cdot (\mathbf{v}_0 \phi_0) = \overline{\mathrm{A}_\phi} \lambda \left\{ \nabla_{\mathbf{x}} \cdot (\nabla_{\mathbf{y}} \psi_0) + \nabla_{\mathbf{y}} \cdot (\nabla_{\mathbf{x}} \psi_0) + \Delta_{\mathbf{y}} \psi_1 \right\}, \tag{3.28}$$

for all $t > 0$, $\mathbf{x} \in \Omega$ and $\mathbf{y} \in \mathcal{P}$. Integrating the above equation over $\mathcal{P}$ w.r.t $\mathbf{y}$ and using the periodicity of ψ_0 and ψ_1 yields

$$\partial_t \int_{\mathcal{P}} \phi_0 \, d\mathbf{y} + \nabla_{\mathbf{x}} \cdot \int_{\mathcal{P}} (\mathbf{v}_0 \phi_0) \, d\mathbf{y} = 0, \tag{3.29}$$

for all $t > 0$ and $\mathbf{x} \in \Omega$. Using (3.26), this becomes

$$\Phi \partial_t S + \frac{1}{2} \nabla_{\mathbf{x}} \cdot \bar{\mathbf{v}}^\phi = 0, \tag{3.30}$$

for all $t > 0$ and $\mathbf{x} \in \Omega$, where $\bar{\mathbf{v}}^\phi$ is the ϕ-dependent velocity given by

$$\bar{\mathbf{v}}^\phi(t, \mathbf{x}) := \int_{\mathcal{P}} \mathbf{v}_0(t, \mathbf{x}, \mathbf{y}) \phi_0(t, \mathbf{x}, \mathbf{y}) \, d\mathbf{y}. \tag{3.31}$$

Using (3.18) in the above equation, one finds

$$\bar{\mathbf{v}}^\phi = -\mathcal{K}^\phi \, \nabla_{\mathbf{x}} p_0 - \mathbf{M}^\phi \, \gamma(c_0), \tag{3.32}$$

for all $t > 0$ and $\mathbf{x} \in \Omega$, where the elements of the effective matrix $\mathcal{K}^\phi(t, \mathbf{x})$ and the components of the effective vector $\mathbf{M}^\phi(t, \mathbf{x})$ are defined by

$$\mathcal{K}^\phi_{\mathtt{i},\mathtt{j}} := \int_{\mathcal{P}} \mathbf{w}_{\mathtt{i},\mathtt{j}} \, \phi_0 \, d\mathbf{y} \quad \text{and} \quad \mathbf{M}^\phi_{\mathtt{i}} := \int_{\mathcal{P}} \mathbf{w}_{\mathtt{i},0} \, \phi_0 \, d\mathbf{y}, \text{ for } \mathtt{i}, \mathtt{j} = 1, \ldots, \mathtt{d}. \tag{3.33}$$

Again, $\mathbf{w}_{\mathtt{j}}$ and $\mathbf{w}_0$ are the solutions of the cell problems (3.16) and (3.17).

3.3.2.3 Solute conservation equation

Using the homogenization ansatz in (3.6c) and (3.6g) provides

$$\begin{aligned}
&-\frac{1}{\epsilon^2}\frac{1}{\overline{\mathrm{Pe}}_c}\nabla_{\mathbf{y}}\cdot\left(I(\phi_0)\nabla_{\mathbf{y}}c_0\right)+\frac{1}{\epsilon}\nabla_{\mathbf{y}}\cdot\left(I(\phi_0)\mathbf{v}_0c_0\right)-\frac{1}{\epsilon}\frac{1}{\overline{\mathrm{Pe}}_c}\nabla_{\mathbf{x}}\cdot\left(I(\phi_0)\nabla_{\mathbf{y}}c_0\right)\\
&-\frac{1}{\epsilon}\frac{1}{\overline{\mathrm{Pe}}_c}\nabla_{\mathbf{y}}\cdot\left(I(\phi_0)\left(\nabla_{\mathbf{x}}c_0+\nabla_{\mathbf{y}}c_1\right)+\phi_1\frac{1}{2}\nabla_{\mathbf{y}}c_0\right)+\partial_t(I(\phi_0)c_0)+\nabla_{\mathbf{x}}\cdot\left(I(\phi_0)\mathbf{v}_0c_0\right)\\
&+\nabla_{\mathbf{y}}\cdot\left(I(\phi_0)\left(\mathbf{v}_0c_1+\mathbf{v}_1c_0\right)+\phi_1\frac{1}{2}\mathbf{v}_0c_0\right)\\
&-\frac{1}{\overline{\mathrm{Pe}}_c}\nabla_{\mathbf{y}}\cdot\left(I(\phi_0)\left(\nabla_{\mathbf{x}}c_1+\nabla_{\mathbf{y}}c_2\right)+\phi_1\frac{1}{2}\left(\nabla_{\mathbf{x}}c_0+\nabla_{\mathbf{y}}c_1\right)\right)\\
&-\frac{1}{\overline{\mathrm{Pe}}_c}\nabla_{\mathbf{x}}\cdot\left(I(\phi_0)\left(\nabla_{\mathbf{x}}c_0+\nabla_{\mathbf{y}}c_1\right)+\phi_1\frac{1}{2}\nabla_{\mathbf{y}}c_0\right)+\mathcal{O}(\epsilon)=0,\qquad\text{in }\Omega\times\mathcal{P},
\end{aligned}\tag{3.34a}$$

$$\begin{aligned}
&\frac{1}{\epsilon}I(\phi_0)\nabla_{\mathbf{y}}c_0\cdot\mathbf{n}+I(\phi_0)\left(\nabla_{\mathbf{x}}c_0+\nabla_{\mathbf{y}}c_1\right)\cdot\mathbf{n}+\epsilon I(\phi_0)\left(\nabla_{\mathbf{x}}c_1+\nabla_{\mathbf{y}}c_2\right)\cdot\mathbf{n}\\
&+\epsilon\phi_1\frac{1}{2}\nabla_{\mathbf{y}}c_0\cdot\mathbf{n}+\mathcal{O}(\epsilon^2)=0,\qquad\text{on }\Omega\times\partial\mathcal{G}.
\end{aligned}\tag{3.34b}$$

The lowest order term from the above equations gives, for all $t > 0$ and $\mathbf{x} \in \Omega$,

$$\begin{aligned}
\nabla_{\mathbf{y}}\cdot\left(I(\phi_0)\nabla_{\mathbf{y}}c_0\right)&=0, &&\text{in }\mathcal{P},\text{ and}\\
I(\phi_0)\nabla_{\mathbf{y}}c_0\cdot\mathbf{n}&=0, &&\text{on }\partial\mathcal{G}.
\end{aligned}$$

Using the Y-periodicity of c_0, one immediately gets that $c_0 = c_0(t, \mathbf{x})$ is independent of $\mathbf{y}$. Further, the ϵ^{-1}-order terms in (3.34a) equate to

$$\frac{1}{\overline{\mathrm{Pe}}_c}\nabla_{\mathbf{y}}\cdot\left(I(\phi_0)\nabla_{\mathbf{y}}c_1\right)=-\frac{1}{\overline{\mathrm{Pe}}_c}\nabla_{\mathbf{y}}\cdot\left(I(\phi_0)\nabla_{\mathbf{x}}c_0\right)+c_0\left(\nabla_{\mathbf{y}}\cdot\left(I(\phi_0)\mathbf{v}_0\right)\right),\tag{3.35}$$

for all $t > 0$, $\mathbf{x} \in \Omega$ and $\mathbf{y} \in \mathcal{P}$. This, together with the boundary condition (3.34b), allows obtaining c_1 in terms of ϕ_0, c_0 and $\mathbf{v}_0$, by solving the cell problems

$$\begin{cases} \nabla_{\mathbf{y}} \cdot \left[I(\phi_0) \left(\nabla_{\mathbf{y}} \chi_{\mathrm{j}} + \mathbf{e}_{\mathrm{j}} \right) \right] = 0, & \text{in } \mathcal{P}, \\ I(\phi_0) \left(\nabla_{\mathbf{y}} \chi_{\mathrm{j}} + \mathbf{e}_{\mathrm{j}} \right) \cdot \mathbf{n} = 0, & \text{on } \partial\mathcal{G}, \\ \chi_{\mathrm{j}} \text{ is } Y\text{-periodic and } \displaystyle\int_{\mathcal{P}} \chi_{\mathrm{j}} \, d\mathbf{y} = 0, & \end{cases} \tag{3.36}$$

for $\mathrm{j} = 1, \ldots, \mathrm{d}$, and

$$\begin{cases} \nabla_{\mathbf{y}} \cdot \left[I(\phi_0) \nabla_{\mathbf{y}} \chi_0 \right] = \nabla_{\mathbf{y}} \cdot \left(I(\phi_0) \mathbf{v}_0 \right), & \text{in } \mathcal{P}, \\ I(\phi_0) \nabla_{\mathbf{y}} \chi_0 \cdot \mathbf{n} = 0, & \text{on } \partial\mathcal{G}, \\ \chi_0 \text{ is } Y\text{-periodic and } \displaystyle\int_{\mathcal{P}} \chi_0 \, d\mathbf{y} = 0. & \end{cases} \tag{3.37}$$

With (3.36) and (3.37), one has for all $t > 0$, $\mathbf{x} \in \Omega$ and $\mathbf{y} \in \mathcal{P}$

$$c_1(t, \mathbf{x}, \mathbf{y}) = \tilde{c}_1(t, \mathbf{x}) + \sum_{\mathrm{j}=1}^{d} \chi_{\mathrm{j}}(t, \mathbf{x}, \mathbf{y}) \, \partial_{x_{\mathrm{j}}} c_0(t, \mathbf{x}) + \chi_0(t, \mathbf{x}, \mathbf{y}) c_0(t, \mathbf{x}), \tag{3.38}$$

where $\tilde{c}_1 = \tilde{c}_1(t, \mathbf{x})$ is arbitrary. Finally, the ϵ^0-order terms in (3.34a) equate to

$$\begin{aligned} &\partial_t (I(\phi_0) c_0) + \nabla_{\mathbf{x}} \cdot (I(\phi_0) \mathbf{v}_0 c_0) - \frac{1}{\mathrm{Pe}_c} \nabla_{\mathbf{x}} \cdot \left(I(\phi_0) \left(\nabla_{\mathbf{x}} c_0 + \nabla_{\mathbf{y}} c_1 \right) \right) \\ &= -\nabla_{\mathbf{y}} \cdot \left(I(\phi_0) \left(\mathbf{v}_0 c_1 + \mathbf{v}_1 c_0 \right) + \phi_1 \frac{1}{2} \mathbf{v}_0 c_0 \right) + \frac{1}{\mathrm{Pe}_c} \nabla_{\mathbf{y}} \cdot \left(I(\phi_0) \left(\nabla_{\mathbf{x}} c_1 + \nabla_{\mathbf{y}} c_2 \right) \right) \\ &+ \frac{1}{\mathrm{Pe}_c} \nabla_{\mathbf{y}} \cdot \left(\phi_1 \frac{1}{2} \left(\nabla_{\mathbf{x}} c_0 + \nabla_{\mathbf{y}} c_1 \right) \right), \end{aligned} \tag{3.39}$$

for all $t > 0$, $\mathbf{x} \in \Omega$ and $\mathbf{y} \in \mathcal{P}$. Integrating the above w.r.t $\mathbf{y}$ over $\mathcal{P}$, using the definitions of the averaged velocity and ϕ-dependent velocity in (3.11) and (3.31), together with the periodicity, one gets the macroscopic law for the solute conservation

$$\Phi \, \partial_t \left(S \, c_0 \right) + \frac{1}{2} \nabla_{\mathbf{x}} \cdot \left(c_0 \left(\bar{\mathbf{v}} + \bar{\mathbf{v}}^{\phi} \right) \right) = \frac{1}{\mathrm{Pe}_c} \nabla_{\mathbf{x}} \cdot \left(\mathcal{B} \nabla_{\mathbf{x}} c_0 + \mathbf{H} c_0 \right), \tag{3.40}$$

for all $t > 0$ and $\mathbf{x} \in \Omega$. Here the elements of the effective matrix $\mathcal{B}(t, \mathbf{x})$ and the components of the effective vector $\mathbf{H}(t, \mathbf{x})$ are determined by

$$\mathcal{B}_{\mathtt{i},\mathtt{j}} = \int_{\mathcal{P}} I(\phi_0) \left(\delta_{\mathtt{ij}} + \partial_{\mathbf{y}_\mathtt{i}} \chi_\mathtt{j}\right)\, d\mathbf{y}, \quad \mathbf{H}_\mathtt{i} = \int_{\mathcal{P}} I(\phi_0) \partial_{\mathbf{y}_\mathtt{i}} \chi_0 \, d\mathbf{y}, \tag{3.41}$$

for $\mathtt{i}, \mathtt{j} = 1, \ldots, \mathtt{d}$, and where $\chi_\mathtt{j}$ and χ_0 solve the cell problems (3.36) and (3.37).

3.3.3 Summary of upscaled model

To simplify the notation, from here we give up the indices 0 in $\mathbf{v}_0, \phi_0, \psi_0, p_0$, and c_0. With this, the Darcy-type laws in (3.20) and (3.32) for the velocities, and the mass conservation laws for the two fluids and for the solute in (3.14), (3.30), and (3.40) can be written as

$$\bar{\mathbf{v}} = -\mathcal{K}\, \nabla p - \mathbf{M}\, \gamma(c), \tag{3.42a}$$

$$\nabla \cdot \bar{\mathbf{v}} = 0, \tag{3.42b}$$

$$\Phi\, \partial_t S + \frac{1}{2} \nabla \cdot \bar{\mathbf{v}}^\phi = 0, \tag{3.42c}$$

$$\bar{\mathbf{v}}^\phi = -\mathcal{K}^\phi\, \nabla p - \mathbf{M}^\phi\, \gamma(c), \tag{3.42d}$$

$$\Phi\, \partial_t (S\, c) + \frac{1}{2} \nabla \cdot \left(c \left(\bar{\mathbf{v}} + \bar{\mathbf{v}}^\phi\right)\right) = \frac{1}{\mathrm{Pe}_c} \nabla \cdot (\mathcal{B}\, \nabla c + \mathbf{H}\, c), \tag{3.42e}$$

defined for all $t > 0$ and $\mathbf{x} \in \Omega$. The Darcy-scale unknowns are $\bar{\mathbf{v}}(t, \mathbf{x})$, $S(t, \mathbf{x})$, $\bar{\mathbf{v}}^\phi(t, \mathbf{x})$, $p(t, \mathbf{x})$, and $c(t, \mathbf{x})$. This system is completed with boundary conditions on $\partial\Omega$, and the initial solute concentration c_{init}. Moreover, an initial (pore-scale) phase field ϕ_{init} is prescribed at each Darcy-scale point, yielding an initial saturation S_{init} satisfying (3.26). The effective parameters $\mathcal{K}$, $\mathcal{K}^\phi$, $\mathbf{M}$, $\mathbf{M}^\phi$, $\mathcal{B}$ and $\mathbf{H}$ are obtained by solving cell problems, as given in Table 3.2.

Table 3.2: Parameters for the upscaled model (3.42).

Effective parameters	Cell problems
$\mathcal{K}_{\mathtt{i},\mathtt{j}} = \int_{\mathcal{P}} \mathbf{w}_{\mathtt{i},\mathtt{j}}\; d\mathbf{y}$, $\mathcal{K}^{\phi}_{\mathtt{i},\mathtt{j}} = \int_{\mathcal{P}} \mathbf{w}_{\mathtt{i},\mathtt{j}}\;\phi\; d\mathbf{y}$.	$\overline{\mathsf{Eu}}\left(\mathbf{e}_{\mathtt{j}} + \nabla_{\mathbf{y}}\Pi_{\mathtt{j}}\right) = -\frac{1}{\mathsf{Re}}\nabla_{\mathbf{y}}\cdot\left(2\mu(\phi)\mathcal{E}_{\mathbf{y}}(\mathbf{w}_{\mathtt{j}})\right)$, in $\mathcal{P}$, $\nabla_{\mathbf{y}}\cdot\mathbf{w}_{\mathtt{j}} = 0$, in $\mathcal{P}$, $\mathbf{w}_{\mathtt{j}} = \mathbf{0}$, on $\partial\mathcal{G}$, $\Pi_{\mathtt{j}}, \mathbf{w}_{\mathtt{j}}$ are Y-periodic and $\int_{\mathcal{P}} \Pi_{\mathtt{j}}\; d\mathbf{y} = 0$, for $\mathtt{j} = 1, \ldots \mathtt{d}$.
$\mathbf{M}_{\mathtt{i}} = \int_{\mathcal{P}} \mathbf{w}_{\mathtt{i},0}\; d\mathbf{y}$, $\mathbf{M}^{\phi}_{\mathtt{i}} = \int_{\mathcal{P}} \mathbf{w}_{\mathtt{i},0}\;\phi\; d\mathbf{y}$.	$\overline{\mathsf{Eu}}\nabla_{\mathbf{y}}\Pi_0 = -\frac{1}{\mathsf{Re}}\nabla_{\mathbf{y}}\cdot\left(2\mu(\phi)\mathcal{E}_{\mathbf{y}}(\mathbf{w}_0)\right)$ $+\frac{1}{\mathsf{Re}\,\mathsf{Ca}}\left(\frac{\mathcal{C}}{\lambda}P'(\phi) - \mathcal{C}\lambda\Delta_{\mathbf{y}}\phi\right)\nabla_{\mathbf{y}}\phi$, in $\mathcal{P}$, $\nabla_{\mathbf{y}}\cdot\mathbf{w}_0 = 0$, in $\mathcal{P}$, $\mathbf{w}_0 = \mathbf{0}$, on $\partial\mathcal{G}$, $\Pi_0, \mathbf{w}_0$ are Y-periodic and $\int_{\mathcal{P}} \Pi_0\; d\mathbf{y} = 0$.
$\mathcal{B}_{\mathtt{i},\mathtt{j}} = \int_{\mathcal{P}} I(\phi)\left(\delta_{\mathtt{ij}} + \partial_{\mathbf{y}_{\mathtt{i}}}\chi_{\mathtt{j}}\right)\; d\mathbf{y}$.	$\nabla_{\mathbf{y}}\cdot\left[I(\phi)\left(\nabla_{\mathbf{y}}\chi_{\mathtt{j}} + \mathbf{e}_{\mathtt{j}}\right)\right] = 0$, in $\mathcal{P}$, $I(\phi)\left(\nabla_{\mathbf{y}}\chi_{\mathtt{j}} + \mathbf{e}_{\mathtt{j}}\right)\cdot\mathbf{n} = 0$, on $\partial\mathcal{G}$, $\chi_{\mathtt{j}}$ is Y-periodic and $\int_{\mathcal{P}} \chi_{\mathtt{j}}\; d\mathbf{y} = 0$, for $\mathtt{j} = 1, \ldots \mathtt{d}$.
$\mathbf{H}_{\mathtt{i}} = \int_{\mathcal{P}} I(\phi)\partial_{\mathbf{y}_{\mathtt{i}}}\chi_0\; d\mathbf{y}$.	$\nabla_{\mathbf{y}}\cdot\left[I(\phi)\nabla_{\mathbf{y}}\chi_0\right] = \nabla_{\mathbf{y}}\cdot\left(I(\phi_0)\mathbf{v}\right)$, in $\mathcal{P}$, $I(\phi)\nabla_{\mathbf{y}}\chi_0\cdot\mathbf{n} = 0$, on $\partial\mathcal{G}$, χ_0 is Y-periodic and $\int_{\mathcal{P}} \chi_0\; d\mathbf{y} = 0$.

To calculate the effective quantities, one needs the phase field $\phi(t, \mathbf{x}, \mathbf{y})$. This is obtained by solving for all $t > 0$ and $\mathbf{x} \in \Omega$ the problem

$$\begin{cases} \nabla_{\mathbf{y}}\cdot(\mathbf{v}\phi) = \overline{\mathrm{A}_{\phi}}\lambda\Delta_{\mathbf{y}}\psi, & \text{in } \mathcal{P}, \\ \psi = \overline{\mathrm{A}_{\psi}}\gamma(c)\left(\dfrac{\mathcal{C}P'(\phi)}{\lambda} + \dfrac{I'(\phi)}{\beta} - \mathcal{C}\lambda\Delta_{\mathbf{y}}\phi\right), & \text{in } \mathcal{P}, \\ \nabla_{\mathbf{y}}\phi\cdot\mathbf{n} = 0, \nabla_{\mathbf{y}}\psi\cdot\mathbf{n} = 0 & \text{on } \partial\mathcal{G}, \\ \phi \text{ and } \psi \text{ are } Y\text{-periodic and } \dfrac{1}{\Phi}\displaystyle\int_{\mathcal{P}}\phi\; d\mathbf{y} = 2\,S - 1. \end{cases} \tag{3.43}$$

Here $\mathbf{v}$ is nothing but the pore-scale velocity $\mathbf{v}_0$ in (3.18), namely

$$\mathbf{v}(t, \mathbf{x}, \mathbf{y}) = -\sum_{\mathtt{j}=1}^{d}\mathbf{w}_{\mathtt{j}}(t, \mathbf{x}, \mathbf{y})\;\partial_{x_{\mathtt{j}}}p(t, \mathbf{x}) - \mathbf{w}_0(t, \mathbf{x}, \mathbf{y})\;\gamma(c(t, \mathbf{x})). \tag{3.44}$$

Remark. *Inspired by the definition of the fluid 1 saturation S in (3.26), and since $\frac{1}{2}\left(\bar{\mathbf{v}}+\bar{\mathbf{v}}^{\phi}\right)=\frac{1}{2}\int_{\mathcal{P}}\mathbf{v}_0(1+\phi)\,d\mathbf{y}$ and $\frac{1}{2}\left(\bar{\mathbf{v}}-\bar{\mathbf{v}}^{\phi}\right)=\frac{1}{2}\int_{\mathcal{P}}\mathbf{v}_0(1-\phi)\,d\mathbf{y}$, one can identify the quantities corresponding to fluid i and reformulate the Darcy-scale equations accordingly. More precisely, we consider the (Darcy-scale) fluid-specific quantities*

$$\begin{aligned} S^{(1)}&=S, & \bar{\mathbf{v}}^{(1)}&=\frac{1}{2}\left(\bar{\mathbf{v}}+\bar{\mathbf{v}}^{\phi}\right), & \mathcal{K}^{(1)}&=\frac{(\mathcal{K}+\mathcal{K}^{\phi})}{2}, & \mathbf{M}^{(1)}&=\frac{(\mathbf{M}+\mathbf{M}^{\phi})}{2},\\ S^{(2)}&=1-S, & \bar{\mathbf{v}}^{(2)}&=\frac{1}{2}\left(\bar{\mathbf{v}}-\bar{\mathbf{v}}^{\phi}\right), & \mathcal{K}^{(2)}&=\frac{(\mathcal{K}-\mathcal{K}^{\phi})}{2}, & \mathbf{M}^{(2)}&=\frac{(\mathbf{M}-\mathbf{M}^{\phi})}{2}. \end{aligned}$$

Then, for all $t>0$ and $\mathbf{x}\in\Omega$, the Darcy-scale equations (3.42a)-(3.42d) become

$$\bar{\mathbf{v}}^{(i)}=-\mathcal{K}^{(i)}\,\nabla p-\mathbf{M}^{(i)}\,\gamma(c), \tag{3.45a}$$

$$\Phi\partial_t S^{(i)}+\nabla\cdot\bar{\mathbf{v}}^{(i)}=0, \tag{3.45b}$$

Note that (3.45a) is an enriched Darcy law, where the last term accounts for the surfactant effects, caused by a variable surface tension. Additionally, $\mathcal{K}^{(i)}$ is the relative permeability of fluid i multiplied by the absolute permeability of the medium, and $\mathbf{M}^{(i)}$ is connected to the effective variable surface-tension effect of the fluid phases. Finally, since $\bar{\mathbf{v}}^{(1)}+\bar{\mathbf{v}}^{(2)}=\bar{\mathbf{v}}$, (3.42b) implies that the total flow is divergence free. Moreover, even if the surface tension is constant, (3.45a) is still an enriched Darcy law because $\mathcal{K}^{(i)}$ and $\mathbf{M}^{(i)}$ both depend on ϕ, which is determined from (3.43).

Observe that (3.45a) and (3.45b) are similar to the standard effective model for two-phase flow when assuming a zero capillary pressure, respectively that the phase pressures are equal. In simplified geometries, such models are derived by transversal averaging, but assuming that the capillary number is moderate compared to ϵ, namely $O(1)$ (see [108, 162]). Additionally, a nonlinear fourth order parabolic equation is obtained in [115] for constant surface tension with capillary pressure, whereas in [117], the Buckley-Leverett equations are derived in the absence of surface tension.

Models disregarding the capillary pressure effects are quite popular in the numerical simulation of two-phase porous-media flows. Compared to these, even if the presence of a soluble surfactant is disregarded, one aspect is much different in the Darcy-scale model derived here. Commonly used models build on a relationship between the relative *permeability of a fluid phase and its saturation. Here, no such relationship is assumed, as the permeability is obtained from the pore scale, by solving the corresponding cell problems.*

3.4 A semi-explicit numerical scheme

For solving the two-scale model summarized in Section 3.3.3, we consider a simple, multi-scale numerical scheme. In this scheme, the solution of the pore-scale problems (3.16), (3.17), (3.36) and (3.37), and the solution of the Darcy-scale problem (3.42) are explicit, while the solution of the phase-field problem is implicit (3.43). Given $N \in \mathbb{N}$, we define the time step $\Delta t := \mathrm{T}/N$ and let $t^n = n\Delta t$. The time-discrete functions are denoted by

$$\phi^n := \phi(t^n, \cdot, \cdot), \quad \nu^n := \nu(t^n, \cdot) \quad \text{and} \quad \eta_{\mathtt{j}}^n := \eta_{\mathtt{j}}(t^n, \cdot),$$

where $\nu \in \{\mathcal{K}^\phi, \mathcal{K}, \mathbf{M}^\phi, \mathbf{M}, \mathcal{B}, \mathbf{H}, p, \bar{\mathbf{v}}, \bar{\mathbf{v}}^\phi, S, c\}$, and $\eta_{\mathtt{j}} \in \{\Pi_{\mathtt{j}}, \mathbf{w}_{\mathtt{j}}, \chi_{\mathtt{j}}\}$ with $\mathtt{j} = 0, 1, \ldots \mathtt{d}$. We denote the given initial data c^0, ϕ^0 and S^0, where S^0 satisfies (3.26). At each time step $n \geq 0$, the following steps are carried out.

Step 1. For each $\mathbf{x} \in \Omega$, compute the solution of the time-discrete counterpart of (3.16) and (3.17), i.e. obtain $(\Pi_{\mathtt{j}}^n, \mathbf{w}_{\mathtt{j}}^n)$ with $\mathtt{j} = 0, 1, \ldots \mathtt{d}$.

Step 2. Compute the time-discrete effective parameters $\mathcal{K}^{\phi,n}$, $\mathcal{K}^n$, $\mathbf{M}^{\phi,n}$ and $\mathbf{M}^n$.

Step 3. Compute the solution of the time-discrete counterpart of (3.42a) and (3.42b). Specifically, obtain p^n and $\bar{\mathbf{v}}^n$ by solving

$$\begin{aligned} \bar{\mathbf{v}}^n &= -\mathcal{K}^n \nabla p^n - \mathbf{M}^n \gamma(c^n), \\ \nabla \cdot \bar{\mathbf{v}}^n &= 0. \end{aligned} \tag{3.46}$$

Step 4. Use the explicit, time-discrete counterpart of (3.42c) and (3.42d) to compute

$$\begin{aligned} \bar{\mathbf{v}}^{\phi,n} &= -\mathcal{K}^{\phi,n} \, \nabla p^n - \mathbf{M}^{\phi,n} \, \gamma(c^n), \\ S^{n+1} &= S^n - \frac{\Delta t}{2\Phi} \nabla \cdot \bar{\mathbf{v}}^{\phi,n}. \end{aligned} \tag{3.47}$$

Step 5. For each $\mathbf{x} \in \Omega$, compute the pore-scale velocity $\mathbf{v}^n$ as in (3.18). Solve the time-discrete counterpart of (3.36) and (3.37), i.e. obtain $\chi^{\mathtt{j},n}$ with $\mathtt{j} = 0, 1, \ldots \mathtt{d}$.

Step 6. Compute the second set of time-discrete effective parameters $\mathcal{B}^n$ and $\mathbf{H}^n$.

Step 7. Compute the solution of the time-discrete counterpart of (3.42e). Specifically, obtain c^{n+1} by solving the following time-discrete problem

$$S^{n+1}c^{n+1} = S^n c^n + \frac{\Delta t}{\overline{\mathrm{Pe}}_c\ \Phi}\nabla\cdot\left(\mathcal{B}^n \nabla c^{n+1}\right) - \frac{\Delta t}{2\ \Phi}\nabla\cdot\left[\left(\bar{\mathbf{v}}^n + \bar{\mathbf{v}}^{\phi,n} - \frac{1}{\overline{\mathrm{Pe}}_c}\mathbf{H}^n\right)c^n\right]. \tag{3.48}$$

Step 8. For each $\mathbf{x} \in \Omega$, compute ϕ^{n+1}, the solution of (3.43) at $t = t^{n+1}$.

Remark. *Observe that the problem (3.43) is nonlinear. For solving it, we have adopted a linear iterative approach. More precisely, at each Darcy-scale mesh point $\mathbf{x} \in \Omega$ and time t^n, with $\mathcal{L} > 0$ large enough and letting $i \in \mathbb{N}$ be the iteration index, assuming $\phi^{n+1,i-1}$ known and Y-periodic, one solves the system*

$$\begin{cases} \nabla_{\mathbf{y}} \cdot (\mathbf{v}^n \phi^{n+1,i}) = \overline{\mathrm{A}_\phi}\lambda\Delta_{\mathbf{y}}\psi^{n+1,i}, & \textit{in } \mathcal{P}, \\ \psi^{n+1,i} = \overline{\mathrm{A}_\psi}\gamma(c^{n+1})\left(\dfrac{\mathcal{C}P'(\phi^{n+1,i-1})}{\lambda} + \dfrac{I'(\phi^{n+1,i-1})}{\beta}\right. & \\ \qquad\qquad \left. + \mathcal{L}(\phi^{n+1,i} - \phi^{n+1,i-1}) - \mathcal{C}\lambda\Delta_{\mathbf{y}}\phi^{n+1,i}\right), & \textit{in } \mathcal{P}, \\ \nabla_{\mathbf{y}}\phi^{n+1,i}\cdot\mathbf{n} = 0,\ \nabla_{\mathbf{y}}\psi^{n+1,i}\cdot\mathbf{n} = 0, & \textit{on } \partial\mathcal{G}, \\ \phi^{n+1,i} \textit{ and } \psi^{n+1,i} \textit{ are } Y\textit{-periodic and } \dfrac{1}{\Phi}\displaystyle\int_{\mathcal{P}} \phi^{n+1,i}\, d\mathbf{y} = 2S^{n+1} - 1. & \end{cases} \tag{3.49}$$

The velocity $\mathbf{v}^n$ is given in (3.44), computed for $t = t^n$. As a starting guess we choose the phase field at the previous time, $\phi^{n+1,0} = \phi^n$. However, the numerical experiments show that the iterations are convergent regardless of the initial guess.

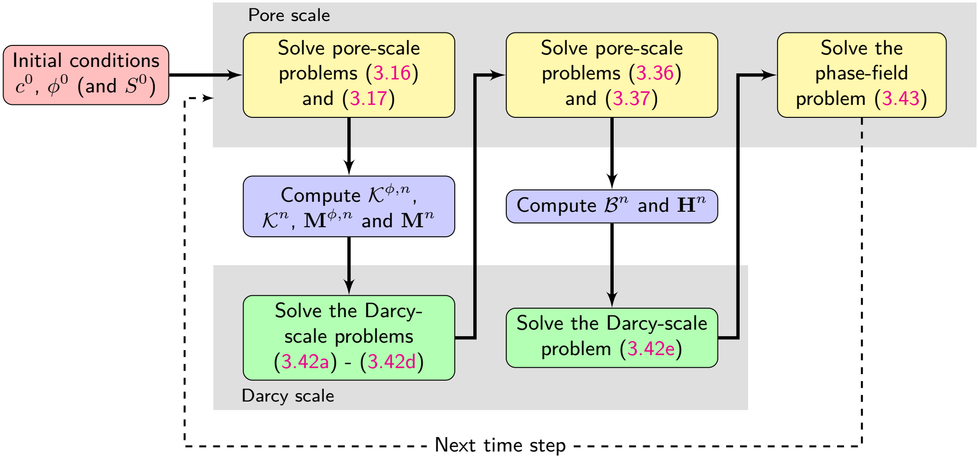

Figure 3.2: The two-scale scheme.

The two-scale scheme is presented in Figure 3.2. Observe that the time stepping in (3.47) is explicit. Note that the explicit spirit of the the scheme relies on its multi-scale nature. In this sense, the computation of a suitable time-step size or a CFL-condition implies further analysis but is beyond the scope of this thesis. For the spatial discretization, we consider $\mathfrak{T}_H$, a Darcy-scale triangular partition of the domain Ω. An element $T \in \mathfrak{T}_H$ has diameter H_T. For each Darcy-scale element T, the effective quantities are computed by solving the cell problems defined in a pore-scale domain $\mathcal{P}$. The triangular partition $\mathfrak{T}_h$ of $\mathcal{P}$ consists of elements T_μ of diameter h_{T_μ}. We let $H := \max_{T \in \mathfrak{T}_H} H_T$ and $h := \max_{T_\mu \in \mathfrak{T}_h} h_{T_\mu}$. The numerical solutions of the pore- and Darcy-scale problems (3.17), (3.37), (3.43), (3.46) and (3.48) are computed using the lowest order Raviart-Thomas elements (see [14]). For the pore-scale problems (3.16) and (3.36) we use the Crouzeix–Raviart elements (see [25, Section 8.6.2]).

To compute the evolution of the phase field accurately and, implicitly, of the effective parameters, one needs a fine pore-scale mesh for each cell problem. This mesh needs to be fine enough to resolve the diffuse interface zone of the phase-field. More details on the mesh construction can be found in [15, 16, 17].

3.5 Numerical results

In this section, we present two numerical experiments, carried out in the 2D case. We consider the (Darcy-scale) domain $\Omega = (0,1)\times(0,\frac{1}{2})$ and take $\mathrm{T} = 1$ as final time. In both tests, a zero initial concentration is considered, $c^0 \equiv 0$, while the initial phase field ϕ^0 does not change with the vertical Darcy-scale variable x_2 (see below). Therefore, the saturation S^0, obtained from (3.26), depends only on the horizontal variable, $S^0(\mathbf{x}) = f(x_1)$. The function f is within the range $[0.66, 0.86]$ (see Figure 3.3).

Every pore-scale domain Y has a centered inner grain $\mathcal{G} = (0.4, 0.6) \times (0.4, 0.6)$. This gives a constant porosity, $\Phi = 0.96$. For each $\mathbf{x} \in \Omega$, the initial phase field $\phi^0(\mathbf{x}, \cdot)$ is radially symmetric up to not being defined on $\mathcal{G}$. Its value changes from -1 (fluid 2, around $\mathcal{G}$) to 1 (fluid 1, the outer part of $\mathcal{P}$) in a thin, diffuse region around a circle. The radius of it changes in the x_1-direction but not in the x_2-direction.

Homogeneous Neumann boundary conditions are imposed for c and p at the upper and lower boundaries of Ω. The same applies for c at the right boundary. The pressure and concentration are prescribed at the left boundary, $p = p_{in} = 2$ and $c = c_{in}$. In the two tests, the only varying data is c_{in}. At the right boundary, a lower pressure is imposed, $p = p_{out} = 0$, causing a horizontal flow to the right. Therefore, the left and right boundaries are called in- and outflow boundaries. This is sketched in Figure 3.3.

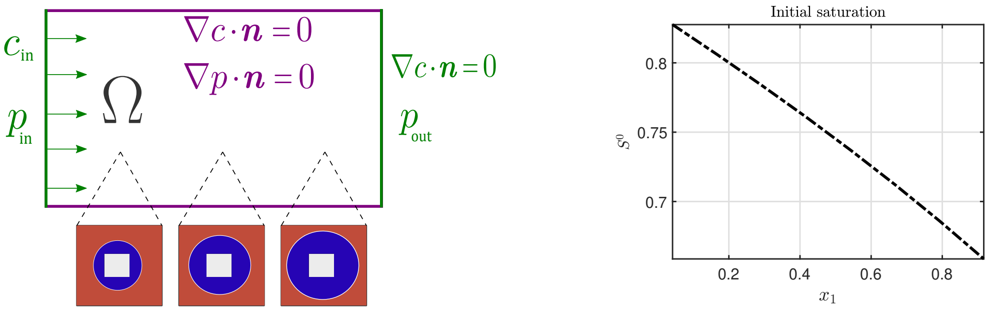

Figure 3.3: A sketch of the Darcy-scale boundary conditions and of the initial phase field at various locations (left), and the corresponding initial saturation (right).

We use the following non-dimensional parameters

$$\lambda = 0.02, \quad \mu_1 = 1, \quad \mu_2 = 0.9, \quad \beta = \overline{\mathrm{Ca}} = \overline{\mathrm{Eu}} = \overline{\mathrm{Re}} = \overline{\mathrm{Pe}_c} = \overline{\mathrm{A}_\phi} = \overline{\mathrm{A}_\psi} = 1,$$

and the given constant $\mathcal{C} = \frac{3}{2\sqrt{2}}$. To illustrate the effect of the solute-dependent surface tension, we let $\gamma(c) = -(100c + 1)$, and consider the following situations.

Test case 1. First we let $c = c_{in} = 0$. Then, the concentration remains 0 during the whole simulation.

Test case 2. With $c = c_{in} = 1$, the concentration is increasing in time for every $\mathbf{x}$, but remains decreasing in the x_1-direction for any t.

For the numerical simulation we use $\Delta t = 0.04$, thus we carry out 25 time steps. For the spatial discretization we construct a uniform Darcy-scale (coarse) mesh with mesh diameter $H = 0.1767$. At the pore scale we consider a uniform (fine) mesh with mesh diameter $h = 0.0283$.

In both test cases, the Darcy-scale solution components do not change with the vertical variable x_2. Therefore, these solutions are presented as a 1D projection/cut in the x_1-direction. Also, to illustrate the evolution in time of various Darcy-scale quantities, we choose $\mathbf{x}_{\mathrm{ref}} = (0.9167, 0.2917)$ as a reference Darcy-scale point. The behaviour in other points is similar. Also, to compare the results obtained in the two test cases, we present the evolution in time of the difference in the variables, calculated at $\mathbf{x}_{\mathrm{ref}}$. E.g. for the saturation S we compute

$$\delta S(t, \mathbf{x}_{\mathrm{ref}}) := S(t, \mathbf{x}_{\mathrm{ref}})\big|_{(\mathrm{TestCase2})} - S(t, \mathbf{x}_{\mathrm{ref}})\big|_{(\mathrm{TestCase1})},$$

for $t \in [0, 1]$, and similarly for other Darcy-scale variables, or effective matrix components and vector elements.

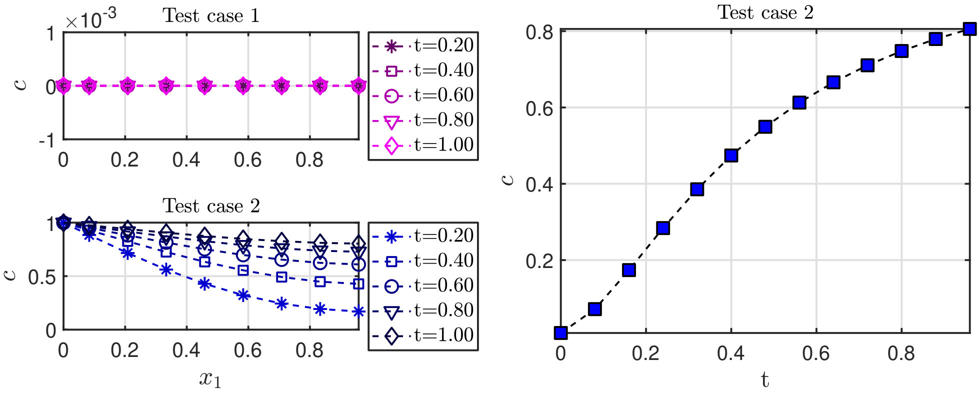

Figure 3.4: The concentration $c(t,\cdot)$ at five time steps for test case 1 (left-top) and test case 2 (left-bottom). The evolution of $c(\cdot,\mathbf{x}_{\text{ref}})$ for test case 2 (right).

The left plots in Figure 3.4 present the numerical approximation of the concentration c for the two test cases. Observe that, as expected, c remains 0 everywhere in the first test case. The right plot in Figure 3.4 shows the evolution of the concentration at the Darcy-scale reference point $\mathbf{x}_{\text{ref}}$ for the second test case.

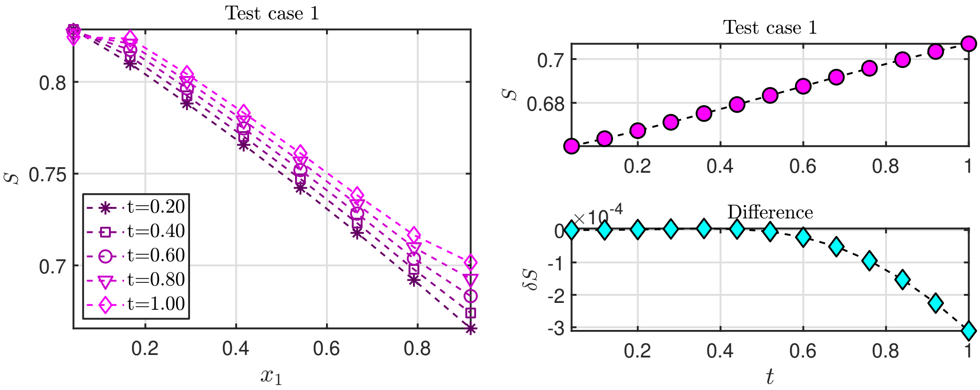

Figure 3.5: The saturation $S(t,\cdot)$ at five time steps, for the test case 1 (left). The evolution of $S(\cdot,\mathbf{x}_{\text{ref}})$ for the test case 1 (right-top) and of the difference $\delta S(\cdot,\mathbf{x}_{\text{ref}})$ between the two test cases (right-bottom).

The left plot in Figure 3.5 shows the numerical approximation of the saturation S for the test case 1. The saturation increases with time, but remains decreasing in the x_1-

direction. The evolution in time of $S(\cdot, \mathbf{x}_{\mathrm{ref}})$ is presented in the upper right plot. The lower right plot shows the difference in the saturations between the two test cases. Note that the saturation S is lower in the second test case as it increases less with time compared to the first test case. This is indirectly caused by the difference in the surface tension, leading to, as we will see below, a difference in the ϕ-weighted Darcy-scale velocity $\bar{\mathbf{v}}^{\phi}$.

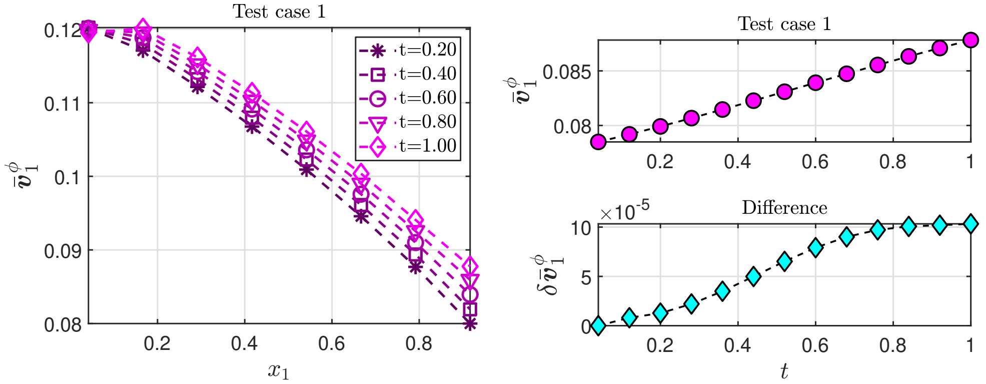

Figure 3.6: The horizontal component of the (Darcy-scale) velocity $\bar{\mathbf{v}}^{\phi}(t, \cdot)$, computed at five time steps, for the test case 1 (left). The evolution of $\bar{\mathbf{v}}_1^{\phi}(\cdot, \mathbf{x}_{\mathrm{ref}})$ for the test case 1 (right-top) and of the difference $\delta\bar{\mathbf{v}}_1^{\phi}(\cdot, \mathbf{x}_{\mathrm{ref}})$ between the two test cases (right-bottom).

Due to the setup, the horizontal component of the Darcy-scale velocity $\bar{\mathbf{v}}$ will remain constant over the domain. However, the velocity $\bar{\mathbf{v}}^{\phi}$ can still vary, and, as follows from (3.42c), this causes changes in the saturation. Moreover, this change becomes more natural when considering (3.45), in which the phase velocity depends on the (here, constant) $\bar{\mathbf{v}}$ and the variable $\bar{\mathbf{v}}^{\phi}$. We note that the vertical component of $\bar{\mathbf{v}}^{\phi}$ is zero, hence only the horizontal component is shown in Figure 3.6. As we see from the left plot in Figure 3.6, the horizontal component has a negative derivative with respect to x_1 throughout the domain, yielding an increasing saturation. However, from the difference shown in the lower right plot of Figure 3.6, the horizontal component of $\bar{\mathbf{v}}^{\phi}$ is higher in the test case 2 than in the test case 1. Hence, its derivative, though negative, is closer to 0, yielding a smaller increase in the saturation. Note that the reference point $\mathbf{x}_{\mathrm{ref}}$ is at the right part of the domain, and that saturation and velocity changes in points further left are less than in $\mathbf{x}_{\mathrm{ref}}$.

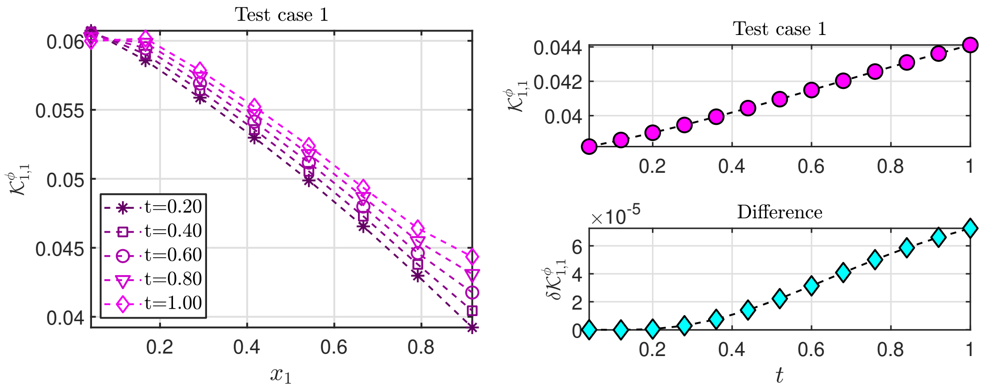

Figure 3.7: The first component of $\mathcal{K}^{\phi}(t,\cdot)$, computed at five time steps, for test case 1 (left). The evolution of $\mathcal{K}^{\phi}_{1,1}(\cdot,\mathbf{x}_{\text{ref}})$ for the test case 1 (right-top) and of the difference $\delta\mathcal{K}^{\phi}_{1,1}(\cdot,\mathbf{x}_{\text{ref}})$ between the two test cases, at $\mathbf{x}_{\text{ref}}$ (right-bottom).

Figure 3.7 and Figure 3.8 are displaying the evolution of the effective parameters from (3.42d), which are influencing $\bar{\mathbf{v}}^{\phi}_1$. The left plot in Figure 3.7 displays $\mathcal{K}^{\phi}_{1,1}$, while the time evolution of $\mathbf{M}^{\phi}_1$ is shown in Figure 3.8. Comparing the sizes, and accounting for the fact that the horizontal pressure drop is around -2, and $\gamma(c)$ is in the range $[-101,-1]$, it becomes clear that the horizontal pressure drop and the evolution of $\mathcal{K}^{\phi}_{1,1}$ dominate the changes in $\bar{\mathbf{v}}^{\phi}_1$ in both test cases considered here. Observe that, similarly to $\bar{\mathbf{v}}^{\phi}_1$, $\mathcal{K}^{\phi}_{1,1}$ increases with time in the right part of the domain, and stronger for the test case 2, causing a decreased divergence of $\bar{\mathbf{v}}^{\phi}$.

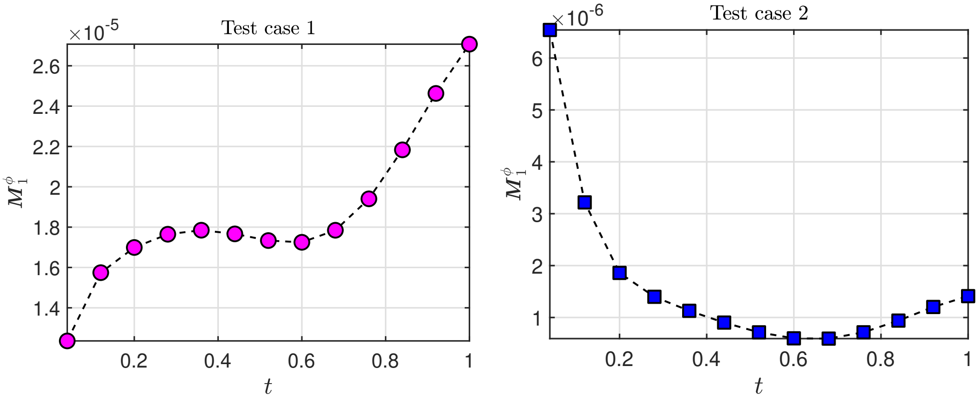

Figure 3.8: The evolution of the first element of $\mathbf{M}^{\phi}(\cdot,\mathbf{x}_{\text{ref}})$ for the two test cases.

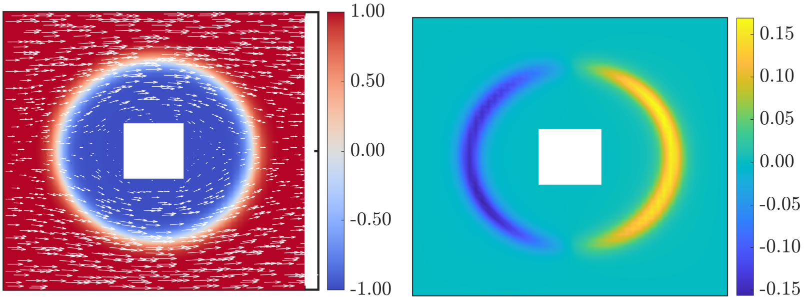

Figure 3.9: The evolution of the pore-scale phase field in the test case 1 (left) and the difference of the phase field $\delta\phi$ between the two test cases (right) corresponding to the Darcy-scale location $\mathbf{x}_{\text{ref}}$ at time $t = 1$.

The changes of $\mathcal{K}^{\phi}$ is depending on how the pore-scale phase-field evolves, which again depends on the surface tension. In Figure 3.9 we display the pore-scale phase field obtained at the final time $t = 1$, at the reference point $\mathbf{x}_{\text{ref}}$. The left plot in Figure 3.9 shows the numerical approximation of the phase field $\phi(1, \mathbf{x}_{\text{ref}}, \mathbf{y})$ and the pore-scale velocity $\mathbf{v}(1, \mathbf{x}_{\text{ref}}, \mathbf{y})$ (with $\mathbf{y} \in \mathcal{P}$), obtained in the first test case. Note that the pore-scale flow field is oriented mainly towards right. This immediately implies that the Darcy-scale velocity $\bar{\mathbf{v}}$ has the same orientation. The difference in the phase fields between the two test cases is displayed in the right plot. This difference is calculated for $t = 1$ and at $\mathbf{x}_{\text{ref}}$, using

$$\delta\phi(1, \mathbf{x}_{\text{ref}}, \mathbf{y}) = \phi(1, \mathbf{x}_{\text{ref}}, \mathbf{y})\big|_{(\text{TestCase2})} - \phi(1, \mathbf{x}_{\text{ref}}, \mathbf{y})\big|_{(\text{TestCase1})}.$$

As follows from the right plot, the phase-field profile in the second case corresponds to fluid 2 being shifted slightly to the left compared to the test case 1.

3.6 Conclusion

We have derived a two-scale model for the two-phase flow in a porous medium. The model takes into account the variations in the surface tension, caused by a surfactant soluble in one fluid phase. The starting point is the pore-scale model proposed in [69]. This is a Navier-Stokes-Cahn-Hilliard model for the flow, coupled with an advection-diffusion equation for solute concentration. In this way, the free boundaries separating the two fluid phases at the pore scale are approximated by thin diffuse interface regions, which allows formulating the problem in a fixed domain.

Using formal homogenization methods, we have derived a two-scale model consisting of mass conservation laws for the two phases and for the solute concentration, and of Darcy-type laws for the effective velocities. The latter include terms accounting for the concentration-dependent surface tension. These Darcy-scale laws involve effective parameters, which are obtained by solving local cell problems. These cell problems depend on the evolution of the phase field at the pore scale.

We have proposed a numerical algorithm building on the explicit Euler time discretization and on the lowest order Raviart-Thomas approximation in space. The explicit scheme requires solving seven pore-scale cell problems, defined for each Darcy-scale point. Note that the choice of Δt is empirical due to the complex multi-scale nature of the two-scale problem. These cell problems depend on Darcy-scale variables concentration, pressure and saturation. At the same time, for solving the Darcy-scale equations, one requires accurate calculations of the effective parameters, based on pore-scale quantities. These cell problems are generally small and parallelizable, allowing for efficient numerical strategies. In particular, for the phase-field cell problem, which is nonlinear and elliptic, we propose a simple, linear iterative scheme having a robust convergence, regardless of the initial guess.

Two test cases are presented, where the surface tension either remains constant, or where the changes in the concentration induce a varying surface tension. The fluids have different viscosities, but the viscosity ratio is small. The profiles of the Darcy-scale quantities display a similar behaviour in time and space in both test cases. Though small, differences in the results can be observed. In particular, the surfactant leads to decreased values of the saturation, as it affects the effective quantities, which depend on the pore-scale phase-field distribution.

Open issues are related to mesh refinement strategies at both the pore scale and the Darcy scale, as mentioned in [17]. Furthermore, adaptive strategies allowing to identify Darcy-scale points where the effective parameters need to be recalculated, and those where these values can be copied from points with a similar behaviour, could also improve the efficiency of the algorithm. Finally, implicit or semi-implicit higher-order numerical schemes for the two-scale model derived here need to be developed, as well as the rigorous analysis of the model and of the numerical approximation.

Chapter 4

Conclusions and outlook

This thesis addresses two-phase/unsaturated flow and surfactant transport in porous media. In particular, we focus on upscaling pore-scale models with evolving fluid-fluid interfaces and accounting for variations in the surface tension. To fulfill this purpose, we first apply transversal averaging for a simple geometry. The main contribution is the derivations of non-standard Darcy-scale models, which includes local pore-scale effects instead of traditionally postulated constitutive relationships ($p_c - S$- and $k_r - S$-relationship). Whereas for a more general domain, we apply periodic homogenization and derive a two-scale phase-field model involving effective parameters. These parameters are obtained by solving the derived pore-scale cell problems. In this way, this thesis contributes to the advancement of the research area of upscaling and modeling two-phase flow and transport trough porous media.

In the second chapter of the thesis, we consider two-phase/unsaturated flow at the pore scale, defined in a thin strip, and use a sharp-interface approach to model the evolution of the free boundary. By assuming that the ratio between the width and the length of the strip approaches 0, we use formal asymptotic expansion methods and average in the transversal direction to derive one-dimensional Darcy-scale models. The resulting averaged models involve Darcy-type laws for the flow, with a concentration-dependent surface tension effect (Marangoni effect) and a capillary pressure-saturation dependency involving the second-order derivative of the saturation.

These formal results are validated by numerical experiments. When the ratio of the width and the length of the pore approaches zero, we present numerical examples which show that the upscaled models are a good approximation of the transversal average of the solution to the pore-scale models. Comparing the Darcy-scale solutions with the transversal averaged pore-scale solutions shows that the Darcy-scale solutions are good approximations of the averaged transversal pore-scale solutions as the strip becomes longer and thinner. We numerically compare the upscaled models valid in the same capillary regime and show that the Marangoni effect influences the overall flow. Additionally, we find that one can use the unsaturated Darcy-scale model instead of the two-phase flow model when the viscosity ratio becomes large (or small).

Since the geometry largely influences the averaged/upscaled quantities and their behavior, in the third chapter of the thesis, we consider a more general domain, namely a periodically perforated domain. We use a phase-field model for two-phase flow and surfactant transport. We derive a two-scale phase-field model for the two-phase flow in a porous medium using periodic homogenization theory. The resulting two-scale model includes extended Darcy-type laws for the effective velocities, accounting for the concentration-dependent surface tension. The effective parameters represent quantities like relative permeability, which can be approximated by solving so-called local cell problems. These cell problems depend on the evolution of the phase field at the pore scale.

We propose a numerical algorithm to solve the two-scale phase-field model. We present numerical results highlighting the influence of the solute-dependent surface tension. We present simulations where the surface tension is either constant or variable. The results with varying surface tension show that, although small, there are visible differences that can be observed for the Darcy-scale variables (e.g., saturation, velocity) when compared to the constant surface tension case. In particular, the surfactant leads to a decreased saturation, affecting the effective quantities, which depend on the pore-scale phase-field distribution.

Outlook

There are still many open issues and challenges for upscaling two-phase flow and transport problems with evolving interfaces at the pore scale, which can be considered further. For the thin-strip models in Chapter 2, we assume that the two fluids have a layered structure and the free boundary is along the symmetry axis. An alternative to the layered structure is that the interface is transversal to the pore, so that fluid-fluid contact points are encountered at the pore walls. Then, one needs to consider contact angle conditions (static, dynamic, hysteretic) and, possibly, slip models. In [108], upscaling of two-phase flow with dynamic contact angle is addressed. However, both in [108] and here the influence of roughness has been neglected. That is, there is no roughness to the pore wall. Adding roughness of the pore wall is natural as in real porous materials the pore walls do have such a structure. For example, upscaling of single-phase flow with wall roughness is done in [96] and slip models are derived. However, adding roughness similar as in [96] for the case of two-phase flow is not straightforward due to interactions with contact line behavior.

When two fluids are moving through a porous medium, the phase pressure difference (capillary pressure) at the fluid-fluid interface within the pores generally changes with time. Additionally, the capillary pressure at the fluid-fluid interface depends on the surface tension. At the Darcy scale, capillary pressure is usually assumed to depend on the phase saturation and alters the overall flow distribution. As a consequence, capillary pressure plays an important role when modeling two-phase flow and transport trough porous media. Although considering a simple geometry, the upscaling procedure in Chapter 2 shows that the capillary pressure is not only a function of the saturation but also of its Laplacian. In this respect, the upscaled model derived from the phase-field model in Chapter 3 needs to be further analyzed for flow regimes with non-zero capillary pressure, as this may reveal further effects due to the evolving fluid-fluid interface.

In Chapters 2 and 3, we consider transport of a soluble surfactant and assume that the Péclet number (the ratio of the time scales for the diffusion and the convective transport) is of order 1. The upscaling procedure can be further investigated for different transport regimes (e.g., high Péclet number), which perhaps leads to the involvement of a dispersion term (e.g., Taylor dispersion, see [95]) in the upscaled model. Taylor dispersion leads to an increase of the effective diffusivity. Dispersion models are important when considering solute transport and high velocities.

The derivation of the Darcy-scale models are based on formal upscaling methods starting from the Navier-Stokes equations at the pore scale. Since the Darcy-scale solutions are approximations of the local pore-scale solutions, one may analyze the errors involved in the upscaling process by doing a rigorous analysis. However, the mathematical analysis of the Navier–Stokes equations for two fluids separated by a free boundary is an open research question which makes this rigorous analysis very difficult.

In Chapter 3, we propose a semi-explicit numerical scheme to solve the two-scale phase-field model. By considering the fully coupled nature of the two-scale problem, it would be better to consider implicit or semi-implicit schemes, combined with appropriate linearization approaches to simulate using longer time steps and hence improve the numerical robustness of the scheme. Moreover, to handle the multi-scale interactions between the sub-problems, one may consider an adaptive two-scale iterative strategy as in [15] which can improve the efficiency of the simulations.

Bibliography

[1] COMSOL Multiphysics® v. 5.4. www.comsol.com COMSOL AB, Stockholm, Sweden.

[2] H. Abels, H. Garcke, and G. Grün, Thermodynamically consistent, frame indifferent diffuse interface models for incompressible two-phase flows with different densities, Mathematical Models and Methods in Applied Sciences, 22 (2012), pp. 1150013, 40, https://doi.org/10.1142/S0218202511500138.

[3] E. Abreu, A. Bustos, P. Ferraz, and W. Lambert, A relaxation projection analytical-numerical approach in hysteretic two-phase flows in porous media, Journal of Scientific Computing, 79 (2019), pp. 1936–1980, https://doi.org/10.1007/s10915-019-00923-4.

[4] G. Allaire, Homogenization of the stokes flow in a connected porous medium, Asymptotic Analysis, 2 (1989), pp. 203–222, https://doi.org/10.3233/ASY-1989-2302.

[5] G. Allaire, Homogenization and two-scale convergence, SIAM Journal on Mathematical Analysis, 23 (1992), pp. 1482–1518, https://doi.org/10.1137/0523084.

[6] B. Amaziane, M. Jurak, and A. Vrbaški, Homogenization results for a coupled system modelling immiscible compressible two-phase flow in porous

media by the concept of global pressure, Applicable Analysis, 92 (2013), pp. 1417–1433, https://doi.org/10.1080/00036811.2012.682059.

[7] W. F. Ames, Numerical methods for partial differential equations, Academic press, 1977, https://doi.org/10.1016/C2013-0-10291-7.

[8] D. Anderson, J. Tannehill, and R. Pletcher, Computational fluid mechanics and heat transfer, Hemisphere Publishing Corporation, Taylor and Francis Group, New York, 1984, https://doi.org/10.1201/9781351124027.

[9] A. Armiti-Juber and C. Rohde, On the well-posedness of a nonlinear fourth-order extension of richards' equation, Journal of Mathematical Analysis and Applications, 487 (2020), p. 124005, https://doi.org/10.1016/j.jmaa.2020.124005.

[10] D. N. Arnold, Mixed finite element methods for elliptic problems, Computer methods in applied mechanics and engineering, 82 (1990), pp. 281–300, https://doi.org/10.1016/0045-7825(90)90168-L.

[11] H. Arunachalam, S. Onori, and I. Battiato, On veracity of macroscopic lithium-ion battery models, Journal of The Electrochemical Society, 162 (2015), p. A1940, https://doi.org/10.1149/2.0771509jes.

[12] J.-L. Auriault, C. Boutin, and C. Geindreau, Homogenization of coupled phenomena in heterogenous media, vol. 149, John Wiley & Sons, 2010, https://doi.org/10.1002/9780470612033.

[13] K. Aziz and A. Settari, Petroleum reservoir simulation, Applied Science Publishers, London, UK, (1979).

[14] C. Bahriawati and C. Carstensen, Three MATLAB implementations of the lowest-order Raviart-Thomas MFEM with a posteriori error control, Computational Methods in Applied Mathematics, 5 (2005), pp. 333–361, https://doi.org/10.2478/cmam-2005-0016.

[15] M. Bastidas, C. Bringedal, and I. S. Pop, A two-scale iterative scheme for a phase-field model for precipitation and dissolution in porous media, Applied

Mathematics and Computation, 396 (2021), p. 125933, https://doi.org/10.1016/j.amc.2020.125933.

[16] M. Bastidas, C. Bringedal, I. S. Pop, and F. A. Radu, Numerical homogenization of non-linear parabolic problems on adaptive meshes, Journal of Computational Physics, 425 (2020), p. 109903, https://doi.org/10.1016/j.jcp.2020.109903.

[17] M. Bastidas, S. Sharmin, C. Bringedal, and I. S. Pop, A numerical scheme for two-scale phase-field models in porous media, in Book of Extended Abstracts of the 6th ECCOMAS Young Investigators Conference YIC2021, Universitat Politècnica de València, Spain, 2021, https://doi.org/10.4995/YIC2021.2021.12571.

[18] I. Battiato, P. T. Ferrero V, D. O'Malley, C. T. Miller, P. S. Takhar, F. J. Valdés-Parada, and B. D. Wood, Theory and applications of macroscale models in porous media, Transport in Porous Media, 130 (2019), pp. 5–76, https://doi.org/10.1007/s11242-019-01282-2.

[19] v. Baňas and H. S. Mahato, Homogenization of evolutionary Stokes-Cahn-Hilliard equations for two-phase porous media flow, Asymptotic Analysis, 105 (2017), pp. 77–95, https://doi.org/10.3233/ASY-171436.

[20] J. Bear, Dynamics of Fluids in Porous Media, New York (N.Y.) : Dover, 1988.

[21] A. Beliaev and S. Hassanizadeh, A theoretical model of hysteresis and dynamic effects in the capillary relation for two-phase flow in porous media, Transport in Porous Media, 43 (2001), pp. 487–510, https://doi.org/10.1023/A:1010736108256.

[22] A. Y. Beliaev and R. J. Schotting, Analysis of a new model for unsaturated flow in porous media including hysteresis and dynamic effects, Computational Geosciences, 5 (2001), pp. 345–368, https://doi.org/10.1023/A:1014547019782.

[23] L. Bergamaschi and M. Putti, Mixed finite elements and Newton-type linearizations for the solution of Richards' equation, International journal for numerical methods in engineering, 45 (1999), pp. 1025–1046.

[24] R. Bird, W. Stewart, and E. Lightfoot, Transport phenomena, New York: John Wiley & Sons, Inc, (1960), p. 780.

[25] D. Boffi, F. Brezzi, and M. Fortin, Mixed finite element methods and applications, vol. 44, Springer Berlin, Heidelberg, 2013, https://doi.org/10.1007/978-3-642-36519-5.

[26] S. Bottero, S. M. Hassanizadeh, P. J. Kleingeld, and T. J. Heimovaara, Nonequilibrium capillarity effects in two-phase flow through porous media at different scales, Water Resources Research, 47 (2011), https://doi.org/10.1029/2011WR010887.

[27] A. Bourgeat, S. Luckhaus, and A. Mikelić, Convergence of the homogenization process for a double-porosity model of immiscible two-phase flow, SIAM Journal on Mathematical Analysis, 27 (1996), pp. 1520–1543, https://doi.org/10.1137/S0036141094276457.

[28] F. Boyer, C. Lapuerta, S. Minjeaud, B. Piar, and M. Quintard, Cahn-Hilliard/Navier-Stokes model for the simulation of three-phase flows, Transport in Porous Media, 82 (2010), pp. 463–483, https://doi.org/10.1007/s11242-009-9408-z.

[29] D. Braess, Finite elements: Theory, fast solvers, and applications in solid mechanics, Cambridge University Press, 2007, https://doi.org/10.1017/CBO9780511618635.

[30] S. C. Brenner, L. R. Scott, and L. R. Scott, The mathematical theory of finite element methods, vol. 3, Springer, New York, NY, 2008, https://doi.org/10.1007/978-0-387-75934-0.

[31] D. Bresch, Shallow-water equations and related topics, in Handbook of differential equations: evolutionary equations., Elsevier/North-Holland, Amsterdam, 2009, pp. 1–104, https://doi.org/10.1016/S1874-5717(08)00208-9.

[32] F. Brezzi and M. Fortin, Mixed and hybrid finite element methods, vol. 15, Springer New York, NY, 1991, https://doi.org/10.1007/978-1-4612-3172-1.

[33] C. Bringedal, I. Berre, I. S. Pop, and F. A. Radu, A model for non-isothermal flow and mineral precipitation and dissolution in a thin strip, Journal of Computational and Applied Mathematics, 289 (2015), pp. 346 – 355, https://doi.org/10.1016/j.cam.2014.12.009.

[34] C. Bringedal, I. Berre, I. S. Pop, and F. A. Radu, Upscaling of non-isothermal reactive porous media flow with changing porosity, Transport in Porous Media, 114 (2016), pp. 371–393, https://doi.org/10.1007/s11242-015-0530-9.

[35] C. Bringedal, I. Berre, I. S. Pop, and F. A. Radu, Upscaling of non-isothermal reactive porous media flow under dominant peclet number: The effect of changing porosity, Multiscale Modeling & Simulation, 14 (2016), pp. 502–533, https://doi.org/10.1137/15M1022781.

[36] C. Bringedal and K. Kumar, Effective behavior near clogging in upscaled equations for non-isothermal reactive porous media flow, Transport in Porous Media, 120 (2017), pp. 553–577, https://doi.org/10.1007/s11242-017-0940-y.

[37] C. Bringedal, L. Von Wolff, and I. S. Pop, Phase field modeling of precipitation and dissolution processes in porous media: upscaling and numerical experiments, Multiscale Modeling & Simulation, 18 (2020), pp. 1076–1112, https://doi.org/10.1137/19M1239003.

[38] R. Brooks and A. Corey, Hydraulic properties of porous media and their relation to drainage design, Transactions of the ASAE, 7 (1964), pp. 26–0028, https://doi.org/10.13031/2013.40684.

[39] R. H. Brooks and A. T. Corey, Properties of porous media affecting fluid flow, Journal of the irrigation and drainage division, 92 (1966), pp. 61–88, https://doi.org/10.1061/JRCEA4.0000425.

[40] E. Buckingham, Studies on the movement of soil moisture, Bulletin (United States. Bureau of Soils), 38 (1907).

[41] S. E. Buckley and M. Leverett, Mechanism of fluid displacement in sands, Transactions of the AIME, 146 (1942), pp. 107–116, https://doi.org/10.2118/942107-G.

[42] R. Bunoiu, G. Cardone, R. Kengne, and J. L. Woukeng, Homogenization of 2D Cahn-Hilliard-Navier-Stokes system, Journal of Elliptic and Parabolic Equations, 6 (2020), pp. 377–408, https://doi.org/10.1007/s41808-020-00074-w.

[43] R. L. Burden, J. D. Faires, and A. M. Burden, Numerical analysis, Cengage learning, 2015.

[44] N. Burdine, Relative Permeability Calculations From Pore Size Distribution Data, Journal of Petroleum Technology, 5 (1953), pp. 71–78, https://doi.org/10.2118/225-G.

[45] J. C. Butcher, Numerical methods for ordinary differential equations, John Wiley & Sons, 2016, https://doi.org/10.1002/9781119121534.

[46] G. Caginalp and P. C. Fife, Dynamics of layered interfaces arising from phase boundaries, SIAM journal on Applied Mathematics, 48 (1988), pp. 506–518, https://doi.org/10.1137/0148029.

[47] J. W. Cahn and J. E. Hilliard, Free energy of a nonuniform system. i. interfacial free energy, The Journal of Chemical Physics, 28 (1958), pp. 258–267, https://doi.org/10.1063/1.1744102.

[48] M. A. Celia and J. M. Nordbotten, Geological Storage of CO2: Modeling Approaches for Large-scale Simulation, John Wiley & Sons, Hoboken, NJ,, 2011, https://doi.org/10.1002/9781118137086.

[49] C.-M. CHANG, M. W. KEMBLOWSKI, J. J. KALUARACHCHI, AND A. ABDIN, Stochastic analysis of two-phase flow in porous media: I. Spectral/perturbation approach, Transport in Porous Media, 19 (1995), pp. 233–259, https://doi.org/10.1007/BF00617531.

[50] M. CHAPWANYA AND J. M. STOCKIE, Numerical simulations of gravity-driven fingering in unsaturated porous media using a nonequilibrium model, Water Resources Research, 46 (2010), https://doi.org/10.1029/2009WR008583.

[51] J. CHEN, S. SUN, AND X. WANG, Homogenization of two-phase fluid flow in porous media via volume averaging, Journal of Computational and Applied Mathematics, 353 (2019), pp. 265–282, https://doi.org/10.1016/j.cam.2018.12.023.

[52] D. CIORANESCU AND P. DONATO, An introduction to homogenization, vol. 17 of Oxford Lecture Series in Mathematics and its Applications, The Clarendon Press, Oxford University Press, New York, 1999.

[53] R. V. CRASTER AND O. K. MATAR, Dynamics and stability of thin liquid films, Reviews of Modern Physics, 81 (2009), p. 1131, https://doi.org/10.1103/RevModPhys.81.1131.

[54] L. CUETO-FELGUEROSO AND R. JUANES, Nonlocal interface dynamics and pattern formation in gravity-driven unsaturated flow through porous media, Physical Review Letters, 101 (2008), p. 244504, https://doi.org/10.1103/PhysRevLett.101.244504.

[55] L. CUETO-FELGUEROSO AND R. JUANES, A phase field model of unsaturated flow, Water Resources Research, 45 (2009), https://doi.org/10.1029/2009WR007945.

[56] J. H. CUSHMAN, L. S. BENNETHUM, AND B. X. HU, A primer on upscaling tools for porous media, Advances in Water Resources, 25 (2002), pp. 1043–1067, https://doi.org/10.1016/S0309-1708(02)00047-7.

[57] K. R. Daly and T. Roose, Homogenization of two fluid flow in porous media, Proceedings of the Royal Society A., 471 (2015), pp. 20140564, 20, https://doi.org/10.1098/rspa.2014.0564.

[58] H. P. G. Darcy, Les Fontaines publiques de la ville de Dijon. Exposition et application des principes à suivre et des formules à employer dans les questions de distribution d'eau, etc, V. Dalamont, 1856.

[59] D. A. DiCarlo, Experimental measurements of saturation overshoot on infiltration, Water Resources Research, 40 (2004), https://doi.org/10.1029/2003WR002670.

[60] D. A. DiCarlo, Experimental measurements of saturation overshoot on infiltration, Water Resources Research, 40 (2004), https://doi.org/10.1029/2003WR002670.

[61] F. Doster and R. Hilfer, Generalized buckley-leverett theory for two-phase flow in porous media, New Journal of Physics, 13 (2011), https://doi.org/10.1088/1367-2630/13/12/123030.

[62] H. Eichel, R. Helmig, I. Neuweiler, and O. A. Cirpka, Upscaling of two-phase flow processes in porous media, in Upscaling multiphase flow in porous media, Springer, 2005, pp. 237–257, https://doi.org/10.1007/1-4020-3604-3_12.

[63] R. Farahi, A. Passian, T. Ferrell, and T. Thundat, Microfluidic manipulation via marangoni forces, Applied physics letters, 85 (2004), pp. 4237–4239, https://doi.org/10.1063/1.1812830.

[64] C. Farmer, Upscaling: a review, International journal for numerical methods in fluids, 40 (2002), pp. 63–78, https://doi.org/10.1002/fld.267.

[65] A. Fasano and A. Mikelić, The 3D flow of a liquid through a porous medium with absorbing and swelling granules, Interfaces and Free Boundaries, 4 (2002), pp. 239–261, https://doi.org/10.4171/IFB/60.

[66] F. FRANK, C. LIU, F. O. ALPAK, AND B. RIVIERE, A finite volume / discontinuous galerkin method for the advective cahn–hilliard equation with degenerate mobility on porous domains stemming from micro-ct imaging, Computational Geosciences, 22 (2018), pp. 543–563, https://doi.org/10.1007/s10596-017-9709-1.

[67] S. GAERTTNER, P. FROLKOVIC, P. KNABNER, AND N. RAY, Efficiency and accuracy of micro-macro models for mineral dissolution, Water Resources Research, 56 (2020), https://doi.org/10.1029/2020WR027585.

[68] R. E. GARCIA, Y.-M. CHIANG, W. C. CARTER, P. LIMTHONGKUL, AND C. M. BISHOP, Microstructural modeling and design of rechargeable lithium-ion batteries, Journal of The Electrochemical Society, 152 (2004), p. A255, https://doi.org/10.1016/j.jpowsour.2015.11.058.

[69] H. GARCKE, K. F. LAM, AND B. STINNER, Diffuse interface modelling of soluble surfactants in two-phase flow, Communications in mathematical sciences, 12 (2014), pp. 1475–1522, https://doi.org/10.4310/CMS.2014.V12.N8.A6.

[70] R. GLASS, T. STEENHUIS, AND J.-Y. PARLANGE, Mechanism for finger persistence in homogeneous, unsaturated, porous media: theory and verification, Soil Science, 148 (1989), pp. 60–70, https://doi.org/10.1097/00010694-198907000-00007.

[71] R. J. GLASS, T. S. STEENHUIS, AND J.-Y. PARLANGE, Mechanism for finger persistence in homogeneous, unsaturated, porous media: Theory and verification, Soil Science, 148 (1989), pp. 60–70.

[72] A. GOLPARVAR, Y. ZHOU, K. WU, J. MA, AND Z. YU, A comprehensive review of pore scale modeling methodologies for multiphase flow in porous media, Advances in Geo-Energy Research, 2 (2018), pp. 418–440, https://doi.org/10.26804/ager.2018.04.07.

[73] Z. GUO AND P. LIN, A thermodynamically consistent phase-field model for two-phase flows with thermocapillary effects, Journal of Fluid Mechanics, 766 (2015), pp. 226–271, https://doi.org/10.1017/jfm.2014.696.

[74] T. Harter and J. W. Hopmans, Role of vadose-zone flow processes in regional-scale hydrology: review, opportunities and challenges, Frontis, (2005), pp. 179–208.

[75] C. Hartnett, I. Seric, K. Mahady, L. Kondic, S. Afkhami, J. D. Fowlkes, and P. Rack, Exploiting the marangoni effect to initiate instabilities and direct the assembly of liquid metal filaments, Langmuir, 33 (2017), pp. 8123–8128, https://doi.org/10.1021/acs.langmuir.7b01655.

[76] S. M. Hassanizadeh and W. G. Gray, Mechanics and thermodynamics of multiphase flow in porous media including interphase boundaries, Advances in Water Resources, 13 (1990), pp. 169–186, https://doi.org/10.1016/0309-1708(90)90040-B.

[77] S. M. Hassanizadeh and W. G. Gray, Thermodynamic basis of capillary pressure in porous media, Water Resources Research, 29 (1993), pp. 3389–3405, https://doi.org/10.1029/93WR01495.

[78] R. Helmig et al., Multiphase flow and transport processes in the subsurface: a contribution to the modeling of hydrosystems., Springer, Berlin, 1997, https://doi.org/10.1017/S0025315400040170.

[79] R. Helmig, J. Niessner, B. Flemisch, M. Wolff, and J. Fritz, Efficient Modeling of Flow and Transport in Porous Media Using Multiphysics and-Multiscale Approaches, Springer Berlin Heidelberg, 2010, pp. 417–457, https://doi.org/10.1007/978-3-642-01546-5_15.

[80] R. Hilfer, F. Doster, and P. A. Zegeling, Nonmonotone saturation profiles for hydrostatic equilibrium in homogeneous porous media, Vadose Zone Journal, 11 (2012), https://doi.org/10.2136/vzj2012.0021.

[81] R. Hilfer and P. Øren, Dimensional analysis of pore scale and field scale immiscible displacement, Transport in Porous Media, 22 (1996), pp. 53–72, https://doi.org/10.1007/BF00974311.

[82] R. HILFER AND R. STEINLE, Saturation overshoot and hysteresis for twophase flow in porous media, The European Physical Journal Special Topics, 223 (2014), pp. 2323–2338, https://doi.org/10.1140/epjst/e2014-02267-x.

[83] G. J. HIRASAKI, C. A. MILLER, AND M. PUERTO, Recent advances in surfactant eor, SPE Journal, 16 (2011), pp. 889–907, https://doi.org/10.2118/115386-PA.

[84] U. HORNUNG, Homogenization and porous media, vol. 6, Springer New York, NY, 1996, https://doi.org/10.1007/978-1-4612-1920-0.

[85] H. HUPPERT, Flow and instability of a viscous current down a slope, Nature, 300 (1982), pp. 427–429, https://doi.org/10.1038/300427a0.

[86] D. ILLIANO, I. S. POP, AND F. A. RADU, Iterative schemes for surfactant transport in porous media, Computational Geosciences, 25 (2021), pp. 805–822, https://doi.org/10.1007/s10596-020-09949-2.

[87] V. JOEKAR-NIASAR AND S. M. HASSANIZADEH, Analysis of fundamentals of two-phase flow in porous media using dynamic pore-network models: A review, Critical Reviews in Environmental Science and Technology, 42 (2012), pp. 1895–1976, https://doi.org/10.1080/10643389.2011.574101.

[88] S. KARPINSKI, I. S. POP, AND F. A. RADU, Analysis of a linearization scheme for an interior penalty discontinuous galerkin method for two-phase flow in porous media with dynamic capillarity effects, International Journal for Numerical Methods in Engineering, 112 (2017), pp. 553–577, https://doi.org/10.1002/nme.5526.

[89] J. KIM, A continuous surface tension force formulation for diffuse-interface models, Journal of Computational Physics, 204 (2005), pp. 784–804, https://doi.org/10.1016/j.jcp.2004.10.032.

[90] J. KIM, Phase-field models for multi-component fluid flows, Communications in Computational Physics, 12 (2012), pp. 613–661, https://doi.org/10.4208/cicp.301110.040811a.

[91] S.-B. KIM, Numerical analysis of bacterial transport in saturated porous media, Hydrological Processes: An International Journal, 20 (2006), pp. 1177–1186, https://doi.org/10.1002/hyp.5930.

[92] P. KNABNER AND L. ANGERMANN, Numerical methods for elliptic and parabolic partial differential equations, Springer Cham, 2003, https://doi.org/10.1007/978-3-030-79385-2.

[93] J. KOCH, A. RÄTZ, AND B. SCHWEIZER, Two-phase flow equations with a dynamic capillary pressure, European Journal of Applied Mathematics, 24 (2013), pp. 49–75, https://doi.org/10.1017/S0956792512000307.

[94] N. M. KOVALCHUK AND M. J. SIMMONS, Effect of surfactant dynamics on flow patterns inside drops moving in rectangular microfluidic channels, Colloids Interfaces, 5 (2021), p. 40, https://doi.org/10.3390/colloids5030040.

[95] K. KUMAR, T. L. V. NOORDEN, AND I. S. POP, Effective dispersion equations for reactive flows involving free boundaries at the microscale, Multiscale Modeling & Simulation, 9 (2011), pp. 29–58, https://doi.org/10.1137/100804553.

[96] K. KUMAR, T. VAN NOORDEN, AND I. S. POP, Upscaling of reactive flows in domains with moving oscillating boundaries, Discrete & Continuous Dynamical Systems-S, 7 (2014), pp. 95–111, https://doi.org/10.3934/dcdss.2014.7.95.

[97] A. LAMACZ, A. RÄTZ, AND S. B., A well-posed hysteresis model for flows in porous media and applications to fingering effects, Adv. Math. Sci. Appl., 21 (2011), pp. 33–64, https://doi.org/10.17877/DE290R-6610.

[98] D. LANDA-MARBÁN, G. BØDTKER, K. KUMAR, I. S. POP, AND F. A. RADU, An upscaled model for permeable biofilm in a thin channel and tube, Transport in Porous Media, 132 (2020), pp. 83–112, https://doi.org/10.1007/s11242-020-01381-5.

[99] D. LANDA-MARBÁN, G. BØDTKER, K. KUMAR, I. S. POP, AND F. A. RADU, An upscaled model for permeable biofilm in a thin channel and tube,

Transport in porous media, 132 (2020), pp. 83–112, https://doi.org/10.1007/s11242-020-01381-5.

[100] D. LANDA-MARBAN, F. A. RADU, AND J. M. NORDBOTTEN, Modeling and simulation of microbial enhanced oil recovery including interfacial area, Transport in Porous Media, 120 (2017), pp. 395–413, https://doi.org/10.1007/s11242-017-0929-6.

[101] D. LASSEUX, A. AHMADI, AND A. A. A. ARANI, Two-phase inertial flow in homogeneous porous media: A theoretical derivation of a macroscopic model, Transport in Porous Media, 75 (2008), pp. 371–400, https://doi.org/10.1007/s11242-008-9231-y.

[102] L. G. LEAL, Advanced transport phenomena: fluid mechanics and convective transport processes, vol. 7, Cambridge University Press, 2007, https://doi.org/10.1017/CBO9780511800245.

[103] S. LEE, A. MIKELIĆ, M. F. WHEELER, AND T. WICK, Phase-field modeling of two phase fluid filled fractures in a poroelastic medium, Multiscale Modeling & Simulation, 16 (2018), pp. 1542–1580, https://doi.org/10.1137/17M1145239.

[104] R. J. LEVEQUE, Finite difference methods for ordinary and partial differential equations, Society for Industrial and Applied Mathematics, 2007, https://doi.org/10.1137/1.9780898717839.

[105] V. G. LEVICH AND V. S. KRYLOV, Surface-tension-driven phenomena, Annual Review of Fluid Mechanics, 1 (1969), pp. 293–316, https://doi.org/10.1146/annurev.fl.01.010169.001453.

[106] X. LI, J. LOWENGRUB, A. RÄTZ, AND A. VOIGT, Solving PDEs in complex geometries: a diffuse domain approach, Communications in mathematical sciences, 7 (2009), pp. 81–107, https://doi.org/10.4310/cms.2009.v7.n1.a4.

[107] F. LIST AND F. A. RADU, A study on iterative methods for solving richards' equation, Computational Geosciences, 20 (2016), pp. 341–353, https://doi.org/10.1007/s10596-016-9566-3.

[108] S. B. LUNOWA, C. BRINGEDAL, AND I. S. POP, On an averaged model for immiscible two-phase flow with surface tension and dynamic contact angle in a thin strip, Studies in Applied Mathematics, 1 (2021), p. 43, https://doi.org/10.1111/sapm.12376.

[109] R. MAURI, Heat and mass transport in nonhomogeneous random velocity fields, Physical Riview E, 68 (2003), p. 066306, https://doi.org/10.1103/PhysRevE.68.066306.

[110] Y. MEHMANI AND H. TCHELEPI, Multiscale computation of pore-scale fluid dynamics: Single-phase flow, Journal of Computational Physics, 375 (2018), pp. 1469–1487, https://doi.org/10.1016/j.jcp.2018.08.045.

[111] Y. MEHMANI AND H. TCHELEPI, Multiscale formulation of two-phase flow at the pore scale, Journal of Computational Physics, 389 (2019), pp. 164–188, https://doi.org/10.1016/j.jcp.2019.03.035.

[112] S. MEIJERS, J. BIJEN, R. DE BORST, AND A. FRAAIJ, Computational results of a model for chloride ingress in concrete including convection, drying-wetting cycles and carbonation, Materials and structures, 38 (2005), pp. 145–154, https://doi.org/10.1007/BF02479339.

[113] S. METZGER AND P. KNABNER, Homogenization of two-phase flow in porous media from pore to Darcy scale: a phase-field approach, Multiscale Modeling & Simulation, 19 (2021), pp. 320–343, https://doi.org/10.1137/19M1287705.

[114] A. MIKELIĆ, A convergence theorem for homogenization of two-phase miscible flow through fractured reservoirs with uniform fracture distributions, Applicable Analysis, 33 (1989), pp. 203–214, https://doi.org/10.1080/00036818908839873.

[115] A. MIKELIĆ, On an averaged model for the 2-fluid immiscible flow with surface tension in a thin cylindrical tube, Computational Geosciences, 7 (2003), pp. 183–196, https://doi.org/10.1023/A:1025527716078.

[116] A. MIKELIĆ, On an averaged model for the 2-fluid immiscible flow with surface tension in a thin cylindrical tube, Computational Geosciences, 7 (2003), pp. 183–196.

[117] A. MIKELIĆ AND L. PAOLI, On the derivation of the buckley—leverett model from the two fluid navier—stokes equations in a thin domain, Computational Geosciences, 1 (1997), pp. 59–83, https://doi.org/10.1023/A:1011509010432.

[118] A. MIKELIC AND L. PAOLI, On the derivation of the buckley-leverett model from the two fluid navier-stokes equations in a thin domain, Computational Geosciences, 4 (2000), pp. 99–101, https://doi.org/10.1023/A:1011503731330.

[119] A. MIKELIC AND C. ROSIER, Modeling solute transport through unsaturated porous media using homogenization i, Computational & Applied Mathematics, 23 (2004), pp. 195–211, https://doi.org/doi.org/10.1590/S0101-82052004000200006.

[120] A. MIKELIĆ, M. F. WHEELER, AND T. WICK, Phase-field modeling of a fluid-driven fracture in a poroelastic medium, Computational Geosciences, 19 (2015), pp. 1171–1195, https://doi.org/10.1007/s10596-015-9532-5.

[121] N. R. MORROW AND C. C. HARRIS, Capillary equilibrium in porous materials, SPE Journal, 5 (1965), pp. 15–24, https://doi.org/10.2118/1011-PA.

[122] Y. MUALEM, A new model for predicting the hydraulic conductivity of unsaturated porous media, Water Resources Research, 12 (1976), pp. 513–522, https://doi.org/10.1029/WR012i003p00513.

[123] M. K. MULLIGAN AND J. P. ROTHSTEIN, The effect of confinement-induced shear on drop deformation and breakup in microfluidic extensional flows, Physics of Fluids, 23 (2011), p. 022004, https://doi.org/10.1063/1.3548856.

[124] S. M. NIELSEN, I. NESTEROV, AND A. SHAPIRO, Microbial enhanced oil recovery—a modeling study of the potential of spore-forming bacteria, Com-

putational Geosciences, 20 (2016), pp. 567–580, https://doi.org/10.1007/s10596-015-9526-3.

[125] J. Niessner and S. M. Hassanizadeh, A model for two-phase flow in porous media including fluid-fluid interfacial area, Water Resources Research, 44 (2008), https://doi.org/10.1029/2007WR006721.

[126] A. A. Olajire, Review of asp eor (alkaline surfactant polymer enhanced oil recovery) technology in the petroleum industry: Prospects and challenges, Energy, 77 (2014), pp. 963–982, https://doi.org/10.1016/j.energy.2014.09.005.

[127] A. Oron, S. H. Davis, and S. G. Bankoff, Long-scale evolution of thin liquid films, Reviews of Modern Physics, 69 (1997), p. 931, https://doi.org/10.1103/RevModPhys.69.931.

[128] S. Osher and R. P. Fedkiw, Level set methods: an overview and some recent results, Journal of Computational Physics, 169 (2001), pp. 463–502, https://doi.org/10.1006/jcph.2000.6636.

[129] H. Pape, C. Clauser, J. Iffland, R. Krug, and R. Wagner, Anhydrite cementation and compaction in geothermal reservoirs: Interaction of pore-space structure with flow, transport, p–t conditions, and chemical reactions, International Journal of Rock Mechanics and Mining Sciences, 42 (2005), pp. 1056–1069, https://doi.org/10.1016/j.ijrmms.2005.05.007.

[130] S. Patankar, Numerical heat transfer and fluid flow, CRC press, 1980, https://doi.org/10.1201/9781482234213.

[131] G. Pavliotis and A. Stuart, Multiscale methods: averaging and homogenization, Springer New York, NY, 2008, https://doi.org/10.1007/978-0-387-73829-1.

[132] M. Peszynska, A. Trykozko, G. Iltis, S. Schlueter, and D. Wildenschild, Biofilm growth in porous media: experiments, computational modeling at the porescale, and upscaling, Advances in Water Resources, 95 (2016), pp. 288–301, https://doi.org/10.1016/j.advwatres.2015.07.008.

[133] D. PICCHI AND I. BATTIATO, The impact of pore-scale flow regimes on upscaling of immiscible two-phase flow in porous media, Water Resources Research, 54 (2018), pp. 6683–6707, https://doi.org/10.1029/2018WR023172.

[134] D. PICCHI AND I. BATTIATO, The impact of pore-scale flow regimes on upscaling of immiscibletwo-phase flow in porous media, Water Resources Research, 54 (2018), pp. 6683–6707, https://doi.org/10.1029/2018WR023172.

[135] B. PLOHR, D. MARCHESIN, P. BEDRIKOVETSKY, AND P. KRAUSE, Modeling hysteresis in porous media flow via relaxation, Computational Geosciences, 5 (2001), pp. 225–256, https://doi.org/10.1023/A:1013759420009.

[136] I. POP, F. RADU, AND P. KNABNER, Mixed finite elements for the richards' equation: linearization procedure, Journal of Computational and Applied Mathematics, 168 (2004), pp. 365–373, https://doi.org/https://doi.org/10.1016/j.cam.2003.04.008.

[137] I. S. POP, C. J. VAN DUIJN, J. NIESSNER, AND S. M. HASSANIZADEH, Horizontal redistribution of fluids in a porous medium: The role of interfacial area in modeling hysteresis, Advances in Water Resources, 32 (2009), pp. 383–390, https://doi.org/10.1016/j.advwatres.2008.12.006.

[138] A. POULOVASSILIS, Hysteresis of pore water in granular porous bodies, Soil Science, 109 (1970), pp. 5–12, https://doi.org/10.1097/00010694-197001000-00002.

[139] A. QUARTERONI, R. SACCO, AND F. SALERI, Numerical mathematics, vol. 37, Springer Science & Business Media, 2010.

[140] M. QUINTARD AND S. WHITAKER, Two-phase flow in heterogeneous porous media: The method of large-scale averaging, Transport in Porous Media, 3 (1988), pp. 357–413, https://doi.org/10.1007/BF00233177.

[141] M. QUINTARD AND S. WHITAKER, Transport in ordered and disordered porous media: volume-averaged equations, closure problems, and compari-

son with experiment, Chemical Engineering Science, 48 (1993), pp. 2537–2564, https://doi.org/10.1016/0009-2509(93)80266-S.

[142] F. A. RADU, K. KUMAR, J. M. NORDBOTTEN, AND I. S. POP, A robust, mass conservative scheme for two-phase flow in porous media including hölder continuous nonlinearities, IMA Journal of Numerical Analysis, 38 (2018), pp. 884–920, https://doi.org/10.1093/imanum/drx032.

[143] F. A. RADU, J. M. NORDBOTTEN, I. S. POP, AND K. KUMAR, A robust linearization scheme for finite volume based discretizations for simulation of two-phase flow in porous media, Journal of Computational and Applied Mathematics, 289 (2015), pp. 134–141, https://doi.org/10.1016/j.cam.2015.02.051.

[144] A. RÄTZ AND B. SCHWEIZER, Hysteresis models and gravity fingering in porous media, ZAMM - Journal of Applied Mathematics and Mechanics, 94 (2014), pp. 645–654, https://doi.org/10.1002/zamm.201200052.

[145] A. RÄTZ AND B. SCHWEIZER, Hysteresis models and gravity fingering in porous media, ZAMM-Journal of Applied Mathematics and Mechanics/Zeitschrift für Angewandte Mathematik und Mechanik, 94 (2014), pp. 645–654, https://doi.org/10.1002/zamm.201200052.

[146] P.-A. RAVIART AND J.-M. THOMAS, A mixed finite element method for 2-nd order elliptic problems, in Mathematical aspects of finite element methods, Springer, Berlin, Heidelberg, 1977, pp. 292–315, https://doi.org/10.1007/BFb0064470.

[147] D. RAY, C. LIU, AND B. RIVIERE, A discontinuous galerkin method for a diffuse-interface model of immiscible two-phase flows with soluble surfactant, Computational Geosciences, 25 (2021), pp. 1775–1793, https://doi.org/10.1007/s10596-021-10073-y.

[148] N. RAY, T. VAN NOORDEN, F. FRANK, AND P. KNABNER, Multiscale modeling of colloid and fluid dynamics in porous media including an evolving microstructure, Transport in Porous Media, 95 (2012), pp. 669–696, https://doi.org/10.1007/s11242-012-0068-z.

[149] N. Ray, T. van Noorden, F. A. Radu, W. Friess, and P. Knabner, Drug release from collagen matrices including an evolving microstructure, ZAMM - Journal of Applied Mathematics and Mechanics, 93 (2013), pp. 811–822, https://doi.org/10.1002/zamm.201200196.

[150] M. Redeker, C. Rohde, and I. S. Pop, Upscaling of a tri-phase phase-field model for precipitation in porous media, IMA Journal of Applied Mathematics, 81 (2016), pp. 898–939, https://doi.org/10.1093/imamat/hxw023.

[151] F. Rezanezhad, H.-J. Vogel, and K. Roth, Experimental study of fingered flow through initially dry sand, Hydrology and Earth System Sciences Discussions, 3 (2006), pp. 2595–2620, https://doi.org/10.5194/hessd-3-2595-2006.

[152] L. A. Richards, Capillary conduction of liquids through porous mediums, Physics, 1 (1931), pp. 318–333, https://doi.org/10.1063/1.1745010.

[153] C. Rohde and L. von Wolff, Homogenization of Nonlocal Navier–Stokes–Korteweg Equations for Compressible Liquid-Vapor Flow in Porous Media, SIAM Journal on Mathematical Analysis, 52 (2020), pp. 6155–6179.

[154] M. Schmuck, M. Pradas, G. A. Pavliotis, and S. Kalliadasis, Derivation of effective macroscopic Stokes-Cahn-Hilliard equations for periodic immiscible flows in porous media, Nonlinearity, 26 (2013), pp. 3259–3277, https://doi.org/10.1088/0951-7715/26/12/3259.

[155] M. Schneider, T. Koeppl, R. Helmig, R. Steinle, and R. Hilfer, Stable propagation of saturation overshoots for two-phase flow in porous media, Transport in Porous Media, 121 (2018), pp. 621–641, https://doi.org/10.1007/s11242-017-0977-y.

[156] R. Schulz, Biofilm modeling in evolving porous media with beavers-joseph condition, ZAMM - Journal of Applied Mathematics and Mechanics, 99 (2019), https://doi.org/10.1002/zamm.201800123.

[157] R. Schulz, Crystal precipitation and dissolution in a porous medium: evolving microstructure and perforated solid matrix, Special Topics & Reviews in Porous

Media: An International Journal, 10 (2019), pp. 305–321, https://doi.org/10.1615/SpecialTopicsRevPorousMedia.2019029274.

[158] R. Schulz and P. Knabner, An effective model for biofilm growth made by chemotactical bacteria in evolving porous media, SIAM journal on Applied Mathematics, 77 (2017), pp. 1653–1677, https://doi.org/10.1137/16M108817X.

[159] B. Schweizer, Hysteresis in porous media: Modelling and analysis, Interfaces and Free Boundaries, 19 (2017), pp. 417–447, https://doi.org/10.4171/IFB/388.

[160] L. E. SCRIVEN and C. V. STERNLING, The Marangoni Effects, Nature, 187 (1960), pp. 186–188, https://doi.org/10.1038/187186a0.

[161] S. Sharmin, M. Bastidas, C. Bringedal, and I. Pop, Upscaling a navier-stokes-cahn-hilliard model for two-phase porous-media flow with solute-dependent surface tension effects, Applicable Analysis, 101 (2022), pp. 1–23, https://doi.org/10.1080/00036811.2022.2052858.

[162] S. Sharmin, C. Bringedal, and I. S. Pop, On upscaling pore-scale models for two-phase flow with evolving interfaces, Advances in Water Resources, 142 (2020), p. 103646, https://doi.org/10.1016/j.advwatres.2020.103646.

[163] J. J. Sheng, Status of surfactant eor technology, Petroleum, 1 (2015), pp. 97–105, https://doi.org/https://doi.org/10.1016/j.petlm..07.003.

[164] S. Shiozawa and H. Fujimaki, Unexpected water content profiles under flux-limited one-dimensional downward infiltration in initially dry granular media, Water Resources Research, 40 (2004), https://doi.org/10.1029/2003WR002197.

[165] J. E. Smith and R. W. Gillham, Effects of solute concentration–dependent surface tension on unsaturated flow: Laboratory sand column experiments, Water Resources Research, 35 (1999), pp. 973–982, https://doi.org/10.1029/1998WR900106.

[166] H. A. Stone and L. G. Leal, The effects of surfactants on drop deformation and breakup, Journal of Fluid Mechanics, 220 (1990), pp. 161–186, https://doi.org/10.1017/S0022112090003226.

[167] T. Sweijen, C. J. van Duijn, and S. M. Hassanizadeh, A model for diffusion of water into a swelling particle with a free boundary: Application to a super absorbent polymer, Chemical Engineering Science, 172 (2017), pp. 407–413, https://doi.org/10.1016/j.ces.2017.06.045.

[168] A. M. Tartakovsky and P. Meakin, Pore scale modeling of immiscible and miscible fluid flows using smoothed particle hydrodynamics, Advances in Water Resources, 29 (2006), pp. 1464–1478, https://doi.org/10.1016/j.advwatres.2005.11.014.

[169] G. I. Taylor, Dispersion of soluble matter in solvent flowing slowly through a tube, Proceedings of the Royal Society of London. Series A. Mathematical and Physical Sciences, 219 (1953), pp. 186–203, https://doi.org/10.1098/rspa.1953.0139.

[170] S. W. Taylor and P. R. Jaffé, Substrate and biomass transport in a porous medium, Water Resources Research, 26 (1990), pp. 2181–2194, https://doi.org/10.1029/WR026i009p02181.

[171] C. J. van Duijn, Y. Fan, L. A. Peletier, and I. S. Pop, Travelling wave solutions for degenerate pseudo-parabolic equations modelling two-phase flow in porous media, Nonlinear Analysis: Real World Applications, 14 (2013), pp. 1361–1383, https://doi.org/10.1016/j.nonrwa.2012.10.002.

[172] C. J. van Duijn, A. Mikelic, I. S. Pop, and C. Rosier, Effective dispersion equations for reactive flows with dominant peclet and damkohler numbers, Advances in Chemical Engineering, 34 (2008), pp. 1–45, https://doi.org/10.1016/S0065-2377(08)00001-X.

[173] C. J. van Duijn and K. Mitra, Hysteresis and horizontal redistribution in porous media, Transport in Porous Media, 122 (2018), pp. 375–399, https://doi.org/10.1007/s11242-018-1009-2.

[174] C. J. van Duijn, K. Mitra, and I. S. Pop, Travelling wave solutions for the richards equation incorporating non-equilibrium effects in the capillarity pressure, Nonlinear Analysis: Real World Applications, 41 (2018), pp. 232–268, https://doi.org/10.1016/j.nonrwa.2017.10.015.

[175] M. T. Van Genuchten, A closed-form equation for predicting the hydraulic conductivity of unsaturated soils, Soil science society of America journal, 44 (1980), pp. 892–898, https://doi.org/10.2136/sssaj1980.03615995004400050002x.

[176] T. van Noorden, I. S. Pop, A. Ebigbo, and R. Helmig, An upscaled model for biofilm growth in a thin strip, Water Resources Research, 46 (2010), https://doi.org/10.1029/2009WR008217.

[177] T. L. van Noorden, Crystal precipitation and dissolution in a porous medium: effective equations and numerical experiments, Multiscale Modeling & Simulation, 7 (2008), pp. 1220–1236, https://doi.org/10.1137/080722096.

[178] T. L. van Noorden, Crystal precipitation and dissolution in a porous medium: Effective equations and numerical experiments, Multiscale Modeling & Simulation, 7 (2009), pp. 1220–1236, https://doi.org/10.1137/080722096.

[179] T. L. van Noorden, Crystal precipitation and dissolution in a thin strip, European Journal of Applied Mathematics, 20 (2009), pp. 69–91, https://doi.org/10.1017/S0956792508007651.

[180] T. L. van Noorden and C. Eck, Phase field approximation of a kinetic moving-boundary problem modelling dissolution and precipitation, Interfaces and Free Boundaries, 13 (2011), pp. 29–55.

[181] H. Vereecken, R. Kasteel, J. Vanderborght, and T. Harter, Upscaling hydraulic properties and soil water flow processes in heterogeneous soils: A review, Vadose Zone Journal, 6 (2007), pp. 1–28, https://doi.org/10.2136/vzj2006.0055.

[182] E. W. WASHBURN, The dynamics of capillary flow, Physical Review, 17 (1921), pp. 273–283, https://doi.org/10.1103/PhysRev.17.273.

[183] S. WEINBAUM, X. ZHANG, Y. HAN, H. VINK, AND S. C. COWIN, Mechanotransduction and flow across the endothelial glycocalyx, Proceedings of the National Academy of Sciences, 100 (2003), pp. 7988–7995, https://doi.org/10.1073/pnas.133280810.

[184] S. WHITAKER, Flow in porous media ii: The governing equations for immiscible, two-phase flow, Transport in Porous Media, 1 (1986), pp. 105–125, https://doi.org/10.1007/BF00714688.

[185] Z. WU, X. YUE, T. CHENG, J. YU, AND H. YANG, Effect of viscosity and interfacial tension of surfactant–polymer flooding on oil recovery in high-temperature and high-salinity reservoirs, Journal of Petroleum Exploration and Production Technology, 4 (2014), pp. 9–16, https://doi.org/10.1007/s13202-013-0078-6.

[186] H. ZHANG AND P. ZEGELING, A numerical study of two-phase flow models with dynamic capillary pressure and hysteresis, Transport in Porous Media, 116 (2017), pp. 825–846, https://doi.org/10.1007/s11242-016-0802-z.

[187] X. ZHANG, F. MA, S. YIN, C. D. WALLACE, M. R. SOLTANIAN, Z. DAI, R. W. RITZI, Z. MA, C. ZHAN, AND X. LÜ, Application of upscaling methods for fluid flow and mass transport in multi-scale heterogeneous media: A critical review, Applied Energy, 303 (2021), p. 117603, https://doi.org/10.1016/j.apenergy.2021.117603.

[188] X. ZHANG AND D. M. TARTAKOVSKY, Effective ion diffusion in charged nanoporous materials, Journal of The Electrochemical Society, 164 (2017), p. E53, https://doi.org/10.1149/2.0491704jes.

[189] G. ZHU AND A. LI, Interfacial dynamics with soluble surfactants: A phase-field two-phase flow model with variable densities, Advances in Geo-Energy Research, 4 (2020), pp. 86–98, https://doi.org/10.26804/ager.2020.01.08.

[190] L. Zhuang, S. Hassanizadeh, C. J. van Duijn, S. Zimmermann, I. Zizina, and R. Helmig, Experimental and numerical studies of saturation overshoot during infiltration into a dry soil, Vadose Zone Journal, 18 (2019), https://doi.org/10.2136/vzj2018.09.0167.

[191] P. Zitha, R. Felder, D. Zornes, K. Brown, and K. Mohanty, Increasing hydrocarbon recovery factors, Society of Petroleum Engineers, (2011), pp. 1–9.